UNIVERSITÀ DEGLI STUDI
DI GENOVA

ISTITUTO ITALIANO
DI TECNOLOGIA

Colloidal Synthesis of Lead Halide Perovskite Nanocrystals for Optoelectronic Applications

By

Javad Shamsi

A dissertation submitted in partial fulfillment

of the requirements for the degree of

Doctor of Philosophy

(NANOCHEMISTRY)

In the University of Genoa

2018

UNIVERSITA' DI GENOVA

DIPARTIMENTO DI CHIMICA E CHIMICA INDUSTRIALE
Via Dodecaneso, 31 – 16146 GENOVA
Tel. +39 – 010- 3536154

DOCTORATE COURSE IN SCIENCES AND TECHNOLOGIES OF CHEMISTRY AND MATERIALS

CURRICULUM: NANOCHEMISTRY

Advisors:

Prof. Liberato Manna

Prof. Adriana Saccone

Doctoral Committee:

Prof. Houtepen Arjan, University of Delft, The Netherlands

Prof. Loi Maria Antonietta, Univ. of Groningen, The Netherlands

Prof. Relini Annalisa, Università di Genova, Italy

Javad Shamsi

Javad.shamsi@iit.it

javadshamsii@gmail.com

ORCID iD: 0000-0003-4684-5407

To my parents

Soodabeh Zamani & Samad Shamsi

Contents

Acknowledgements

Foremost, I would like to thank Prof. Dr. Liberato Manna who gave me the great opportunity to work in his prestigious group. Libero, I would like to express my sincere gratitude to you for your patience, motivation, enthusiasm, and immense knowledge.

Many thanks to my colleagues and friends at Istituto Italiano di Tecnologia for all the fun and collaboration.

Lastly, thanks to my parents and my sister for all the moral support and the amazing chances they've given me over the years.

Thank You dear God. I love You so much. You are everything I need.

1. Introduction

Light is an inseparable component of our daily lives and is a crucial cross-cutting discipline of science in the 21st century. The fields of optics, photonics and optoelectronics, which are the branches of physics and involve the behavior and properties of the light, are somewhat intertwined and strongly contribute in modern technologies[1]. Into such technologies, experimental and theoretical research extends from material breakthroughs on an atomic level through to the development of optical techniques[2-5]. Optoelectronic devices incorporating new, inexpensive materials such as semiconductors show tremendous promise to alter the energy landscape by reducing the cost of both energy production and consumption[6, 7].

Since 1833 when Michael Faraday noticed the temperature dependence of the electrical conductivity of silver sulfide till today, *semiconductors* have changed the world beyond anything that could have been imagined before them[8]. A semiconductor material is one whose electrical properties lie in between those of insulators and good conductors (e.g. metals)[9]. Semiconductors have conductivity between 10^4 and 10^{-10} $(\Omega cm)^{-1}$. They can be also defined as those materials which have a very narrow energy gap separating the empty conduction band (CB) and fully filled valence band (VB)[9]. It's well known that semiconductors are classified as *Intrinsic* and *Extrinsic*. Depending on the type of doping material used, the latter one can be sub-divided into two classes: *n-type* and *p-type* semiconductors[11]. The best-known semiconductor is surely silicon (Si)[12]. However, there are many minerals besides Si found in nature that are semiconductors, such as ZnS, Cu_2O and PbS. In addition, semiconductors come about in many different chemical compositions with a large variety of crystal structures. Many photochemical and photophysical processes have been expanded by the interaction of semiconductors and electromagnetic field. When the light with energy higher than the absorption threshold of the semiconductor pass into the semiconductor, the semiconductor absorbs photons and such phenomenon initiates the excitation process of the VB's electron into the CB and leaves a positive hole in the VB[11]. This simple process (and/or vice-versa) is indeed the heart of most optoelectronic devices.

A new class of medium-bandgap semiconductors called *halide perovskites*, have become one of the hottest topics in optoelectronic materials research in recent years[4, 13-16]. In contrast to conventional semiconductors such as Si, perovskites offer simple *bandgap tunability* by *changing the composition* and *low-temperature processability* in the form of bulk single crystals, thin films, or supported and unsupported nanostructures[17, 18]. In particular, the form of *colloidal nanocrystals* of such materials have emerged as a versatile photonic source, utilized via bright photoluminescence (PL) in displays or lighting or via electroluminescence in light-emitting diodes[19-21].

1.1. The ABX_3 Perovskite Structure

The perovskite crystal structure was discovered in 1839 by the German mineralogist Gustav Rose in the Ural Mountains in Russia[13]. This natural occurring mineral, calcium titanium oxide ($CaTiO_3$), was named after Russian mineralogist Lev Perovski. Later on, perovskite has given its name to any material with the same type of crystal structure as $CaTiO_3$ called *perovskites*, which have a general formula close to or derived from the composition ABX_3 (Figure 1.1)[22]. A pure perovskite compound is generally described as a three-dimensional sequence of a corner-sharing octahedral BX_6 unit, as shown in Figure 1.1. A cation fills the voids formed by every eight adjacent BX_6 octahedra and serves principally as a counter ion for charge balance and physical stabilization, but its influence on octahedral orientation and dimensionality leads to profound effects on electronic structure[23].

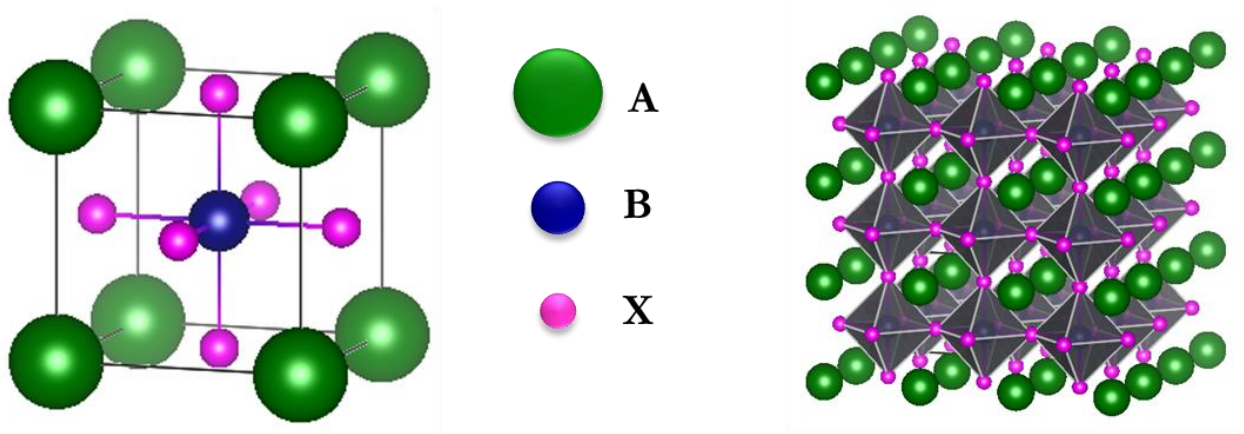

Figure 1.1: Schematic perovskite ABX_3 structure

The correlation between the distortion and stability of the ABX_3 crystal structure was first investigated by Victor Moritz Goldschmidt in 1926[4]. The stability and final crystal structure of the B-X framework is determined by the ionic radii of the anion and cations. This stability can be described by the semi empirical geometric *Goldsmith tolerance factor*, *t* (formula 1), and is dependent of the ionic radii of A, B and X (rA, rB and rX. respectively). In general, stable perovskite structures are formed when the tolerance factor falls between 0.8 and 1. When the tolerance factor falls out of this range, non-perovskite structures or 2D perovskites can be formed, as will be further discussed later on[24]. Stable perovskites are further constrained by the octahedral factor μ (formula 2), which describes the stability of the BX_6 octahedron which is dependent on the anion radii of B and X (stable with a μ between 0.44 and 0.9).

1) Goldsmith tolerance factor, $t = \frac{r_A + r_X}{\sqrt{2}(r_B + r_X)}$
2) Octahedral factor, $\mu = r_B/r_X$

The octahedral factor (μ) together with the tolerance factor, provides a parameter space for perovskite formability and can be used to predict novel perovskite combinations[25]. Although this method gives a good approach to predict novel perovskite materials, it is limited and less accurate for larger anions (less electronegative halides) and for non-spherical A^+ cations (linear, non-spherical A^+ cations can rotate and align with the lead halide framework and thus minimize their effective atomic radius). More sophisticated realistic calculations alter these formation diagrams and allow for a better assignment of stable phases. The standard and often depicted perovskite phase is the pure cubic phase, Pm-3m, and has the highest symmetry. This phase though is in most cases not the most stable phase. Small rotations of the BX_6 octahedron can lower the symmetry from cubic to tetragonal and orthorhombic phase, in order of decreasing symmetry. In general, these small rotations lower the overall unit cell size and are often most favored. Furthermore, a higher tolerance factor influences the stability of higher symmetry phases. Although this changes are often minor in the unit cell lattice parameters, they can have a considerable impact on the optical properties, turning the perovskites from, small semiconductor bandgaps to large insulator or indirect bandgaps. For instance, in *lead iodide perovskite*, the small cation (Cs^+, Cs is still not large enough to hold the stable cubic perovskite structure) causes the octahedral framework to tilt into an orthorhombic crystal structure (the PbI_6 is larger than the $PbBr_6$ framework and the smaller Cs thus causes more tilting) and the orthorhombic phase is a non-luminescent material. In fact this must be replaced with a larger molecule, such as methylammonium or formamidinium.

1.2. Lead Halide Perovskite

An emerging class of materials called *lead* halide perovskites (LHPs) is poised to revolutionise both the PV and LED fields. Their crystal structures (including space group and lattice parameter) as well as ferroelectric behaviors were initially investigated in 1958 by Moller[26]. The first exploitation of perovskite as a solar cell absorber (light-to-electricity conversion process) was reported in 2009 by Kojima *et al.* with less than 4% efficiency[27]. Due to the poor stability and low efficiency of reported solar cell, such system didn't initially attract scientific community's attention. Three years later two simultaneous breakthrough works on solid-state solar cells with 10-11% efficiencies triggered the prompt development and implementation of low-cost solution processed perovskite solar cells. Since then, huge research efforts have focused on fundamental understanding of material properties as well as perovskite material/device development and device principles[4, 28-32].

The crystal structure of LHPs is analogous to ABX_3, consisting of a monovalent cation, both organic and inorganic (A = Cs^+, methyl ammonium (MA^+), formamidinium (FA^+)), a divalent cation (B = Pb^{2+}), and monovalent halides (X = Cl^-, Br^- and I^-). LHPs with the tolerance factor between 0.89 – 1, normally exist in cubic structure[25] (figure 1.2) while the smaller *t* could result the lower-symmetry tetragonal (β phase) or orthorhombic (γ phase) structures. moreover, larger *t* causes the destabilization of the 3D lead-halogen framework and leads to the formation of layered perovskite structure.

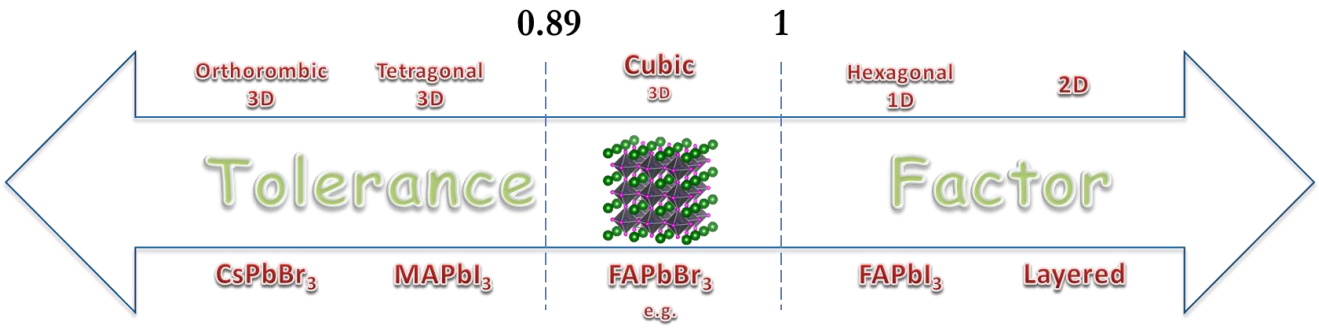

Figure 1.2: Few examples of the relation between tolerance factors (t) and lead halide perovskite crystal structures

1.3. Origin of Bandgap, Optical Properties and Influence of Halides

LHPs are classified as direct-bandgap semiconductors and the states around the band gap come from X and Pb atoms, whereas A-site cation has no contribution. In the valence band, the Pb s and X np states have strong hybridization (Figure 1.3) and their antibonding interaction leads to the formation of the upper valence band. On the contrary, the conduction band is formed through the coupling between the empty Pb p states and the X np states with n = 5, 4, 3 for X = I, Br, Cl, respectively. Because of the ionic nature of LHPs, the antibonding interactions between the valence band and conduction band states are insignificant, so the lower conduction bands have almost no contribution from Br atoms[33].

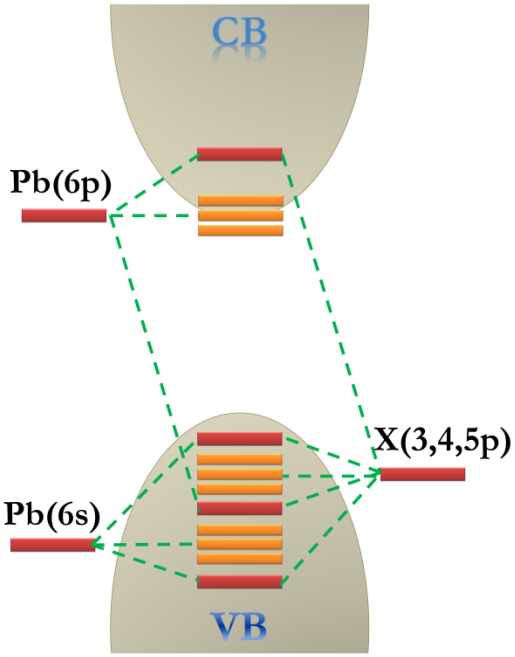

Figure 1.3: schematic of the electronic structure of $APbX_3$

As the optical absorption coefficient of a material is closely related to its electronic structure, the unique electronic structure of LHPs results to the superior optical properties, such as high optical absorption which makes them promising material for photovoltaics[13]. The much higher optical absorption of LHPs than the absorber layers in second-generation solar cells (GaAs as example) is because the density of states (DOS) derived from the Pb p orbital in the lower CB is significantly higher than that of GaAs owing to a more dispersed s orbital from Ga. In fact, this unique configuration manifests the importance of Pb for the outstanding optical properties of LHPs.

In contrast to conventional semiconductors such as Si, LHPs offer simple bandgap tunability[34-36] by changing the elemental compositions and low-temperature solution processability. As shown in Figure 1.3 the electronic structure of LHPs is related to the p orbital of X and thus, the bandgap can generally be tuned by the p orbital of X i.e., the valence orbital of the halide changes from 3p to 4p to 5p when X changes from Cl to Br to I. Practically, Noh et al. first demonstrated a continuous bandgap tuning in the LHPs via adjusting the ratio of Br to I, as illustrated in Figure 1.4[36].

1.4. Defects and Defects-Tolerance in LHPs

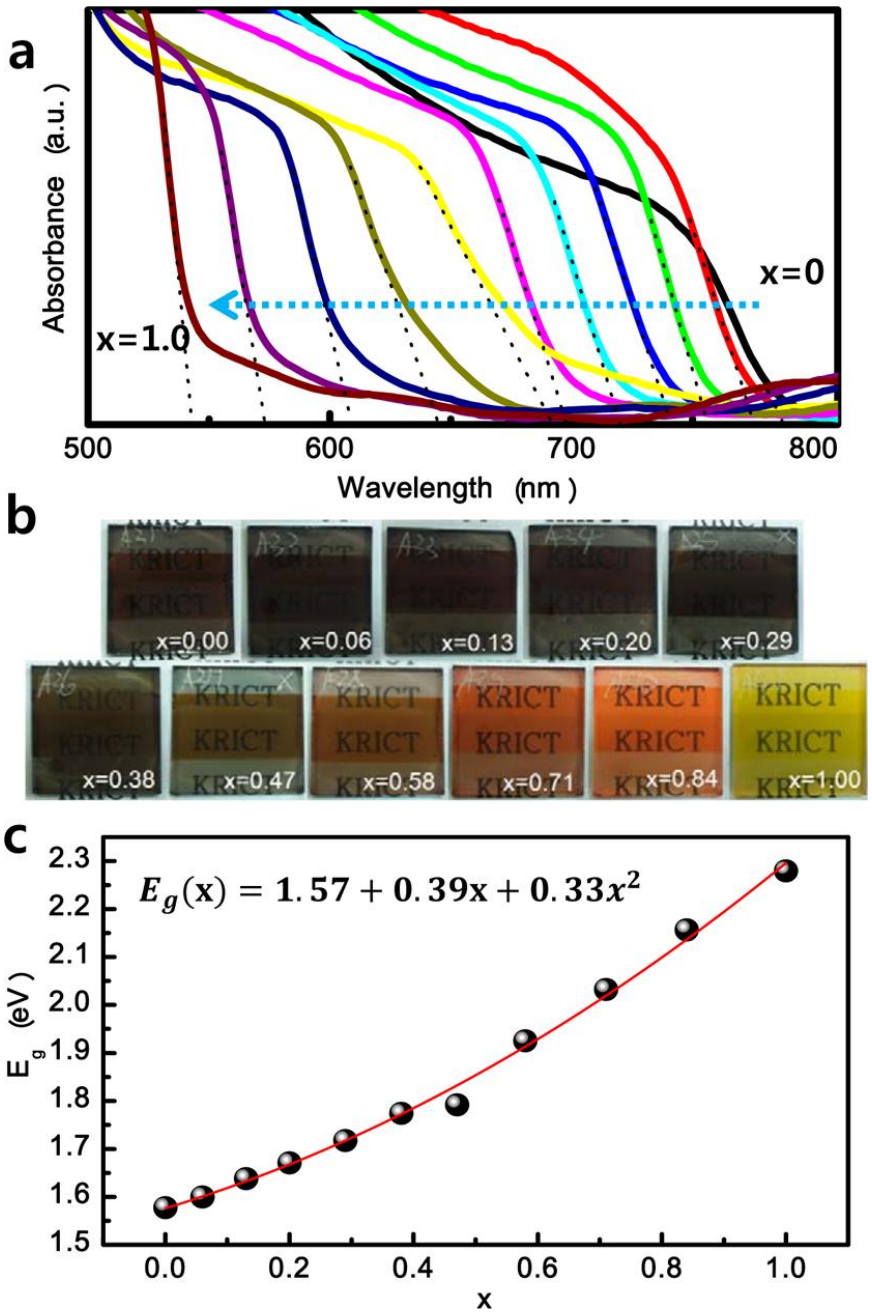

Figure 1.4: Photographs and UV–vis absorption spectra of $MAPb(I_{1-x}Br_x)_3$. (a) UV–vis absorption spectra of FTO/bl-TiO_2/mp-TiO_2/ $MAPb(I_{1-x}Br_x)_3$/Au cells measured using an integral sphere. (b) Photographs of 3D TiO_2/$MAPb(I1-xBrx)_3$ bilayer nanocomposites on FTO glass substrates. (c) A quadratic relationship of the band-gaps of $MAPb(I1-xBrx)_3$ as a function of Br composition (x). (Reprinted with permission from ref. 36)

In conventional semiconductors, crystallographic defects can be in the form of point defects, where interruptions exist in the perfect crystal lattice. They can appear in the form of atomic vacancies (atoms missing from the lattice), interstitials (atoms occupying the space between atoms in the lattice), and anti-site substitutions (atoms occupying the wrong site in the lattice), or higher-dimensional defects, such as dislocations, grain boundaries, *etc*[37]. In LHPs the major type of point defects are vacancies

which have much lower formation energy compared with other semiconductors, i.e. < 0.5 eV, resulting a high concentration of Schottky-type A-site and/or halide vacancies in such materials[37]. Low lattice energy in LHPs, which is originated from the lower charges of the constituent ions in LHPs, can also promote other types of defects, such as grain boundaries, dislocations, stacking faults and twin planes[37, 38]. Different studies of point defects in the bulk material or on the surface of nanocrystals and at grain boundaries showed that defects in LHPs do not form mid-gap trap states[33]. This defect tolerance again originates from the unique feature of band structure of LHPs (Figure 1.3) in which the vacancies form states residing within the VB and CB, or at worst are shallow defects[24].

1.5. Bulk Crystal Growth of Lead Halide Perovskite

Bulk halide perovskite single crystals exhibit remarkable optical and electrical properties such as long carriers lifetime, high carrier mobility, long diffusion length, and low trap state densities.[39-44] In addition to providing an ideal platform for the proper understanding of the material's merits, bulk crystals have been integrated in optoelectronic devices including solar cells[45, 46] and photodetectors.[47-55]

High-quality $MAPbBr_3$ ($MA = CH_3NH_3^+$) bulk single crystals grown in organic solvents are generally grown either by an anti-solvent vapor-assisted crystallization (AVC)[41] or by inverse temperature crystallization (ITC).[56, 57] Despite AVC and ITC being very different in terms of solvents, crystallization temperature, and growth rate, the formed crystals are of similar quality based on their measured optical and transport properties. Nevertheless, it is also reported that different crystallization techniques/additives could have a significant impact on the crystalline quality of the as-grown single crystals and hence on their transport properties.[58] In devices, the higher crystalline nature of planar-integrated single-crystalline $MAPbBr_3$ compared to polycrystalline thin films ensures a much better performing photodetector.[59] In addition to the crystalline quality, it has been found that the quality of the surface plays a crucial role in the final properties of perovskite bulk crystals.[60, 61] Trap density was shown to be much higher at the surface than in the bulk of the crystal,[62, 63] and several attempts to passivate the surface traps in order to achieve enhanced optoelectronic properties such as increased photoluminescence (PL) have been reported. Surface passivation requires the addition of an external passivating layer, which was previously achieved for perovskite thin films through halogen bonding[64] or Lewis base passivation[65, 66] or for single-crystalline perovskite nanowires through soaking in oleic acid.[67] Recently, thin films of halide perovskite were prepared from precursors introduced in non-stoichiometric ratios (i.e. using an excess of MAI) in order to passivate the grain boundaries and reduce

the non-radiative recombination[68] as well as to enhance the crystal stability.[69] The solution-based growth of fully inorganic $CsPbX_3$ bulk crystals also gained much attention as they could perhaps overcome the known issues of chemical instability of hybrid perovskites[31, 70].

Schematic representation of AVC and ITC are shown in Figures 1.5 and 1.6, respectively. Briefly, in AVC using a solvent with high solubility and moderate coordination for MAX and PbX_2 [N,N-dimethylformamide (DMF) or γ-butyrolactone (GBA)] and an anti-solvent in which both perovskite precursors are completely insoluble [dichloromethane (DCM)] result the conditions in which all the ionic building blocks of the LHPs to be coprecipitated from solution stoichiometrically[41].

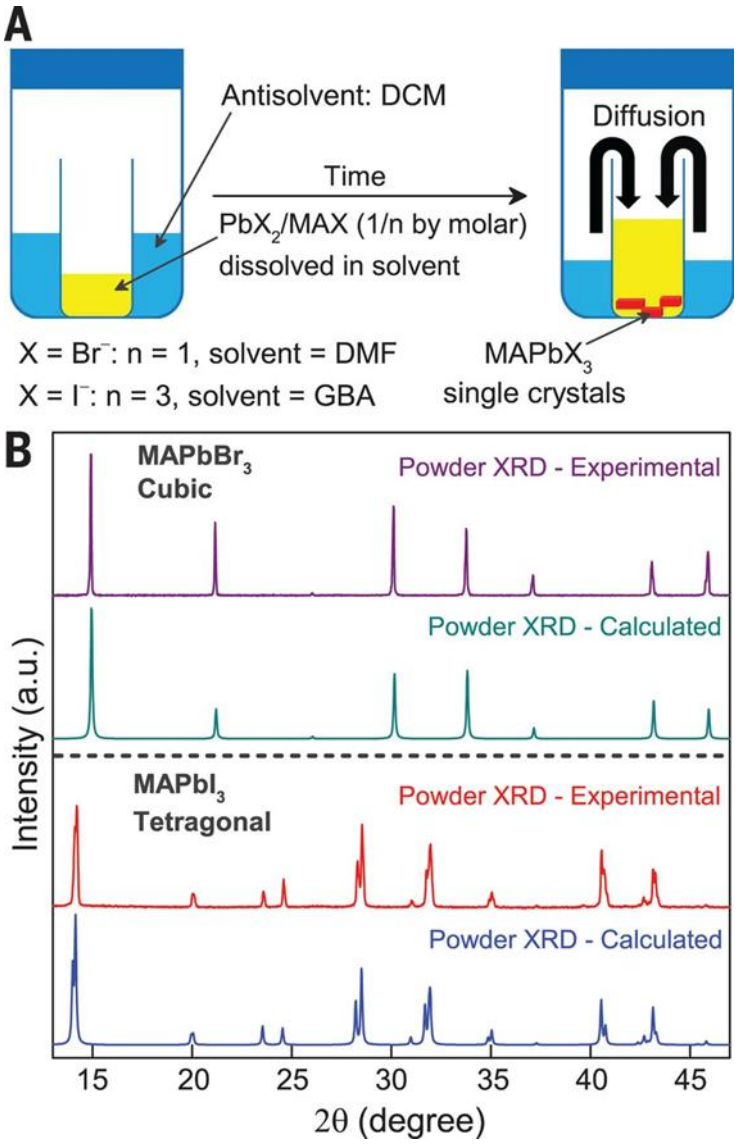

Figure 1.5: A) Schematic diagram of the crystallization process. (B) Experimental and calculated powder XRD profiles confirming the phase purity of $MAPbX_3$ crystals grown at room temperature (Reprinted with permission from ref. 41)

ITC is instead based on inverse temperature solubility behavior of LHPs in certain solvents. Saidaminov et al. demonstrated that the solubility of $MAPbBr_3$ in DMF drops considerably from $0.80\pm0.05\ g\ ml^{-1}$ at room temperature to $0.30\pm0.05\ g\ ml^{-1}$ at 80 °C[71]. This inverse solubility phenomenon was used to crystallize $MAPbX_3$ rapidly in hot solutions as shown in Figure 1.6.

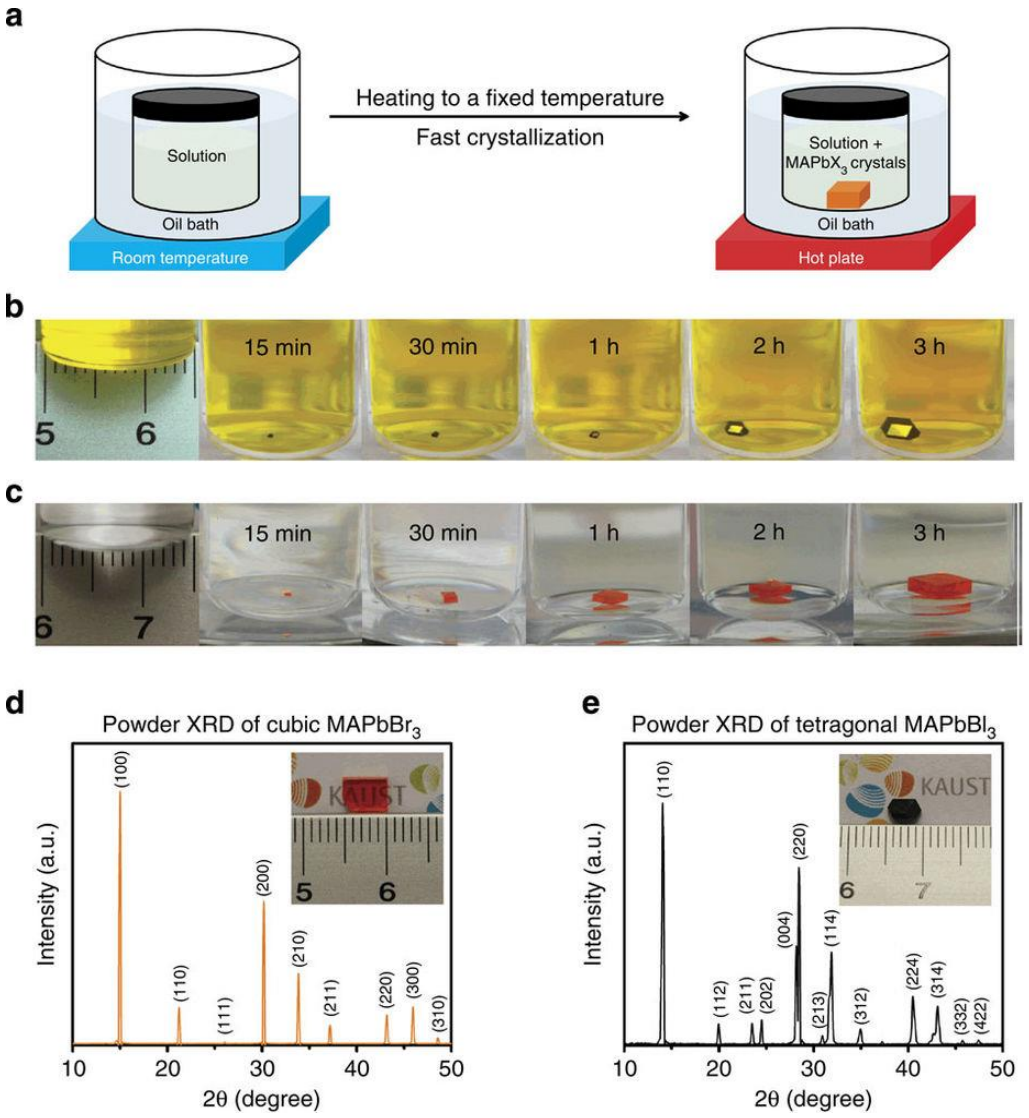

Figure 1.6: (a) Schematic representation of the ITC apparatus in which the crystallization vial is immersed within a heating bath. The solution is heated from room temperature and kept at an elevated temperature (80 °C for $MAPbBr_3$ and 110 °C for $MAPbI_3$) to initiate the crystallization. (b,c) $MAPbI_3$ and $MAPbBr_3$ crystal growth at different time intervals. (d,e) Powder X-ray diffraction of ground $MAPbBr_3$ and $MAPbI_3$ crystals. Insets: pictures of the corresponding crystals grown within a non-constraining vessel geometry. (Reprinted with permission from ref. 71)

in a similar fashion, Dirin et al. found that the growth of $CsPbBr_3$ single crystal is best carried out in dimethyl sulfoxide (DMSO) among other *good solvents*, e.g. DMF or GBA[70].

1.6. Lead Halide Perovskite Nanocrystals

Colloidal semiconductor nanocrystals (NCs) have become an important class of materials with great potential for energy applications (e.g. optoelectronic devices) and opened up a new branch of chemistry. Colloidal synthesis offers advantages of bottom-up approach with a precise control over shape and size and enables systematic studies of structural, electronic and optical properties of such materials[72]. The surfaces of semiconductor NCs are covered by capping ligands that mediate their crystallization and enable steric stabilization of such NCs. Compared with molecules, inorganic phosphors, organic materials, and bulk semiconductors, QDs offer various optical properties. QDs are single crystals of semiconductor material, typically only several nanometers in size. Common examples are cadmium selenide (CdSe), cadmium sulfide (CdS), or zinc sulfide (ZnS) nanocrystals. Their size-dependent optical and electronic properties, making it possible to tune the photoluminescence (PL) of QDs through a wide spectral window by choosing the composition, size and shape of them. These size tunable properties arise from quantum confinement phenomenon, which is a result of the nanocrystal being smaller than the *Bohr exciton* diameter ($2a_B$) (by squeezing the electron and hole to live in a space smaller than the normal equilibrium distance in the bulk material, see Figure 1.7). As a result, the smaller the nanocrystal, the larger the band gap of the material and the bluer the emission from the nanocrystals.

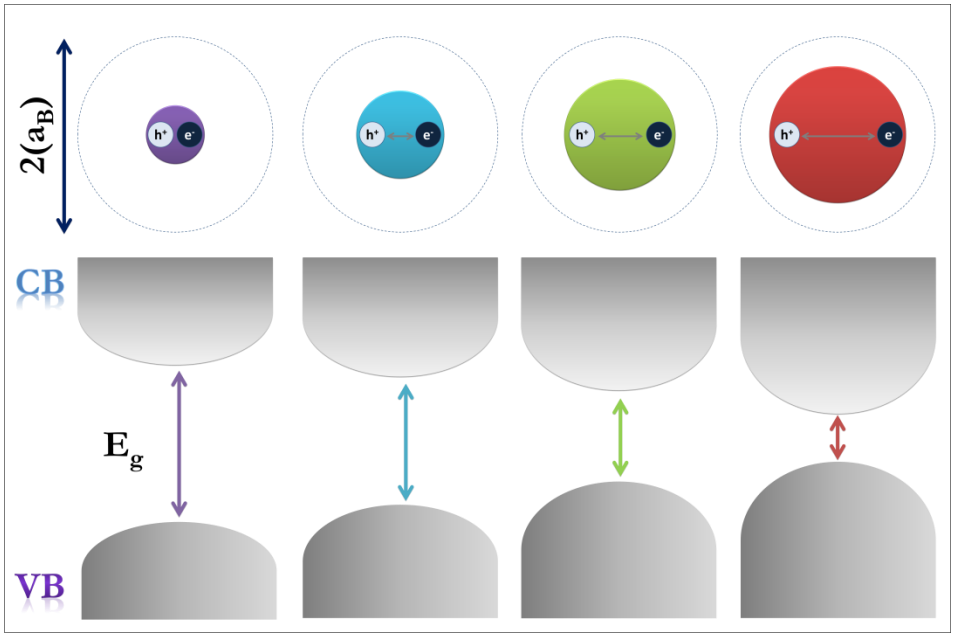

Figure 1.7: Schematic representation of the quantum confinement effect on the energy level structure of a semiconductor material.

In QDs surface atoms possess unsatisfied chemical bonds, resulting unshared atomic orbitals (dangling bonds). These give rise to energy levels within the band gap of the QDs. Surface defects can considerably trap the electron or hole and afford the nonradiative recombination routes. therefore, it is crucial to control the surface of semiconductor NCs and eliminate dangling bonds, e.g. by overgrowing a shell of a wider band gap semiconductor[73, 74]. In order to achieve strongly emissive QDs, heterostructure architectures are desirable for such QDs which are typically composed of a core, and one or more shells with wider band gap (Figure 1.8)[72].

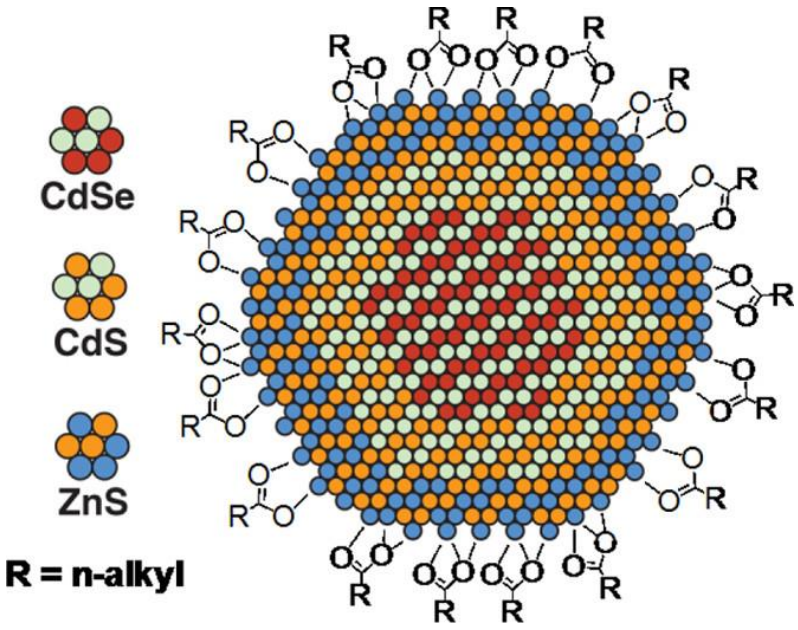

Figure 1.8: Representative of quantum dot heterostructure. An emissive CdSe core is shelled in increasingly electrically insulating CdS and ZnS layers that improve the luminescence efficiency. Surface bound ligands (e.g. carboxylates) are bound to a metal enriched surface. (Reprinted with permission from ref. 72)

In parallel to work on classical colloidal semiconductor NCs, a brilliant discovery of methyl ammonium lead iodide ($MAPbI_3$) in the form of nanometer-scale[75] crystals as promising PV material in 2011 has attracted the colloidal chemistry community into such new class of medium-bandgap semiconductors. few month later, highly luminescent $MAPbBr_3$ perovskite nanoparticles were synthesized on TiO_2 mesoporous nanocrystalline films[76]. This work was indeed another sign to point out the potential of LHP NCs for optoelectronic application. The first solution-based colloidal approach to grow LHP NCs was reported by Schmidt et al.in 2014 with the photoluminescence quantum yield (PLQY) of 20%[77].

Although the luminescence of nanosized aggregated $CsPbX_3$ phase was initially observed in CsX single crystal hosts in 1997[78], but Protesescu et al. nicely delivered this phase into colloidal chemistry and developed the monodisperse $CsPbX_3$ NCs by the adaption of classical hot-injection method in 2015[79]. These last two reports indeed triggered the vast investigation of scientists from various fields on such

materials. The major attribute of LHP NCs compared with bulk is the impressive PLQY (up to near unity) which again manifest the impact of colloidal chemistry (such as precise control over shape, size and surface passivation) on the optical properties of LHPs (Figure 1.9).

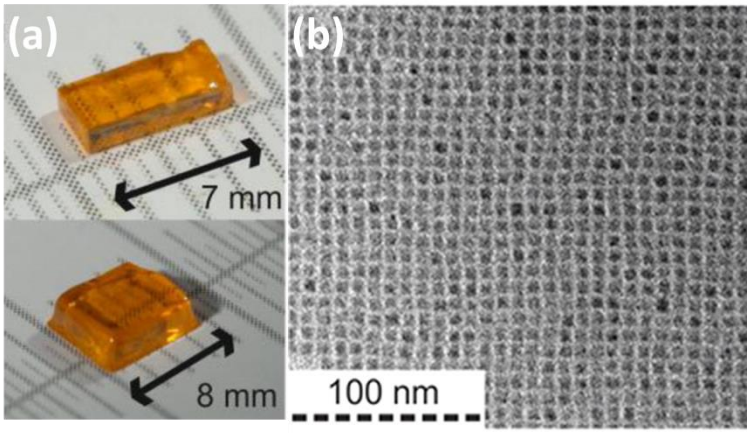

Figure 1.9: Downsizing the LHPs by colloidal synthesis approach; (a) bulk crystals and (b) nanocrystals of $CsPbBr_3$ (Adapted with permission from ref. 70 and ref. 70)

In contrast to classical QDs, LHP NCs have a soft and rather ionic lattice, and their optical and electronic properties are highly tolerant to structural defects and surface states, meaning that surface defects impart no significant detrimental effects to the photophysics of LHP NCs. This unique feature arises from the fact that defects reside in relatively shallow states within the bandgap[24, 33].

1.7. Ligand Assisted Reprecipitation (LARP) Technique

Reprecipitation synthesis is a very simple and available technique through mixing solvent and has been widely applied to prepare organic nanoparticles and polymer dots[80]. After the advent of LHPs, different groups employed this method to synthesize LHP NCs by adding proper ligands to control size and shape of the NCs[77, 81-83]. Typically this technique is accomplished by simply mixing a solution of LHP precursors in a good solvent (e.g. DMF) into a vigorously stirred poor solvent (e.g. toluene) with long chain organic ligands (normally amine and acid), which subsequently results in the controlled crystallization of precursors into colloidal nanoparticles[84]. This facile approach enables to produce different shapes of LHPs even at room temperature, such as spherical quantum dots, nanocubes, nanorods, and nanoplatelets by varying the capping ligands (Figure 1.10)[81].

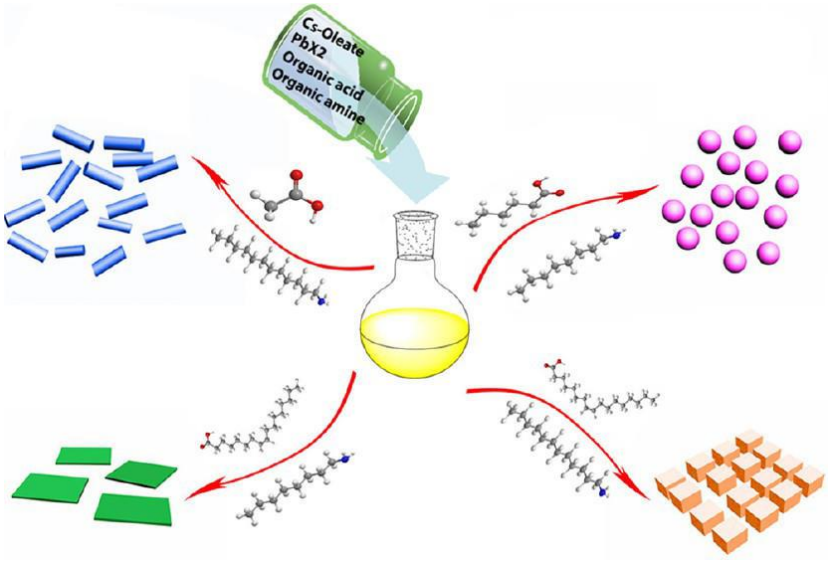

Figure 1.10: Schematic illustrating the formation process for different $CsPbX_3$ (X = Cl, Br, I) nanocrystals mediated by organic acid and amine ligands at room temperature. Hexanoic acid and octylamine for spherical quantum dots; oleic acid and dodecylamine for nanocubes; acetate acid and dodecylamine for nanorods; oleic acid and octylamine for few-unit-cell-thick nanoplatelets. (Reprinted with permission from ref. 81)

The main drawback of this technique (especially in large-scale synthesis) is the broad size distribution of resulting NCs which is originated from the inhomogeneous mixing of the solvents. It's worth mentioning that the LARP is not a reliable and successful method to synthesize iodide-based perovskite NCs, as the residues of DMF on the surface of NCs destabilize the α-phase[85]. Nucleation and growth at room temperature again manifest the fact that the chemical bonding in LHPs is intrinsically much more ionic than in the more rigid, highly covalent lattices of metal chalcogenides which require elevated synthesis temperatures in order to promote crystallization.

1.8. Hot Injection Technique

Following the classical hot-injection method, which is frequently used for the synthesis of colloidal metal chalcogenide NCs, Protesescu et al. launched the fabrication of $CsPbX_3$ (X = Cl, Br, I and their mixtures) NCs by adapting such technique[79]. Generally, the nucleation and growth of $CsPbX_3$ NCs is triggered by the swift injection of cesium oleate into an octadecene solution containing PbX_2, oleic acid (OA), and oleylamine (OLA) at high temperatures (normally in the range of 140 – 200°C) as expressed below and shown in Figure 1.11[86]:

$$2\text{Cs-oleate} + 3PbX_2 \rightarrow 2CsPbX_3\ \text{NCs} + Pb(\text{oleate})_2$$

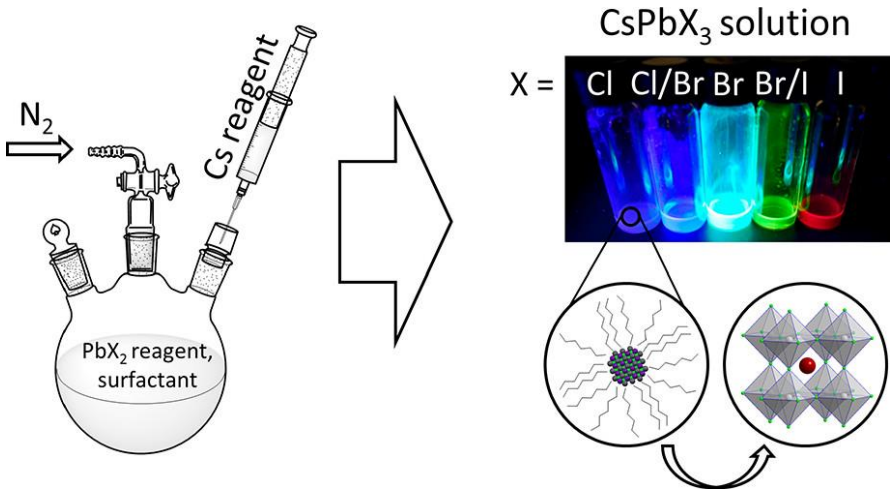

Figure 1.11: Scheme of the hot injection synthesis (Reprinted with permission from ref. 86)

Similar to LARP technique, hot injection method has also extended to produce other members of perovskite family, such as $MAPbX_3$ and $FAPbX_3$ NCs[87, 88]. One problem with the hot injection synthesis of these NCs is that both nucleation and growth occur swiftly. Critical steps of this synthesis scheme are the fast injection of a preheated solution of cesium oleate (CsOA) and a fast cooling that follows immediately after that, which makes it hard to control their size, upscale the process and more in general to test variants in a reproducible fashion.

Thanks to nuclear magnetic resonance (NMR) spectroscopy, De Roo et al. elucidated that capping ligands are not tightly bound to the NC surface and can easily leave the surface during the isolation and purification procedures. This because LHP NCs are ionic in nature and the interactions with capping ligands are also more ionic and labile[89].

Recently, various approaches have been reported as alternative methods to synthesize LHP NCs, such as microwave assisted[90, 91], droplet-based microfluidic[92], ultrasound assisted[93], solvothermal[94], etc. Almost all of them yield highly emissive LHP NCs that again highlight the defect tolerance feature of LHP NCs compared with classical QDs.

1.9. Light-Emitting Applications

As discussed earlier, LHP NCs are highly luminescent and emit over the full visible range (400-700 nm[95, 96], the emission can even be extended into the infrared by replacing Cs or MA with FA[97]). The high PLQYs without the benefits of core-shell passivation (can reach to near unity[98, 99]) and very narrow emission linewidths (FWHM of 12-50 nm) making them ideal candidates for luminescent display

applications. In addition, the quantum confinement effect can afford an interesting way to tune the emission of fully-inorganic perovskites NCs, which is a prerequisite for various light-emitting applications[3, 100]. Interestingly, LHP NCs can emit polarized light either in solution (e.g. hexane) or in film without using extra polarizer due to the movement of halide ions together with the well-ordered spatial arrangement of NCs[101]. Different groups demonstrated the amplified spontaneous emission (ASE) from such NCs in the whole visible spectral region with low pump thresholds (e.g., 2.2 μJ cm^{-2})[102] which make them interesting as new quantum materials for lasing[103].

Figure 1.12 presents development approaches for the first through fifth generations of general white-light LED lighting devices[104]. Recent promising works provide an opportunity to replace traditional down-converting phosphors in white light LEDs with direct red, green, blue perovskite emitters, producing low-cost, high quality white lights and high resolution displays. Perovskites can surmount the shortcomings of both traditional LEDs (high efficacy but expensive) and emerging LED technologies such as quantum dots (QLEDs) and organics (OLEDs) (low-cost and tunable but low brightness) by producing bright, inexpensively-produced LEDs with an emission spectrum that can be adjusted to any desired spectral output by tuning material compositions or dimension. This would allow manufacturers to provide a range of white light shades to suit the preferences of all consumer markets with a single production line[105].

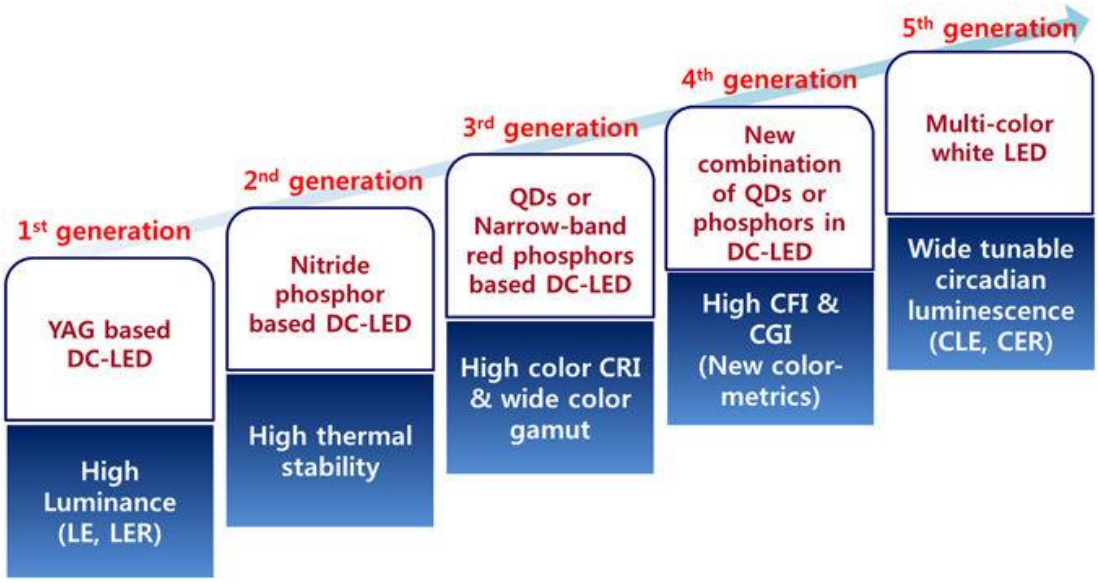

Figure 1.12: Schematic diagram of the development approaches for the first through fifth generations for general WLED lighting devices. [Luminous efficacy (LE), luminous efficacy of radiation (LER), color rendering index (CRI), color fidelity index (CFI), color gamut index (CGI), circadian luminous efficacy (CLE), and circadian luminous efficacy of radiation (CER)]. (Reprinted with permission from ref. 104)

1.10. Outline

In this thesis, we aim to develop different synthetic routes for LHP NCs in order to understand the effect of various approaches (such as hot injection, heat up, cation exchange and reprecipitation methods) on the size, shape and consequently the optical properties of such materials. We focus on the chemistry of these approaches including the effect of ligands, precursors and solvents on the structural and optical properties. This knowledge will allow us to move rationally towards large-scale synthesis and enable to translate the high performance of nanocrystals into solid films for optoelectronic applications.

In **chapter 3**, we modify the standard hot injection method for the $CsPbBr_3$ NCs to break the crystal symmetry and promote the anisotropic growth of such NCs. We report the colloidal synthesis of $CsPbBr_3$ nanoplatelets (NPLs) which enable us to study the 1D confinement of the carriers. We further investigate the impact of lateral size of such platelets on photoluminescence by growing nanosheets (NSs) and preserving the thickness in the confine regime. The role of capping ligands is investigated and finally resulting NSs are fully characterized.

Chapter 4 presents a heat up method to synthesize $CsPbBr_3$ NPLs and compares that with the hot injection approach which is developed in chapter 3. We show that the heat up method is a better choice for the large-scale synthesis of uniform $CsPbBr_3$ nanoplatelets. Moreover, resulting nanoplatelets preserve their optical properties in solid state due the their unique stacked lamellar structures. We then show that such self-assembled platelets can transform to the green-emitting belts by UV-light irradiation. This results in stable and highly emissive perovskite thin films with a record PLQY of 65%. Finally we demonstrate the potential of such films for optoelectronic applications.

Chapter 5 reports an alternative chemical route to synthesize monodisperse $CsPbX_3$ NCs by employing colloidal CsX NC precursors. The main goal of this chapter is finding an indirect method to grow the perovskite domain which somewhat enable us to control the fast nucleation and growth of $CsPbX_3$ NCs. We develop a facile colloidal synthesis of CsX NCs and their transformation to $CsPbX_3$ NCs by studying the intermediate stages under high resolution microscopy.

In **chapter 6** we focus on the chemistry of another member of the lead-halide perovskite family called $MAPbX_3$ in both NCs and bulk forms. We explore a new solvent to dissolve PbX_2 salts in the LARP technique. We show that N-methylformamide as a good solvent can also act as a source of A-site cation and release methyl ammonium cation into the reaction medium via either hydrolysis or

transamidation processes. Both mechanisms are proved by NMR. We optimize all related parameters to grow $MAPbX_3$ bulk- and nano-crystals. Finally we show that such method can be easily scaled up to yield large amount of $MAPbBr_3$ NCs.

In the last **Chapter 7**, conclusions as well as outlook for further investigations on the topic of the thesis are presented.

2. Chemicals & Instruments

"All chemicals were used without any further purification"

2.1. Precursors

Lead(II) bromide ($PbBr_2$, 99.999% trace metals basis), lead(II) iodide (PbI_2, 99.999% trace metals basis), lead(II) acetate trihydrate ($Pb(Ac)_2$, 99%), Lead(II) thiocyanate ($Pb(SCN)_2$, 99.5% trace metals basis), lead(II) oxide (PbO, 99.999%), zinc chloride ($ZnCl_2$, 99.999%), zinc bromide ($ZnBr_2$, 99.999%), zinc iodide (ZnI_2, 99.999%), cobalt(II) chloride ($CoCl_2$, 97%), cobalt(II) bromide ($CoBr_2$, 99%), indium (III) chloride ($InCl_3$, 99.99%), tetrabutylammonium chloride (TBAC, 97%), tetrabutylammonium bromide (TBAB, 99%), tetrabutylammonium iodide (TBAI, 99%) cesium carbonate (Cs_2CO_3, reagentPlus, 99%), hydrochloric acid (HCl, ACS reagent, ≥37%), hydrobromic acid (HBr, 48 wt % in H_2O), hydriodic acid (HI, 57 wt % in H_2O) were purchased from Sigma-Aldrich.

Lead(II) chloride ($PbCl_2$, 99.999% trace metals basis), was purchased from Alfa Aesar.

2.2. Capping ligands

Oleylamine (OLA, 70%), oleic acid (OA, 90%), octanoic acid (OctAc, 99%), octylamine (OctAm 99,5%) were purchased from Sigma-Aldrich.

2.3. Solvents

1-Octadecene (ODE, technical grade, 90%), hexane (anhydrous, 95%), toluene (anhydrous, 99.8%), N-Methylformamide (NMF, 99%), N-Ethylformamide (NEF, ≥99.0% (GC)), chloroform ($CHCl_3$, anhydrous, 99.95%), 1,2-dichlorobenzene (DCB, anhydrous, 99.8%) and 2-propanol (IPA, anhydrous, 99.5%) were purchased from Sigma-Aldrich.

2.4. Transmission Electron Microscopy (TEM)

Conventional TEM images were acquired on a JEOL JEM-1011 microscope equipped with a thermionic gun at 100 kV accelerating voltage. High-resolution TEM (HRTEM) imaging was performed on a JEOL JEM-2200FS microscope equipped with a 200 kV Schottky gun, a CEOS image aberration corrector enabling a spatial resolution of 0.9 Å, and an in column Ω-filter. A Bruker Quantax 400 energy dispersive X-ray spectrometry (EDS) system with an XFlash 5060 detector on the same microscope was used for the elemental analysis. The samples were prepared by drop-casting diluted NC suspensions onto 200 mesh carbon-coated copper grids for conventional TEM imaging, and ultrathin

carbon/holey carbon coated 400 mesh copper grids for HRTEM imaging, respectively. Geometrical phase analysis (GPA) was performed on HRTEM images using the FRWRtools plugin for Digital Micrograph® (Gatan, Inc.).

2.5. Scanning electron microscope (SEM)

The SEM micrographs were acquired using a Helios Nanolab 620 (FEI Company) dual-beam system. High resolution scanning electron microscopy (HR-SEM) images were acquired using a FEI Nova 600 NanoLab instrument.

2.6. Powder X-ray Diffraction (XRD) Analysis

XRD patterns were obtained using a PANalytical Empyrean X-ray diffractometer equipped with a 1.8 kW Cu Kα ceramic X-ray tube, PIXcel3D 2×2 area detector and operating at 45 kV and 40 mA. The diffraction patterns were collected in air at room temperature using Parallel-Beam (PB) geometry and symmetric reflection mode. All XRD samples were prepared by drop casting a concentrated solution on a zero diffraction silicon wafer.

2.7. Optical Absorption and Photoluminescence Spectroscopy

The optical absorption spectra were taken on a Varian Cary 5000 UV−vis−NIR spectrophotometer. Samples were prepared by diluting the NC solutions in toluene in 1 cm path length quartz cuvettes. Photoluminescence quantum yield (PLQY) measurements of the NCs were carried out with an Edinburgh Instruments fluorescence spectrometer (FLS920) equipped with a Xenon lamp with monochromator for steady-state PL, and a time-correlated single photon counting unit coupled with a pulsed laser diode (λ = 405 nm, pulse width = 50 ps) for time-resolved PL. PLQY values were obtained from NC solutions in a quartz cuvette and diluted to 0.1 optical density at the excitation wavelength (λ = 400 nm) using a calibrated integrating sphere.

2.8. Atomic Force Microscopy (AFM)

AFM images were acquired employing a Nanowizard III (JPK Instruments, Germany) in intermittent contact mode, in air. Single-beam uncoated silicon cantilevers (OMCL-AC160TS-W, Olympus) with a nominal tip radius of curvature of 10 nm and typical cantilever resonance frequency of 300 kHz were used. Quantitative Imaging mode (QI – JPK Instruments) was used in order to determine simultaneously sample topography, adhesion and elasticity (Young's Modulus). QI is based on the acquisition of a large set of force-distance curves and on the reconstruction of the sample topography from the tip position at the specific force load. Local mechanical properties of the sample can be extracted from the analysis of the acquired curves. QI images deriving from 128x128 force-distance (FD) curves, with maximum force

load of 4 nN. For each curve, tip speed was 20 μm/s and curve length was 100 nm. For the determination of the absolute value of Young's Modulus each single FD curve was fitted with the Hertz model, the tip was approximated as spherical and with a radius of 30 nm.

2.9. Confocal Microscopy

The fluorescence imaging has been carried out by a Nikon A1 MP confocal microscope (Nikon Instruments, Tokyo, Japan). For all the images we excited the sample with a pulsed laser at 405nm and 40 MHz of repetition rate (LDH-D-C-405, PicoQuant GmbH, Berlin, Germany). We used a 100x 1.4 NA oil immersion objective and we kept the pinhole size at 1 Airy unit. The pixel dwell time was 5 μs and 8 line averages. The fluorescence was acquired over two channels, in the 425 - 475 nm and in the 500 - 550 nm spectral windows, by two GaAsP photomultipliers tubes respectively. The samples were prepared by drop casting 20 μl NCs in Hexane solution. In order to reduce the evaporation, we sealed the coverslip onto a glass slide.

2.10. Nuclear magnetic resonance (NMR)

All NMR spectra were recorded on a Bruker AvanceIII 400 MHz spectrometer equipped with a BBI probe.

3. Colloidal Synthesis of Cesium Lead Bromide ($CsPbBr_3$) Nanoplatelets and Nanosheets with Tunable Optical Properties via Anion Exchange Reactions

Abstract: We report the nontemplated colloidal synthesis of single crystal $CsPbBr_3$ perovskite nanoplatelets, nanosheets (with lateral sizes up to a few micrometers) with thickness of just a few unit cells (i.e., below 5 nm), hence in the strong quantum confinement regime. While adding more oleic acid to the standard protocol of $CsPbBr_3$ cubes resulted nanoplatelets, introducing short ligands (octanoic acid and octylamine) in the synthesis together with longer ones (oleic acid and oleylamine) yielded large sheets in quantum confinement regime. The lateral size is tunable by varying the ratio of shorter ligands over longer ligands, while the thickness is mainly unaffected by this parameter and stays practically constant at 3 nm in all the syntheses conducted at short-to-long ligands volumetric ratio below 0.67. Beyond this ratio, control over the thickness is lost and a multimodal thickness distribution is observed. We then study the effects of high energy (80/200 keV) electron irradiation on as-prepared nanosheets. Our results show that the $CsPbBr_3$ nanosheets undergo a radiolysis process, with electron stimulated desorption of a fraction of bromine atoms and the reduction of a fraction of Pb^{2+} ions to Pb^0. Subsequently Pb^0 atoms diffuse and aggregate, giving rise to the high contrast particles. The diffusion is facilitated by both high temperature and electron beam irradiation.

Parts of this chapter have been adapted or reproduced with permission from:

Shamsi, J.; Dang, Z.; Bianchini, P.; Canale, C.; Stasio, F. D.; Brescia, R.; Prato, M.; Manna, L., Colloidal Synthesis of Quantum Confined Single Crystal CsPbBr3 Nanosheets with Lateral Size Control up to the Micrometer Range. Journal of the American Chemical Society 2016, 138, 7240-3.

3.1. Introduction

The rise of graphene[106] has ignited global interest in noncarbon-based ultrathin two-dimensional (2D) nanomaterials, such as transition metal dichalcogenides, layered metal oxides, and hexagonal boron nitride, to name a few[107-110]. Several synthetic methods have been developed for the preparation of 2D nanomaterials, including bottom-up wet chemistry routes. The latter have rapidly evolved to the point that they can now deliver 2D nanostructures also for nonlayered materials, such as noble metals, metal oxides, and metal chalcogenides[111]. These 2D nanomaterials offer unique advantages over their 3D counterparts, in addition to the increased specific surface area. In particular, 2D colloidal semiconductor nanocrystals exhibit remarkable optical properties[112, 113]: their absorption edges and the emission spectra are narrow (even below 10 nm at room temperature), their PLQY is typically high, in the 30−80% range, and their PL lifetimes are usually fast, making them good candidates for light emission applications. These optical properties are strictly dependent on the sheet/platelet thicknesses, which can be finely tuned in colloidal synthesis by a proper choice of the organic surfactants that are used to control the growth. When seeking for a synthesis route to prepare nanoplatelets or nanosheets of a nonlayered material, it is critical to break the crystal symmetry and promote anisotropic growth. In the case of organic-inorganic hybrid perovskite, few works have addressed the colloidal synthesis of $MAPbBr_3$ (MA = methylammonium) nanoplatelets (NPLs) with confined thickness[100, 114], while in another work layered $(C_4H_9NH_3)_2PbBr_4$ nanosheets were directly grown on a SiO_2/Si substrate and then detached from the substrate and suspended in solution[115]. Several reports have dealt with shape control in the colloidal synthesis of fully inorganic $CsPbX_3$ (X being a halide) nanocrystals. Zhang et al. observed the evolution of $CsPbX_3$ (X = Br, I) nanocubes to nanowires (NWs) by increasing the reaction time from few seconds up to 60 min in a synthesis that was initially used to prepare nanocubes[116]. At a reaction time around 30 min, the sample consisted of a mixture of NWs and square-shaped nanosheets (NSs) of 100 nm lateral dimensions. Sun et al. reported shape control of $CsPbX_3$ perovskite via a reprecipitation process at room temperature, which yielded green emitting NPLs/NSs with edge length of around 100 nm[81]. Recently, two colloidal routes were reported on the anisotropic growth of all inorganic $CsPbBr_3$ NPLs exhibiting a strong 2D confinement of the carriers. In one of them, our group devised a room temperature synthesis to $CsPbBr_3$ NPLs with monolayer-level thickness control in the 3-5 unit cells range[117]. In the other work, Bekenstein et al. observed that the procedure to prepare $CsPbBr_3$ nanocubes[79], when carried out at temperatures in the 90-130 $^{\circ}$C range, yields NPLs[118]. In the same synthesis scheme, no particles were formed at temperatures as low as 70 °C, while at 150 °C nanocubes

were synthesized. The prepared NPLs could then undergo lateral oriented attachment, forming nanosheets (NSs) with lateral size up to 200 nm.

In this chapter we report the synthetic routes for the colloidal orthorhombic $CsPbBr_3$ NPLs and NSs with thickness in the range of 3-5 unit cells (i.e., around 3 nm). The lateral dimensions varies from 30 - 50 nm for NPLs to 0.3 – 5 μm for NSs. We also show that the composition of the NSs can be varied all the way to $CsPbCl_3$ or $CsPbI_3$ by anion exchange, with preservation of the size and shape of the starting particles. We further show that the $CsPbBr_3$ nanosheets undergo a radiolysis process under high energy electron irradiation.

3.2. Experimental Section

Preparation of cesium-oleate solution:

0.032 g Cs_2CO_3 and 10 mL OA were loaded into 25 mL 3-neck flask, dried for 1h at 120 ºC under vacuum, and then heated under N2 to 140 ºC until all Cs_2CO_3 reacted with OA.

Synthesis of $CsPbBr_3$ NPLs:

10 mL ODE, 0.013g $PbBr_2$, 500 μL OA, 500 μL OLA were loaded into a 25 mL 3-neck flask and dried under vacuum for 20 minutes at 100 ºC. After complete solubilization of the $PbBr_2$ salt, the temperature was increased to 130 ºC under N_2 and 1 mL of Cs-oleate solution (prepared as described above) was swiftly injected. After 5 minutes, the reaction mixture was slowly cooled to room temperature using a water bath.

Synthesis of $CsPbBr_3$ NSs:

10 mL ODE, 0.013g $PbBr_2$, 250 μL OA, 250 μL OLA, and a proper volume of OctAm and OctAc (e.g. 400 μL to obtain NSs of lateral size close to 1 μm, see main text for details) were loaded into a 25 mL 3-neck flask and dried under vacuum for 20 minutes at 100 ºC. After complete solubilization of the $PbBr_2$ salt, the temperature was increased to 150 ºC under N_2 and 1 mL of Cs-oleate solution (prepared as described above) was swiftly injected. After 5 minutes, the reaction mixture was slowly cooled to room temperature using a water bath.

Isolation and purification of $CsPbBr_3$ NPLS & NSs:

To collect the NSs, 10 mL of hexane was added to the crude solution and then the mixture was centrifuged at 3000 and 700 RPM (for NPLs and NSs, respectively) for 5 min. After centrifugation, the supernatant was discarded and the NPLs/NSs were redispersed in hexane. It has to be noted that, due to the large area of our nanosheets, they show a natural tendency to aggregate in solution over time, and we observed a gradual shift of the PL wavelength from blue to green (i.e. towards the emission value of non-confined bulk-like $CsPbBr_3$ structures). This effect is even stronger on cleaned samples, where the centrifugation step is likely responsible for a not-negligible loss of surface ligands, thus facilitating the aggregation of nanosheets and their evolution to thicker assemblies. It is nonetheless interestingly to remark that, if fresh diluted solutions are used to prepare films of these NSs either by spin coating or drop casting, followed by gentle dipping in pure solvent to remove the excess of organics (as done in the preparation of the samples for AFM characterization, see main text), the quantum confinement can be preserved.

3.3. Results & Discussion

The process is carried out using standard air-free techniques and is an evolution of the synthesis reported by Protesescu et al[79]. Our major change is to use Cs-oleate dissolved in oleic acid (OA) instead of octadecene (as done instead in the work of Protesescu et al.). This change alone leads to NPLs and not to cubes, over a wide temperature range (from 50 to 150 °C, see Figure 3.1), differently from Bekenstein et al., who could get NPLs only in a narrower temperature range[118].

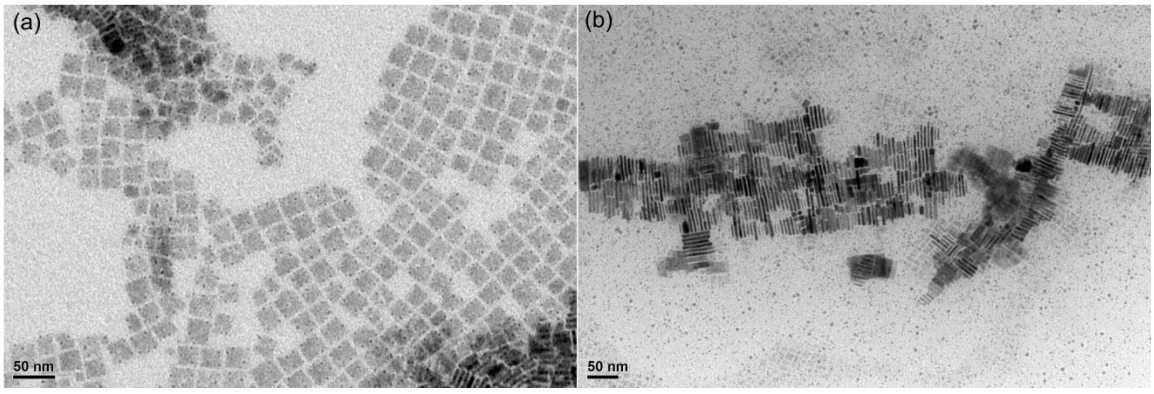

Figure 2.1: TEM images of NPLs prepared by using the solution of Cs-oleate in OA instead of hot solution of Cs-oleate in ODE. Reaction conditions: 0.013 $PbBr_2$, 10 mL ODE, 500µL OA, 500µL OLA. Reaction temperature, (a) 50°C, (b) 150 °C.

However, the best quality NPLs with unimodal thickness distribution were synthesized at 130°C with a blue shift of PL as a result of confinement effects. We attribute this effect to the excess amount of oleic acid which produces more oleylammonium cations in the solution (Figure 3.2).

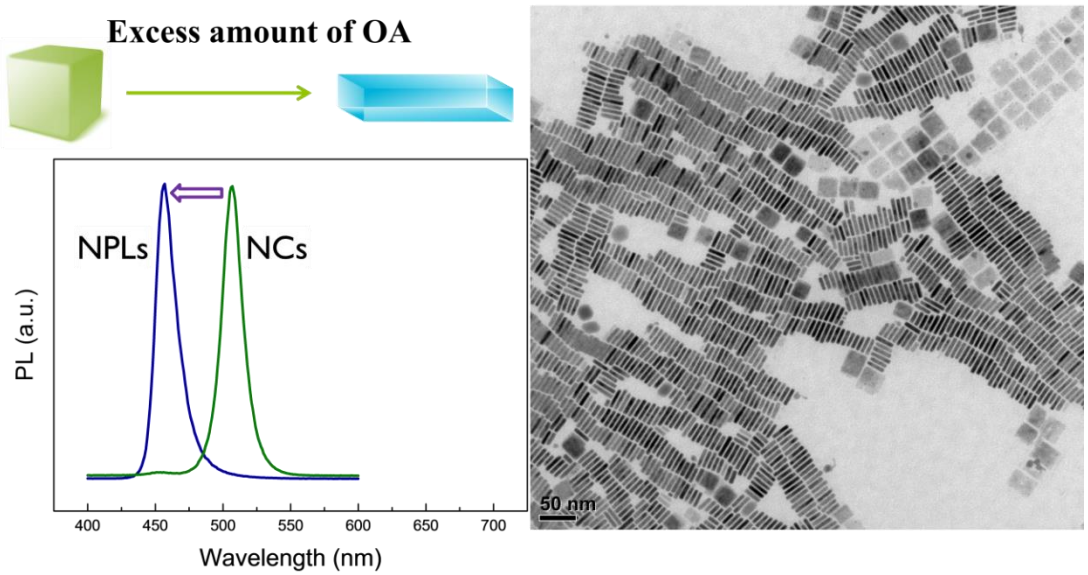

Figure 3.2: $CsPbBr_3$ NPLs; the effect of adding more oleic acid. Reaction conditions: 0.013 $PbBr_2$, 10 mL ODE, 500µL OLA, 500µL OA, reaction temperature: 150 °C

In our initial scheme, tuning of the lateral size of the NPLs (from 50 to 200 nm) was possible by varying the reaction time (from a few seconds up to a few minutes). However, the NPLs would grow in thickness as well, as their PL emission shifted from 450 nm (compatible with a thickness of approximately 3 nm, as calculated with the empirical formula by Sun et al.[81]), to 510−520 (compatible with a thickness of 7-8 nm, therefore out of the strong confinement regime) and led to a multimodal thickness distribution (Figure 3.3).

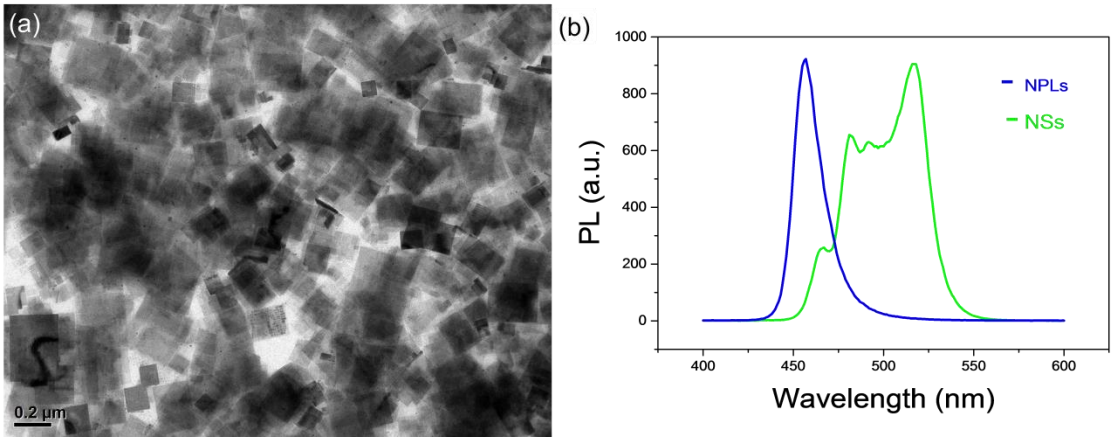

Figure 3.3: Promoting the growth in lateral size by increasing reaction time from few seconds up to two minutes. Reaction conditions: 0.013 $PbBr_2$, 10 mL ODE, 500µL OA, 500µL OLA, reaction temperature: 150 °C. (a) TEM image of NSs synthesized by increasing the reaction time; (b) Comparison of the PL spectra of NPLs (Figure 3.1.b) with that of as-prepared NSs.

A second change in the synthesis was to introduce shorter ligands (in addition to OA and OLA of the standard protocol), namely, octanoic acid (OctAc) and octylamine (OctAm). By varying the ratio of

these two short ligands over that of the longer ligands (OA and OLA), we could control the lateral size of the particles, which could be tuned from 300 nm up to 5 μm (with a higher ratio of short to long ligands yielding larger nanosheets), while at the same time the thickness remained fixed at 5 unit cells (2.5−3 nm, see Table 3.1).

Table 3.1: Reaction conditions for the synthesis of NSs with various lateral sizes and summary of the relevant geometrical and optical properties: average size, half width at half-maximum (HWHM) of the size distribution, PL wavelength, and estimated thickness[a]

OctAc volume (= OctAm volume)	short/long ligands volumetric ratio (X)	NS <size> (nm) / size distribution HWHM (nm)	PL (nm) (±2 nm)	Estimated thickness[81] from PL position
250 μL	0.33	280 / 120	452	2.7 nm
300 μL	0.40	610 / 120	458	2.9 nm
400 μL	0.52	975 / 200	458	2.9 nm
500 μL	0.67	5160 / 1300	458; 491	2.9 nm; 4 nm

[a] In all reactions, 250 μL of OA and 250 μL of OLA are used as long chain ligands. An additional 1 mL of OA is added with the Cs precursor

The use of short ligands therefore enabled the synthesis of NSs with large lateral dimensions and in which the vertical dimension was always in the strong quantum confinement regime. Although OctAc alone could be used as short ligand to promote the lateral growth of the sheets (see Figure 3.4a), in that case the quality of the NSs, in terms of lateral size distribution, was not as good as when OctAm was added to OctAc. However, when using OctAm alone as a short ligand, no sheets were obtained but only a mixture of large crystals and thin NPLs/NSs (see Figure 3.4b). Therefore, the use of both short ligands in conjunction was necessary. Similar results were found when working with nonanoic acid instead of OctAc (data not shown).

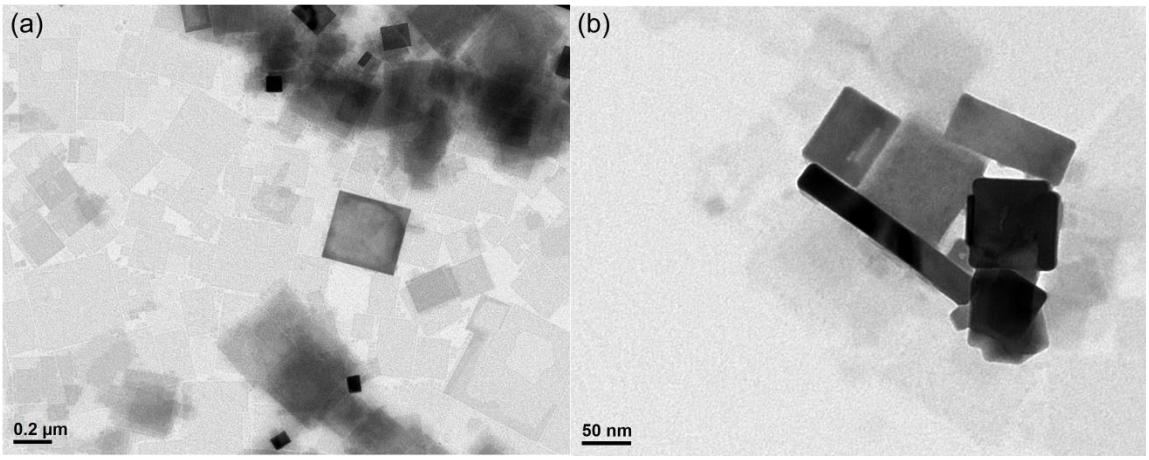

Figure 3.4: Role of short ligands. TEM images of products which were synthesized by adding only (a) 500 µL OctAc or (b) 500 µL OctAm. Reaction conditions: 0.013 $PbBr_2$, 10 mL ODE, 250µL OA, 250µL OLA, reaction temperature: 150 ◦C, reaction time: 5 min.

Other parameters that were found critical in controlling the shape and the thickness of the sheets were the temperature and the reaction time. The optimal temperature range for growth was 145−155 °C. Temperatures above 155 °C led to sheets with an addition of various byproducts (including cubes), whereas below 145 °C the growth was slow and the shape of the NSs was not regular, with nonsharp edges (see Figure 3.5). The optimal growth time was up to 5 min. Attempts to grow larger sheets by increasing the reaction time resulted in aggregation of the particles. Therefore, lateral size control was best achieved by tuning the ratio of short to long ligands rather than by increasing the reaction time over 5 min (see Figure 3.6). The role of short ligands in promoting NS growth and in fine tuning the lateral size, and especially in depressing the growth rate in the vertical direction, is presently unclear and will require further scrutiny. The marked instability of the early aliquots from the synthesis under the electron beam of the TEM made it difficult to perform detailed structural and morphological analyses on them, and therefore to advance solid hypotheses on the growth mechanism (whether this proceeds by oriented attachment or by addition of monomers to initially formed nuclei).

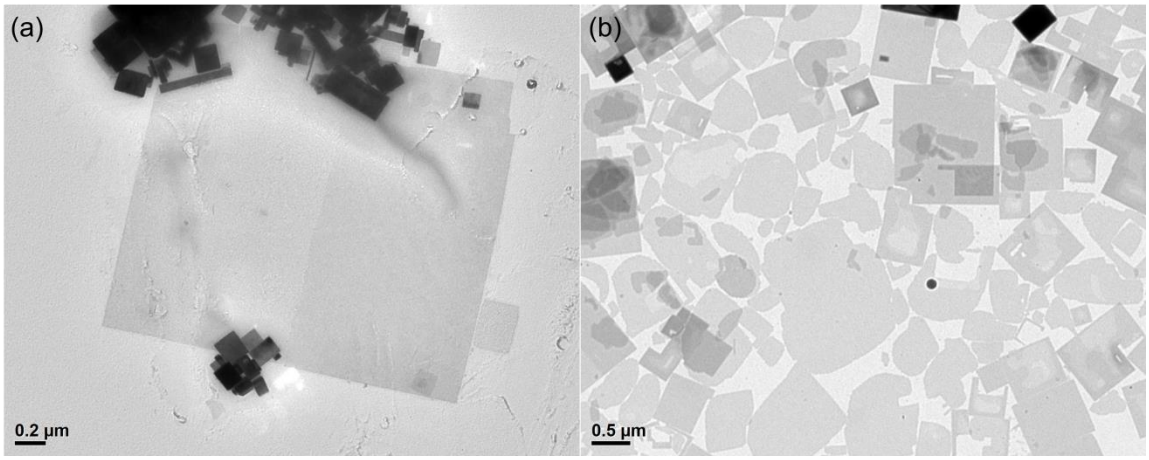

Figure 3.5: The effect of reaction temperature. TEM images of products at (a) 160°C (b) 140°C. Reaction condition: 0.013 $PbBr_2$, 10 mL ODE, 250µL OA, 250µL OLA, 500 µL OctAc, 500 µL OctAm, , reaction time: 5 min.

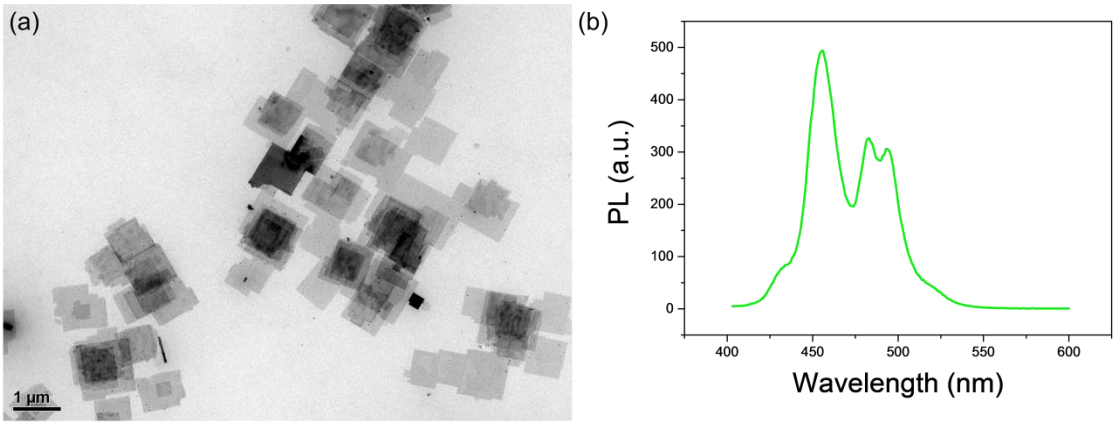

Figure 3.6: The result of increasing reaction time up to 6 min. (a) TEM image and (b) PL spectrum of aggregated NSs. Reaction conditions: 0.013 $PbBr_2$, 10 mL ODE, 250µL OlAc, 250µL OlAm, 500 µL OctAc, 500 µL OctAm, , reaction temperature: 150 °C.

Typical (TEM) images of the NSs prepared at different short to long ligand volumetric ratios (henceforth defined as "X") are reported in Figure 3.7, along with histograms of lateral size distributions and PL spectra. In all cases, the shapes of the NSs were roughly squared and with sharp edges, supporting a single crystalline nature for each of them. The NSs synthesized when working at X = 0.33 (see Figure 3.7a) exhibited a quite broad lateral size distribution, centered ~ 280 nm (Figure 3.7e and Table 3.1, where the average size is reported together with the half width at half-maximum, HWHM, of the size distribution, as obtained via Gaussian fit of the size distribution histogram) and a narrow PL spectrum centered at 452 nm. This emission wavelength, compared with that of 8.5 nm cube-shaped NCs (emitting at approximately 510 nm), indicates that the thickness of our NSs should be below the Bohr exciton diameter for $CsPbBr_3$, i.e., below 7 nm.

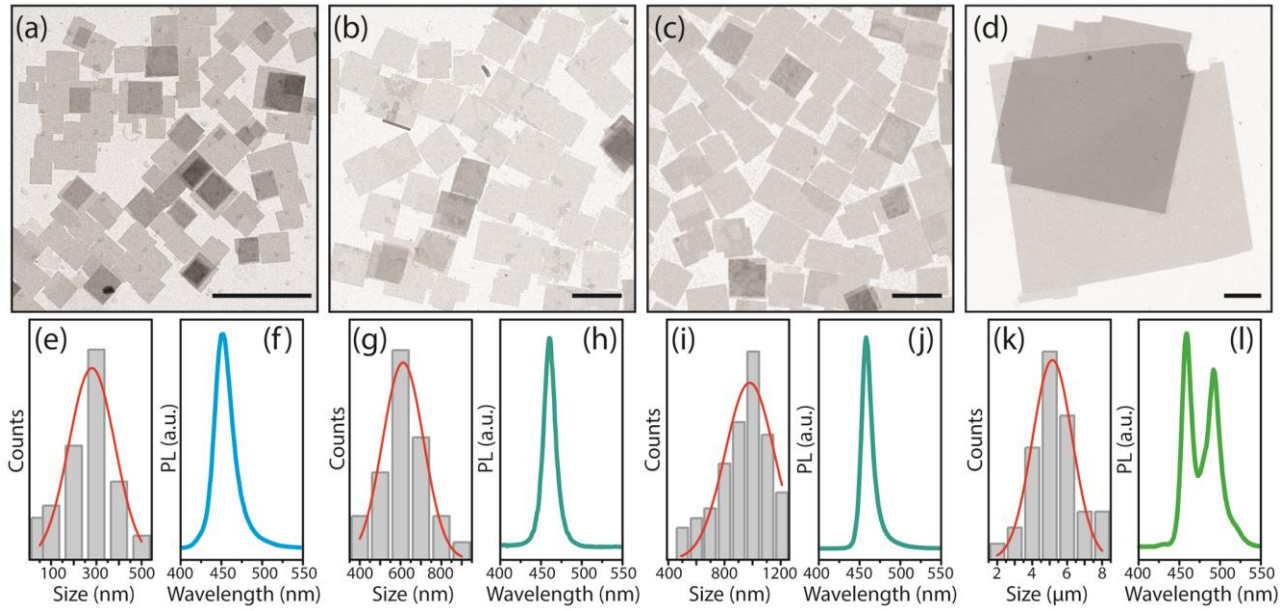

Figure 3.7: Effect of increasing the ratio of short to long ligands on controlling the lateral size of $CsPbBr_3$ NSs. Representative (a–d) TEM images, (e,g,i,k) lateral size distribution, and (f,h,j,l) emission spectra of $CsPbBr_3$ NSs prepared with short-to-long ligands molar ratios equal to X = 0.33 (a,e,f), X = 0.40 (b,g,h), X = 0.52 (c,i,j), and X = 0.67 (d,k,l). Scale bars in all TEM images are 1 μm long.

A thickness of 2.7 nm could be estimated using the Sun formula[81]. This value seems quite reliable since in the previous work from our group we had observed a similar emission wavelength for quantum confined $CsPbBr_3$ NPLs having thicknesses of 2.5 nm[117]. The presence of a single emission peak suggests that, in spite of the relatively broad lateral size distribution, our NSs had a narrow thickness distribution. By increasing the X ratio up to 0.4 and 0.52, the average lateral size of the NSs increased to 610 nm (Figure 3.7b, 3.7g) and to 975 nm (Figure 3.7c, 3.7i), respectively. In both cases, the lateral size distribution was still quite broad (Table 3.1); however, the PL spectrum was narrow and centered at 458 nm (Figure 3.7h,j), matching the PL emission wavelength of 3 nm thick $CsPbBr_3$ NPLs. In particular, the sample prepared at X = 0.52 exhibited a narrow emission peak, with full width at half-maximum of 13 nm, indicating a unimodal distribution of thicknesses (Figure 3.7j). Further increasing of the amount of short ligands in the solution (X = 0.67) led to large nanosheets, with mean lateral size of 5.16 μm (Figure 3.7d,k, Table 3.1), but with poor control over the thickness, as seen by the multiple peaks in the emission spectrum (with two distinct maxima at 458 and 491 nm, Figure 3.7l), indicating a roughly bimodal thickness distribution.

Our analysis focused then on the synthesis that delivered the sample characterized by the narrower thickness distribution coupled with a mean lateral size around 1 μm, i.e., the one prepared at X = 0.52 (Figure 3.7c,i,j). For this sample, we measured a PL quantum yield (QY) of ~33%, which is higher than that of bulk $CsPbBr_3$[119]. The increased PLQY could be related to a quantum confinement effect,

although it might simply be due to a lower density of trap states in the NSs compared to the bulk case. We also recorded the PL lifetime at the PL peak value (λ_{PL} = 456 nm, see Figure 3.8). Similar to the $CsPbBr_3$ nanoplatelets reported by Sun et al.[81], a three-exponential function was necessary to fit the PL decay.

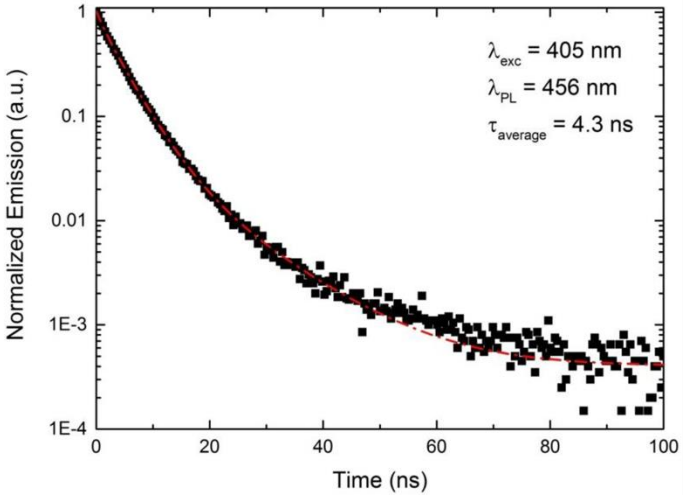

	Value	Std. error
I_1	0.10	0.01
τ_1 (ns)	1.16	0.1
I_2	0.835	0.008
τ_2 (ns)	4.12	0.08
I_3	0.065	0.012
τ_3 (ns)	11.6	0.8

Figure 3.8: PL decay measured at the PL peak (λ_{PL}= 456 nm) for a diluted toluene solution of $CsPbBr_3$ nanosheets. The PL decay fitting was carried out with a three-exponential function: $\boldsymbol{I=I_1e^{(-t/\tau 1)}+I_2e^{(-t/\tau 2)}+I_3e^{(-t/\tau 3)}}$. The results of the fitting procedure are summarized in the table of figure 3.8. Importantly the 4.12 ns component (τ 2, see table) accounts for more than 80% of the PL decay, while an initial fast decay (τ 1 = 1.16 ns) represents only the 10% of the total decay. The time-resolved PL measurement was carried out using a time-correlated single photon counting unit and a pulsed laser diode as excitation source (λ = 405 nm, pulse width = 50 ps).

The estimated average PL lifetime (τ) was of 4.3 ns, in line with previously published values for $CsPbBr_3$ NPLs[117] (τ = 3 ns) or for $(C_4H_9NH_3)_2PbBr_4$ NSs[115] (τ = 1.61 ns) synthesized with different methods. The overall PL lifetime falls within the range of perovskite NCs with shapes differing from sheets or platelets, for example, the cubic $CsPbX_3$ (where X = Br or I, τ = 1- 22 ns) NCs that were employed as gain material in lasers[102].

Figure 3.9a reports a confocal microscopy image of the NSs, recorded by exciting the sample with a pulsed laser (LDH-D-C- 405, PicoQuant GmbH, Berlin, Germany) at 405 nm and with a 40 MHz repetition rate. The emission from the NSs was collected over two channels, one in the 425 - 475 nm spectral window, which corresponds to the spectral emission range of the sample in solution (coded in blue), and the other channel in the 500 - 550 nm spectral window, centered at around the emission wavelength of bulk $CsPbBr_3$ (coded in green). Apart from a few byproducts emitting in the green channel, all the NSs were emitting in the blue channel, which corroborates the narrow thickness distribution of the sheets. Atomic force microscopy (AFM) was used to evaluate the thickness of these NSs. Few microliters of the NSs dispersion in hexane were deposited onto a glass substrate. To remove

the excess of organic ligands that could affect the correct estimation of thickness, the dried sample was washed twice with pure hexane. A representative AFM topography image is reported in Figure 3.9b. The different colors in the image correspond to different heights. From the height profiles (Figure 3.9c) we estimated a 3 nm thickness for a single NS, in agreement with the assessment based on the PL emission wavelength.

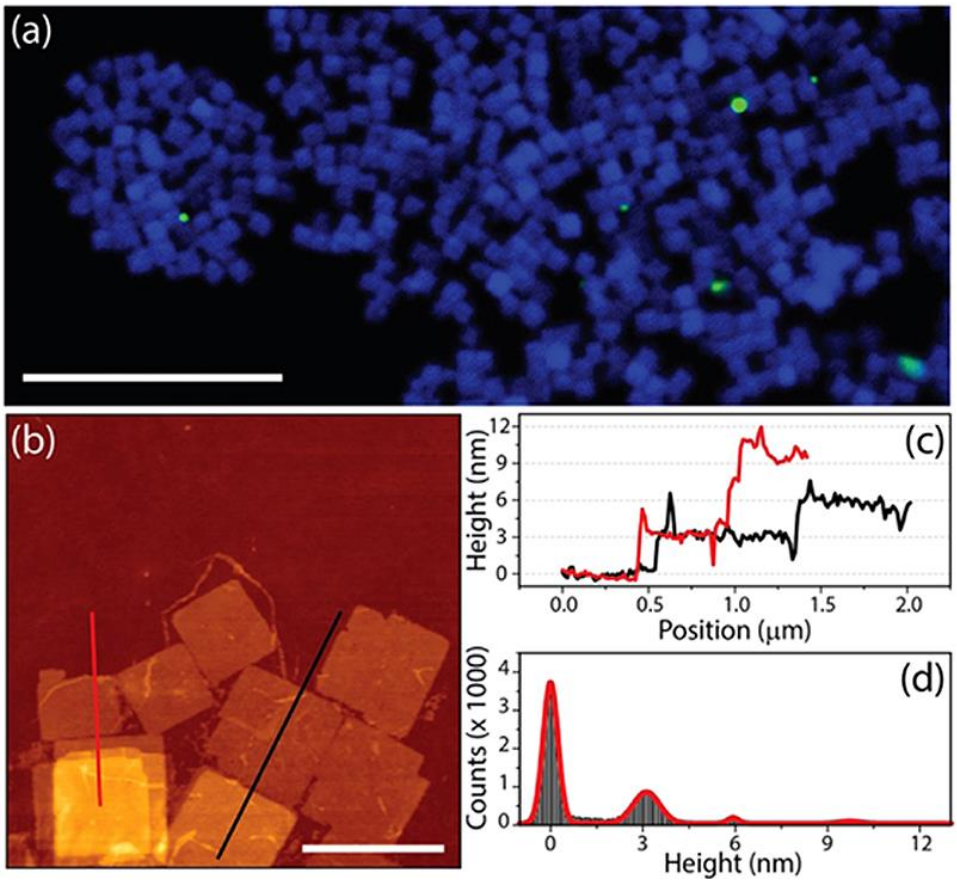

Figure 3.9: Confocal (a) and atomic force (b–d) microscopy analysis of the NSs. Scale bars correspond to 10 μm (panel a) and 1 μm (panel b). Panel c reports the height profiles obtained from the image in (b) along the red and black lines. (d) Height distribution over the whole image. The peak centered at 0 nm corresponds to the bare glass substrate.

In the height distribution over the whole AFM image (Figure 3.9d), apart from the peak centered at 0 nm, corresponding to the bare glass substrate, the main peak was centered at 3.1 nm, indicating a relatively monodisperse population of sheets with such thickness value. The other two minor peaks are present at approximately 6 and 10 nm, likely due to stacks of two and three NSs, respectively. It is also important to notice that the washing procedure in hexane likely removed not only the organics in excess but also most of the ligands from the surface of the NSs. Indeed, the high resolution adhesion maps as well as the maps of stiffness acquired by AFM, reported in Figure 3.10, indicate the presence of few small and isolated protruding features, characterized by different adhesion properties and lower stiffness

with respect to the rest of the crystal plates, likely due to the presence of a few residual organic molecules.

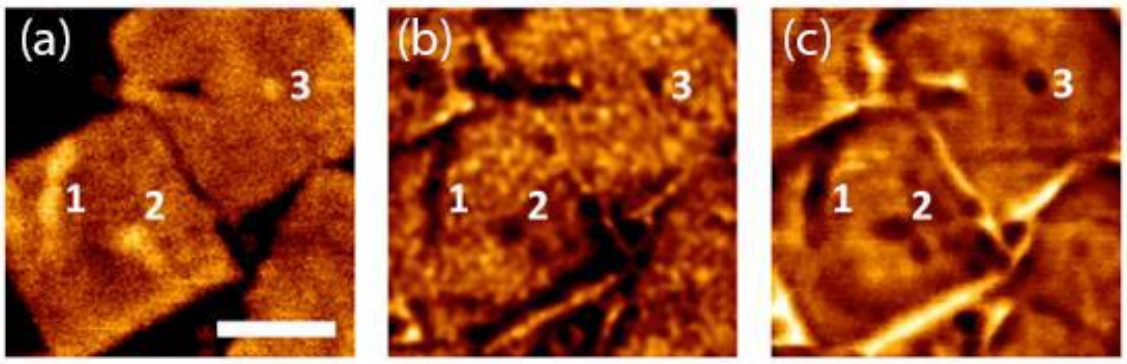

Figure 3.10: Few protruding features (indicated with 1, 2, 3) are displayed on the flat NSs surface in AFM topographical image acquired in QI mode (a). The adhesion between the AFM tip and the sample is significantly reduced on these spots, appearing as darker areas in the high-resolution adhesion map (b). At the same time, the same areas are also characterized by smaller Young's moduli (c). These observations suggest that the protruding regions are the residue of the organic molecules, originally capping the nanosheets. Scale bar: 300 nm. Data scale: 2 nm (a), 1.5 nN (b), 800 MPa (c).

High resolution TEM (HRTEM) and selected area electron diffraction (SAED) analyses revealed a structure matching with an orthorhombic crystal phase (ICSD 97851, a = 8.207 Å, b = 8.255 Å, c = 11.759 Å) also reported by Zhang et al. for $CsPbBr_3$ nanowires[116] and by Abhishek Swarnkar et al.[120] and Cottingham et al.[121] for $CsPbBr_3$ nanocuboids. The NSs are oriented with the zone axis [00−1] and enclosed by (110), (−1−10), (1−10), and (−110) facets (see Figure 3.11a). Figure 3.11a reports the HRTEM image of the thin area of the NS shown in the inset of the same panel, with corresponding fast Fourier transform (FFT) in Figure 3.11b. Data points for [210] planes (3.7 Å) are shown, which are unique for the orthorhombic phase and are missing in the cubic (ICSD 29073) and tetragonal (ICSD 109295) phases. However, some features are observed in FFTs and SAED patterns for the NSs ((100), (010), (110), (−110), (2−10) spots), which should be forbidden in kinematical diffraction conditions for orthorhombic $CsPbBr_3$, which will need further investigation. A wider view of the same nanosheet shows the presence of few nanometer-sized Pb nanoparticles, already reported for $CsPbBr_3$ nanoplatelets[117]. Figure 3.11c shows the azimuthally integrated electron diffraction pattern obtained by selecting the thin area of Figure 3.11a, which is compared with the reference card for the said orthorhombic phase and the cubic phase formerly reported for colloidal $CsPbBr_3$ nanoplatelets (ICSD 29073)[117]. The pattern contains peaks that are unique for the orthorhombic phase (one of them is marked by an arrow).

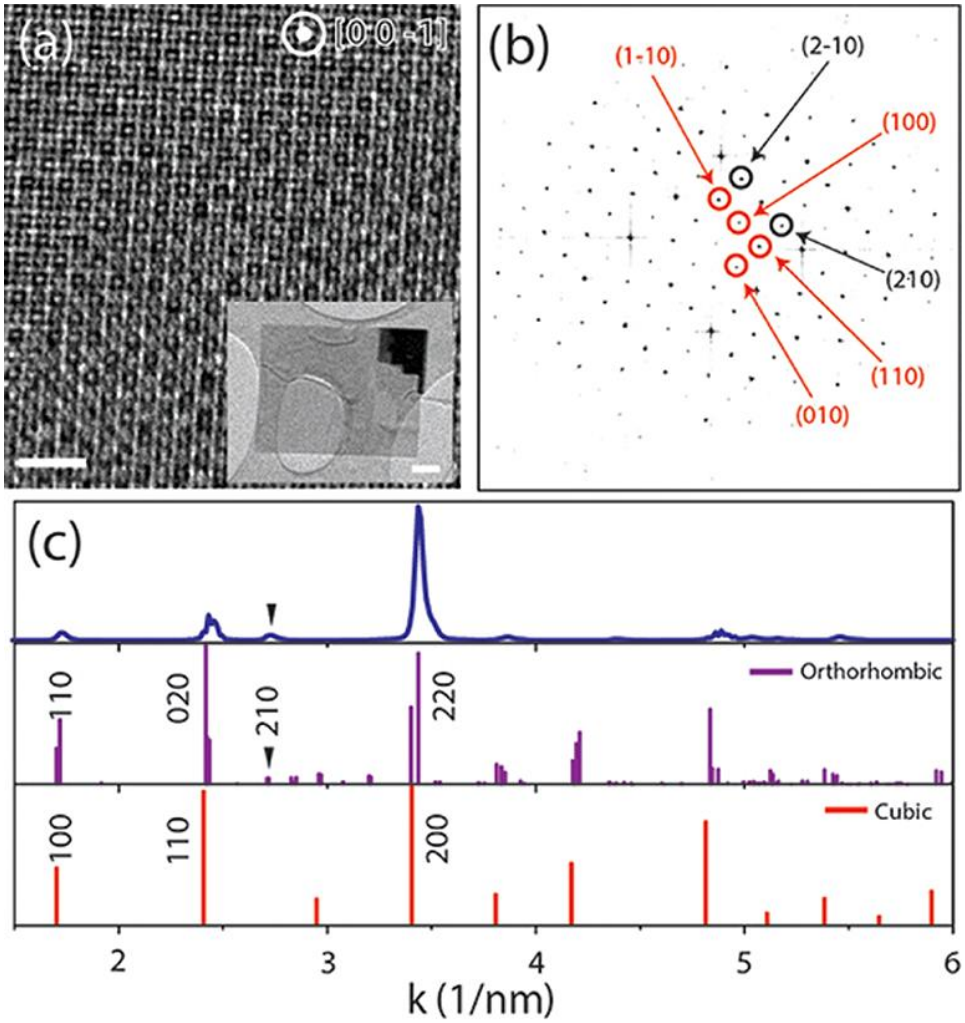

Figure 3.11: (a) HRTEM from a thin region of a CsPbBr3 sheet partly suspended on a hole in the carbon film. Scale bar: 2 nm. The inset shows the low magnification TEM image of the whole NS. The scale bar in the inset is 100 nm. (b) Corresponding FFT of (a), consistent with an orientation along the [00−1] zone-axis. (c) Azimuthal integration of the SAED pattern performed on the thin area in (a), and comparison with reference cards for the orthorhombic and the cubic CsPbBr3 phases, respectively.

Additional peaks are visible when the NSs are tilted with respect to the [001] orientation or in regions including multiple NSs (see Figures 3.12 and 3.13). NSs with various sizes share the same orthorhombic phase (see Figure 3.14).

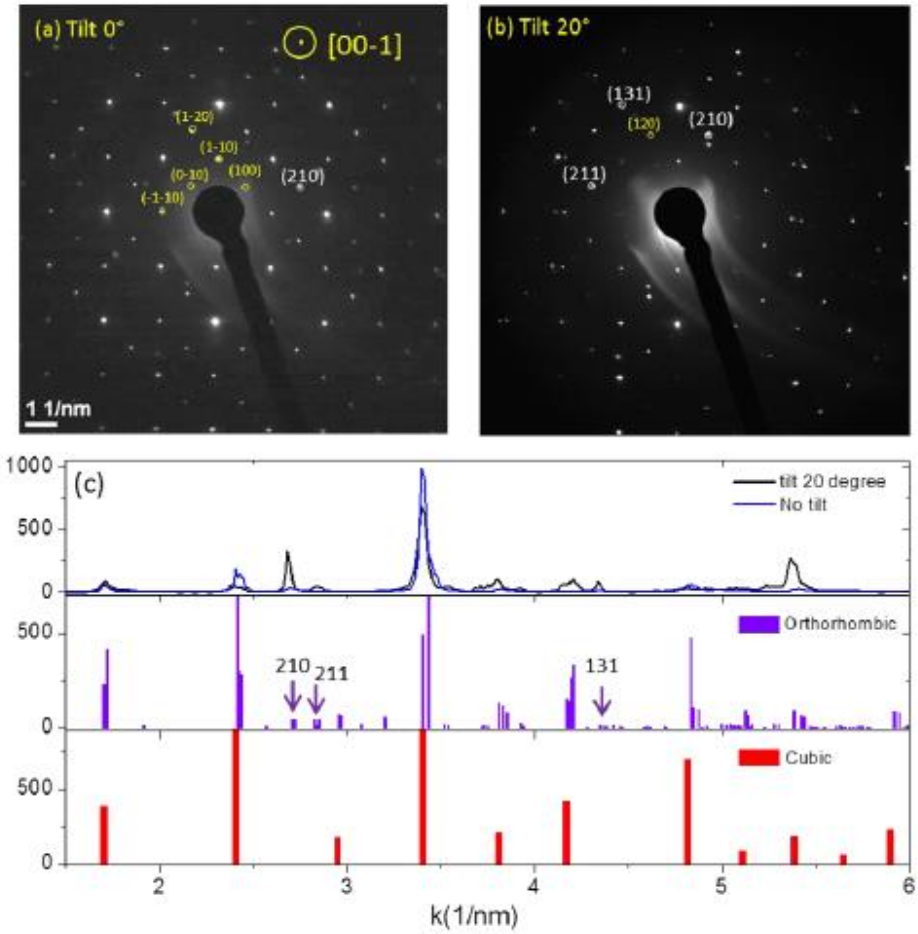

Figure 3.12: SAED patterns from the thin area of NS of figure 3.7a with (a) no tilt and (b) 20° tilt. (c) Corresponding azimuthally integrated patterns in comparison with the powder XRD data for an orthorhombic phase (ICSD 97851) and a cubic phase (ICSD 29073). The distinctive peaks for orthorhombic are labelled by arrows and marked in the diffraction patterns.

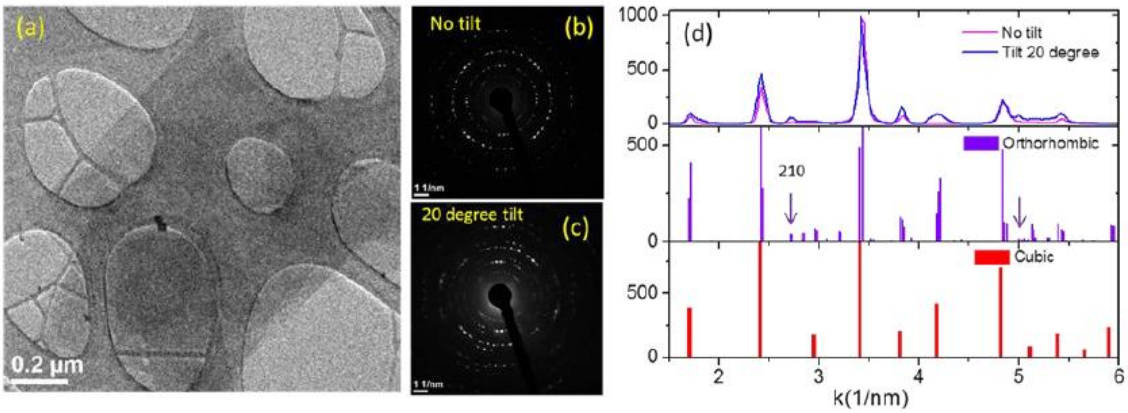

Figure 3.13: (a) TEM image of a region including multiple NSs and (b,c) SAED pattern with (b) no tilt and (c) 20° tilt. (d) Corresponding azimuthally integrated patterns in comparison with the XRD data for orthorhombic and cubic phases from database.

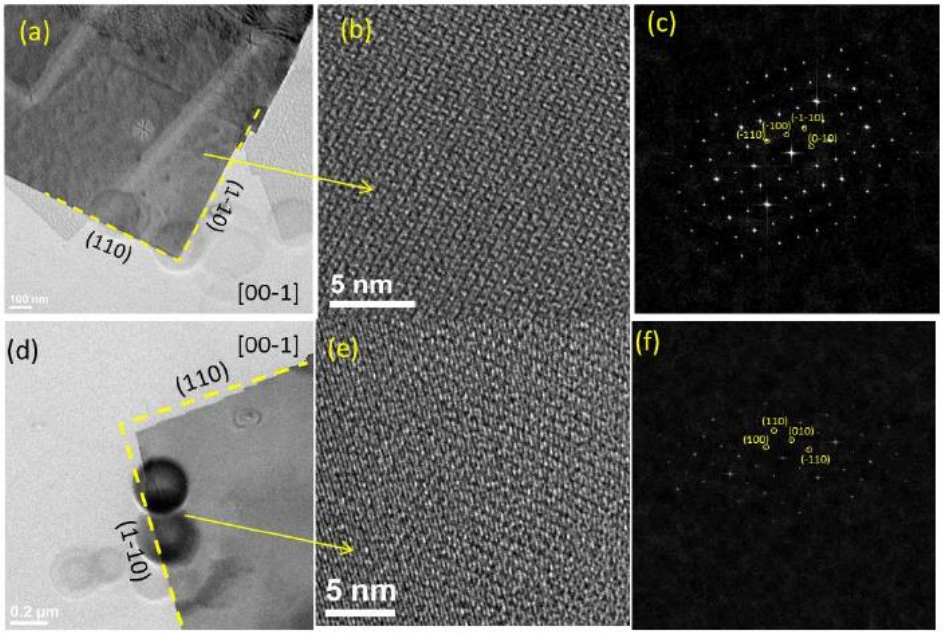

Figure 3.14: Low magnification TEM image,(b) HRTEM and (c) corresponding FFT showing orthorhombic phase; 5µm NS: (d) low magnification TEM image,(e) HRTEM and (f) corresponding FFT showing orthorhombic phase.

In line with previous reports on anion exchange on halide perovskite nanocrystals[95, 96], these NSs too could undergo anion exchange in the presence of Cl^- and I^- anions, such that they could be converted to the corresponding chloride and iodide perovskite, with preservation of shape and quantum confinement in the vertical direction (Figure 3.15).

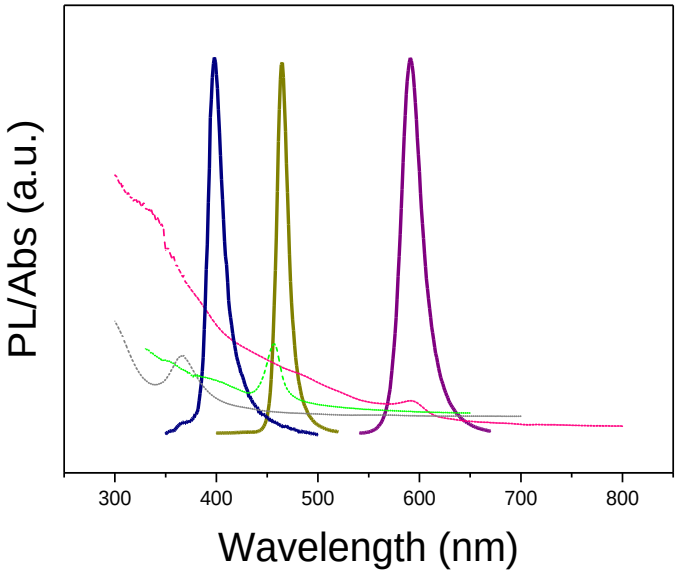

Figure 3.15: Results of anion exchange reactions on the NSs: (A) PL and absorption spectra of the initial $CsPbBr_3$ NSs, and of the corresponding samples after exchange with Cl^- and I^-. These exchange reactions were carried out in air as described in our previous work: briefly, 50µL of crude $CsPbBr_3$ NSs solution was dispersed in 3 mL of toluene and different amount of oleyl ammonium iodide or tetrabutyl ammonium chloride were added[95].

we have further studied the effects of high energy (80/200 keV) electron irradiation on colloidal $CsPbBr_3$ NSs, a morphology that facilitated the analysis of the various ongoing processes. Our results show that the $CsPbBr_3$ NSs undergo a radiolysis process, with electron stimulated desorption of a fraction of bromine atoms and the reduction of a fraction of Pb^{2+} ions to Pb^0. Subsequently Pb^0 atoms diffuse and aggregate, giving rise to the high contrast particles, as previously reported by various groups. The diffusion is facilitated by both high temperature and electron beam irradiation. The early stage Pb nanoparticles are epitaxially bound to the parent $CsPbBr_3$ lattice, and evolve into nonepitaxially bound Pb crystals upon further irradiation, leading to local amorphization and consequent dismantling of the $CsPbBr_3$ lattice (Figure 3.16).

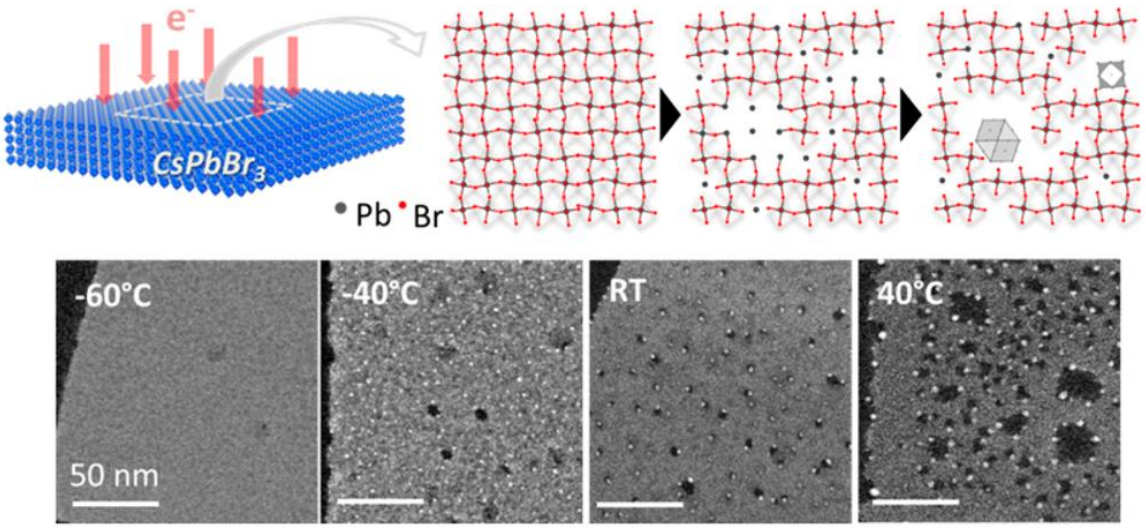

Figure 3.16: Effect of temperature on the nucleation and growth of Pb nanoparticles in 3 nm thick $CsPbBr_3$ nanosheets, as shown in HAADFSTEM images (Scale bars: 50 nm, E0 = 200 keV, the total doses for acquiring all the images are approximately $\sim 1.0 \times 10^3$ e^-/Å2)

3.4. Conclusion

In summary, we have reported the colloidal synthesis of single crystal NPLs and NSs with lateral dimensions tunable up to the micron regime (this is achieved by dosing the ratio of short to long ligands in the synthesis protocol), yet with vertical size in the quantum confinement regime. The large lateral size of these sheets should make the investigation of their physical properties more affordable and should facilitate their integration in field effect transistors and photodetectors. Additionally, and unlike previous works in which large perovskite sheets were essentially not confined in the vertical direction, the influence of quantum confinement effect of the present sheets can be finally tested in devices.

4. Bright-Emitting Perovskite Films by Large-Scale Synthesis and Photoinduced Solid-State Transformation of $CsPbBr_3$ Nanoplatelets

Abstract: Lead halide perovskite nanocrystals are an emerging class of materials that have gained wide interest due to their facile color tuning and high photoluminescence quantum yield. However, the lack of techniques to translate the high performance of nanocrystals into solid films restricts the successful exploitation of such materials in optoelectronics applications. Here, we report a heat-up and large-scale synthesis of quantum-confined, blue-emitting $CsPbBr_3$ nanoplatelets (NPLs) that self-assemble into stacked lamellar structures. Spin-coated films fabricated from these NPLs show a stable blue emission with a photoluminescence quantum yield (PLQY) of 25%. The morphology and the optoelectronic properties of such films can be dramatically modified by UV-light irradiation under ambient conditions at a high power, which transforms the self-assembled stacks of NPLs into much larger structures, such as square-shaped disks and nanobelts. The emission from the transformed thin films falls within the green spectral region with a record PLQY of 65%, and they manifest an amplified spontaneous emission with a sharp line width of 4 nm at full-width at half-maximum under femtosecond-pulsed excitation. The transformed films show stable photocurrents with a responsivity of up to 15 mA/W and response times of tens of milliseconds and are robust under treatment with different solvents. We exploit their insolubility in ethanol to fabricate green-emitting, all-solution-processed light-emitting diodes with an external quantum efficiency of 1.1% and a luminance of 590 Cd/m^2.

Parts of this chapter have been adapted or reproduced with permission from:

Shamsi, J.; Rastogi, P.; Caligiuri, V.; Abdelhady, A. L.; Spirito, D.; Manna, L.; Krahne, R., Bright-Emitting Perovskite Films by Large-Scale Synthesis and Photoinduced Solid-State Transformation of CsPbBr3 Nanoplatelets. ACS nano 2017, 11, 10206-10213.

4.1. Introduction

In Chapter 3 we found that the optical properties of $CsPbX_3$ NCs are dependent on their size and shape as has been also demonstrated by other groups for different shapes[122-129]. Among these shapes, nanoplatelets (NPLs) are of particular interest due to their excitonic behavior that is reminiscent of that of epitaxial quantum wells, which are typical building blocks in practical optoelectronic devices. The "reprecipitation" and "hot injection" methods are the most common approaches to synthesize $CsPbBr_3$ NPLs with a controlled thickness and lateral size[117, 118]. However, these methods do not yield NPLs in quantities sufficient for their implementation in optoelectronic devices. A large-scale synthesis of high-quality nanomaterials with little batch-to-batch variation could be achieved using a "heat-up" method[130]. Despite the excellent photoluminescence quantum yield (PLQY) of $CsPbBr_3$ NCs in solution, preserving a high emission efficiency in the solid state remains a challenge[131]. The PLQY of $CsPbBr_3$ NC films drops from 50% to 90% of NC solutions to 18-30% due to the agglomeration of the NCs and the subsequent loss of surface passivation[132]. Furthermore, light−matter interaction can also have a significant impact on the structural and optical properties of perovskite materials. For example, the illumination of halide perovskite films can induce trap formation and photoinduced decomposition, as has been recently reported[133, 134]. De Quilettes et al. demonstrated that the Photoinduced photoluminescence (PL) "brightening" of $CH3NH_3PbI_3$ thin films can be attributed to one order of magnitude reduction in trap-state density[135]. Wang et al. studied the transformation of $CsPbBr_3$ NPLs to their bulk analogue by continuous wave laser irradiation[136], and very recently Huang et al. reported a large PL reduction of standard $CsPbBr_3$ NC thin films under illumination with an LED[137]. Here, we first report a heat-up and large-scale synthesis approach of quantum-confined, blue-emitting $CsPbBr_3$ NPLs with a unimodal thickness distribution, which spontaneously self-assemble into stacked lamellar structures in solution with lengths up to hundreds of nanometers. In our facile method, a certain amount of isopropanol (IPA) can trigger the nucleation of unreactive precursors at room temperature. The NPLs were grown by simply heating the solution in a microwave (MW) oven. We chose MW irradiation to raise the temperature of the reaction solution uniformly[138], which is of fundamental importance for a large-scale synthesis. This MW synthesis could be extended to chloride-based perovskite NPLs and to iodide-based nanowires. When $CsPbBr_3$ NPLs are excited with a laser or LED at wavelengths in the range of 360-440 nm with a moderate intensity (less than 10 mW/cm^2), the resulting NPLs show a bright and stable blue emission both in solution and from spin-coated or drop-casted films. However, if the NPL films are exposed to a UV/blue light at a higher power, the as prepared stacked NPL structures transform to green-emitting nanobelts (NBs) with lengths within the micrometer range. These NBs

constitute highly luminescent solids and manifest an increased PLQY with respect to the original NPL solution and films, suggesting that the trap-state-induced nonradiative decay is drastically reduced. Furthermore, the NB films exhibit large and stable photoconductivity with response times below 50 ms, which makes them interesting for photodetection and energy harvesting. The UV-exposed films are stable even if in contact with different types of solvents, a feature that facilitates the fabrication of all solution-processed devices requiring multiple layer depositions by spin- or bar-coating. We demonstrate this robustness by fabricating a solution-processed green LED with an external quantum efficiency (EQE) of 1.1%[139]. The advantage of a large-scale synthesis and the facile solid transformation of stacked blue-emitting NPLs to green-emitting NBs can open possibilities regarding the application of perovskite NC solids in photovoltaic and optoelectronic devices.

4.2. Experimental Section

Synthesis and purification of $CsPbBr_3$ NPLs:

All synthesis steps reported here were performed in air. A 4 mL $PbBr_2$ solution (0.725 g of $PbBr_2$ were dissolved in 10 mL of ODE together with 5 mL of OLA and 5 mL of OA at 100 °C) was mixed with 2 mL of ODE and 0.5 mL of an as-prepared CsOA precursor (325 mg of Cs_2CO_3 dissolved in 5 mL of OA by a heat gun). After adding 250 μL of IPA, the solution was stirred using vortex for 30s. Then the turbid greenish solution was transferred to a glass petri dish and put in the microwave oven (Panasonic NN-E201WM) at medium power (350 W) for 4 min. Next, the reaction mixture was slowly cooled to room temperature by the water bath. To collect the NPLs, 3 mL of toluene was added to the crude solution; then the mixture was centrifuged at 3000 rpm for 10 min. After centrifugation, the supernatant was discarded and the NPLs were redispersed in 3 mL of toluene/hexane.

Large-scale synthesis:

7.2 g of $PbBr_2$ was dissolved in 200 mL of ODE together with the OA and OLA (50/50) at 100 °C on a hot plate under stirring overnight. Then, the as-prepared $PbBr_2$ solution was mixed with 25 mL of an as-prepared Cs-OA precursor (1.625 g of Cs_2CO_3 dissolved in 25 mL of OA by a heat gun) and 5 mL of IPA. Afterward, the solution was transferred to a 1 L glass petri dish and put in the microwave oven at medium power (350 W) for 5 min. The purification step was similarly performed to that for the small-scale synthesis.

Low-Temperature PL Measurements:

PL spectra were acquired in a vacuum chamber equipped with a cryostat (base temperature 16 K); the excitation was provided by a laser at 405 nm wavelength via an optical fiber, illuminating an area of a few mm2. The emission was collected from the center of the illuminated area through an optical window, using a lens, a collimator, and an optical fiber connected to a Horiba i-hr320 spectrometer (grating: 300 grooves/mm) that was equipped with a CCD detector. The integration time was varied according to the intensity of the observed peak, without changing the laser power.

LED Fabrication:

LEDs were fabricated on patterned ITO glass substrates, which were cleaned in an ultrasonic bath using acetone and IPA sequentially. Prior to the PEDOT:PSS deposition, the ITO/glass substrates were functionalized with oxygen plasma treatment for 10 min at 15 W. The PEDOT:PSS (35 nm) was spin-coated on the cleaned ITO (100 nm) glass substrates at 4000 rpm and dried at 140 °C for 10 min. The hole transport layers consisting of PTPD (35 nm) and PVK (8 nm) were obtained by dissolving the polymers in chlorobenzene and m-xylene at 8 and 2 mg/mL and by spin-coating at 2000 rpm and annealing at 110 °C for 20 min and 170 °C for 30 min, respectively. NPLs (40 nm) were then spin-coated from a toluene dispersion at 2000 rpm for 1 min, and the film was exposed to UV light for 7 min at 200 mW/cm2. ZnO nanoparticles as electron transport layer were spin-cast at 3000 rpm from ethanol solution, which resulted in a layer with 50 nm thickness. Finally, a 100 nm thick layer of Al was deposited by thermal evaporation in a vacuum deposition chamber. All layers were deposited in a glovebox, and only the UV exposure was carried out under air. The current−voltage− luminance characteristics were measured using a Keithley 2410 sourcemeter and a calibrated PDA100A Si switchable gain detector. The EL spectra of the devices were obtained using an Ocean Optics HR4000+ spectrometer.

4.3. Results & Discussion

The synthesis of the $CsPbBr_3$ NPLs was performed in air starting with a mixture of cesium oleate (Cs OA) and a $PbBr_2$ solution. Adding a small amount of IPA to this turbid white mixture triggered the nucleation at room temperature. The emerging excitonic absorption band at 405 nm and PL peak at 420 nm with a full width at half-maximum (fwhm) of 19 nm proved the formation of $CsPbBr_3$ clusters (Figure 4.1). When observed under TEM, these clusters quickly transformed to metallic lead dots, due to electron-beam-induced damage (Figure 4.2a). NPLs with average lateral dimensions of 30 ± 3 nm

(length) × 5 ± 2 nm (width), as shown in Figure 4.2b, were grown by applying MW radiation to the solution of $CsPbBr_3$ clusters. In a typical sample, the PL peak position at 458 nm (fwhm of 23 nm, Figure 4.1c) indicates a thickness of 3 nm according to previously reported data[140], which corresponds to 5 unit cells of perovskite layers. This synthesis method can be easily scaled up to yield several grams of NPL products as demonstrated in Figure 4.4. A conventional X-ray diffraction (XRD) pattern collected from the $CsPbBr_3$ NPLs is reported in Figure 4.1b. Due to the anisotropic shape of the NPLs, only two narrow and intense peaks at $2\theta = 15^{\circ}$ and 29.7° were observed. Our recent structural studies on $CsPbBr_3$ nanosheets demonstrated an orthorhombic phase for such a 2D confined perovskite system[140]. As displayed in Figure 4.1a, the NPLs are uniform in size and shape to the extent that they spontaneously form regular lamellar structures, made of face-to-face stacked arrays of NPLs 300-350 nm in length. We ascribe this narrow distribution of shapes to our two-step synthesis procedure that enables the separation of the nucleation step (when first small $CsPbBr_3$ clusters are formed by addition of IPA) from the growth step (when MW irradiation is turned on). As a comparison, we performed the same reaction (after the addition of IPA) using a heating mantle, applying a temperature ramp that was aimed at reproducing the results of the MW synthesis (in which the temperature was raised to 120 °C in 4 min).

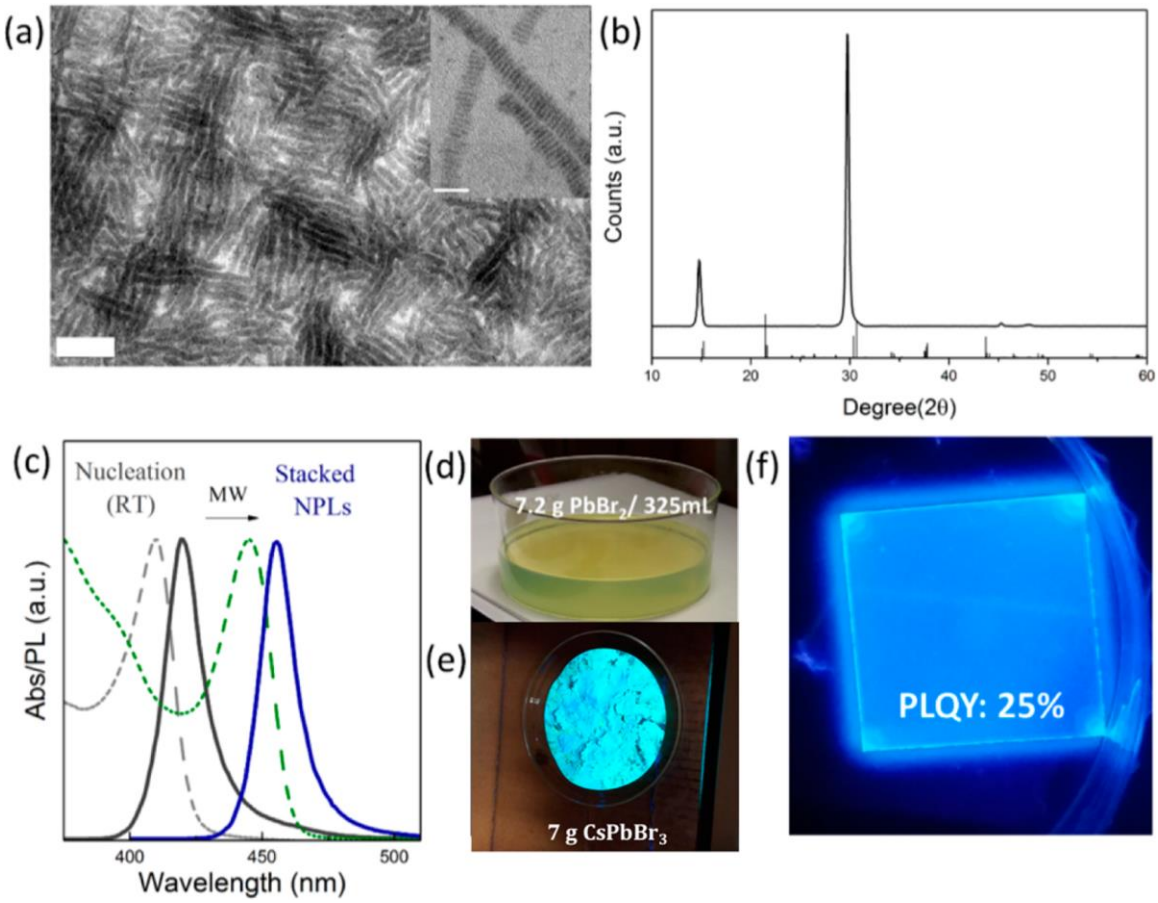

Figure 4.1: (a) Low-magnification TEM image showing ribbons of self-assembled NPLs. The inset depicts a higher magnification image in which the individual NPLs can be resolved. Scale bars correspond to 200 nm and to 50 nm in the inset. (b) XRD pattern matching with the orthorhombic reference pattern (98-009-7851). (c) Optical properties of $CsPbBr_3$ NPLs: PL (solid line) and absorption (dashed line) spectra before and after microwave irradiation. Photographs of a scaled-up (7.2 g) synthesis (d) and of the resulting 7 g of product under UV light (e). (f) Emissive NPL spin-coated thin film under UV light.

This synthesis, however, not only yielded unstacked and separated NPLs but also produced large sheets and hexagonal Cs_4PbBr_6 NCs as byproducts (Figure 4.3a).

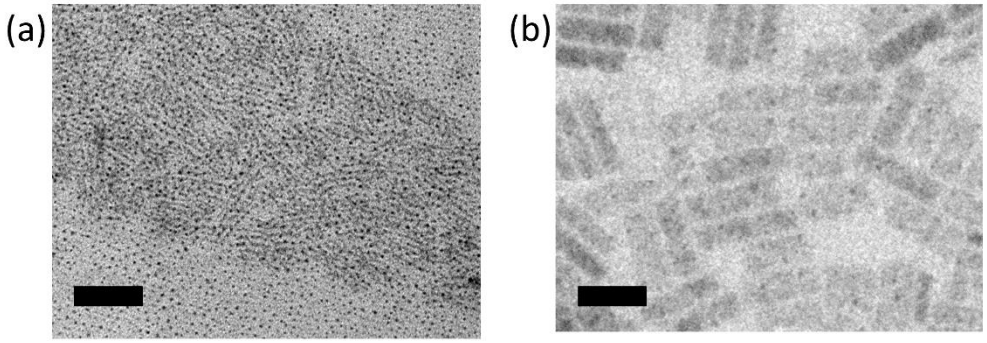

Figure 4.2: TEM images of (a) $CsPbBr_3$ clusters obtained by adding IPA to the precursor solution; (b) $CsPbBr_3$ NPLs grown by microwave (MW) irradiation from a highly diluted solution deposited on a carbon coated copper grid (scale bars correspond to 20 nm)

In another control experiment, the precursor solution was MW heated but without previously adding IPA. The product of this synthesis was a mixture of non-uniform sheets and NPLs (Figure 4.3b), which demonstrates that the separate nucleation by the addition of IPA enables a better control over growth. Henceforth, we focus our discussion on the synthesis of NPLs by MW synthesis with the addition of IPA.

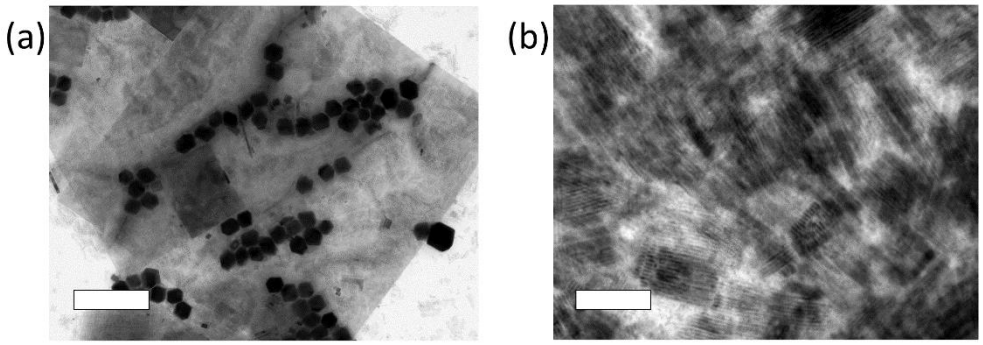

Figure 4.3: TEM images of byproducts: (a) by using a heating mantle instead of MW, and (b) by using MW but without previously adding IPA (scale bars correspond to 100 nm).

For the emission of the quantum-confined NPLs at 458 nm (blue line in Figure 4.1c), we measured a PLQY of 33% in solution and 25% for a thin film.

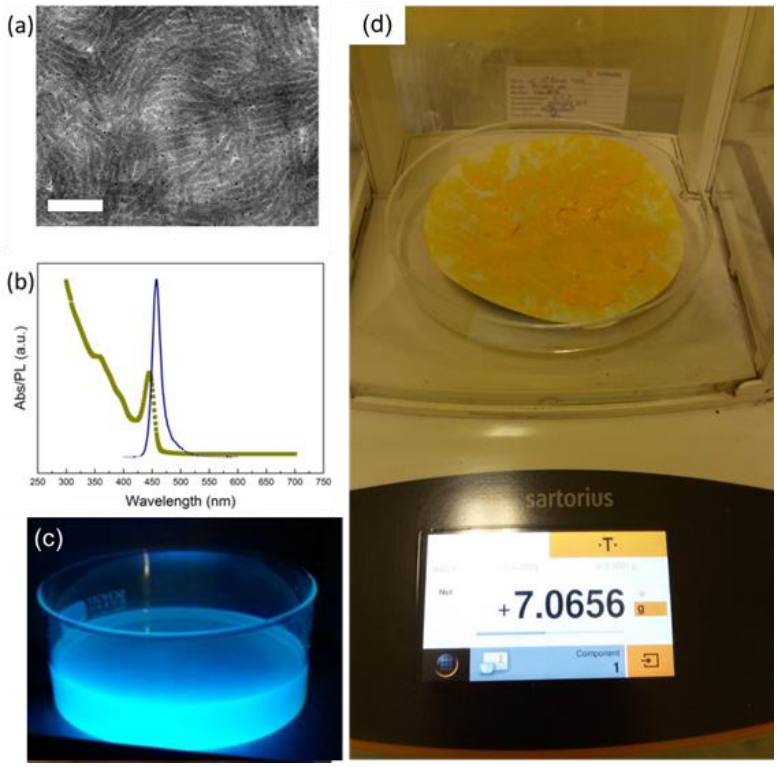

Figure 4.4: TEM image (a) and optical properties (b) of $CsPbBr_3$ NPLs prepared by large-scale MW irradiation synthesis, using 7.2 g of $PbBr_2$ in 325 ml (scale bar corresponds to 200 nm). (c,d) Photographs of NPLs solution (c) and synthesis product (d) obtained by a large scale synthesis on a precision balance showing the weight in grams.

The synthesis could be easily scaled-up to a larger batch that yielded 7 g of nanocrystals (Figure 4.1d,e), with a slightly lower PLQY in solution (29%) and an fwhm of 22 nm (Figure 4.4). Furthermore, we extended the synthesis method to the Cl- and I-based perovskite NCs. Interestingly, the chloride analogue resembles the bromide-based NPLs.

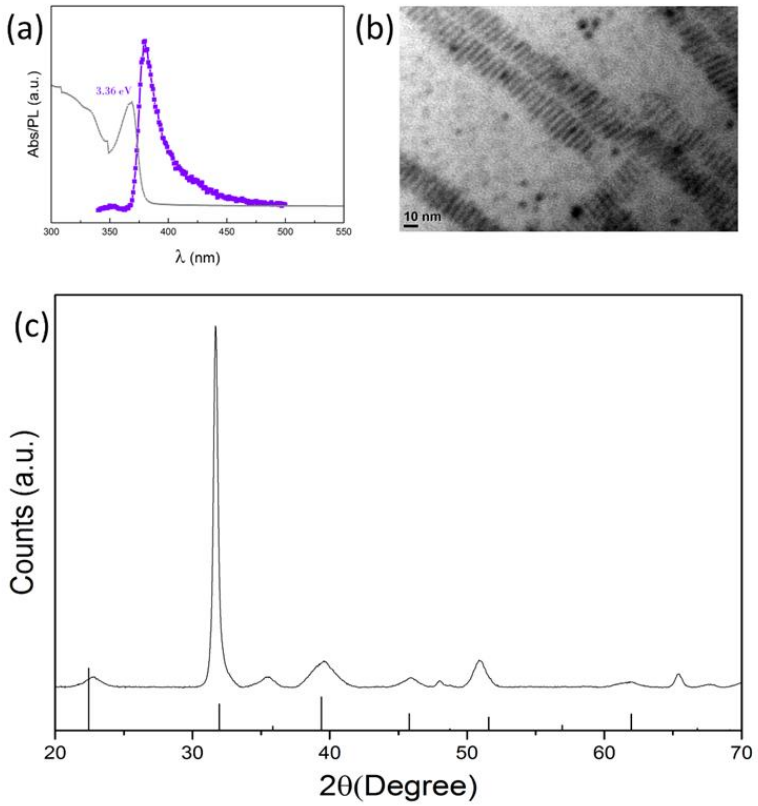

Figure 4.5: Overview of the properties of $CsPbCl_3$ NPLs prepared by MW irradiation: (a) Optical absorption and emission, (b) TEM image (scale bar corresponds to 10 nm), and (c) XRD spectrum with reference pattern ICSD 98-002-9067, cubic phase)

Further characterization of the Cl-based NPLs revealed a cubic perovskite phase and absorbance onset at 3.36 eV, which is significantly blue-shifted compared to the band gap of bulk (420 nm, 2.96 eV) $CsPbCl_3$ [141](see Figure 4.5).

In the case of $CsPbI_3$, the same reaction condition led to the formation of nanowires with multimodal thickness distribution and hundreds of nm in length (Figure 4.6) that degraded in a couple of hours if exposed to air.

We then fabricated films by spin-coating a dense $CsPbBr_3$ NPL solution (in toluene) on glass substrates and investigated their optical properties.

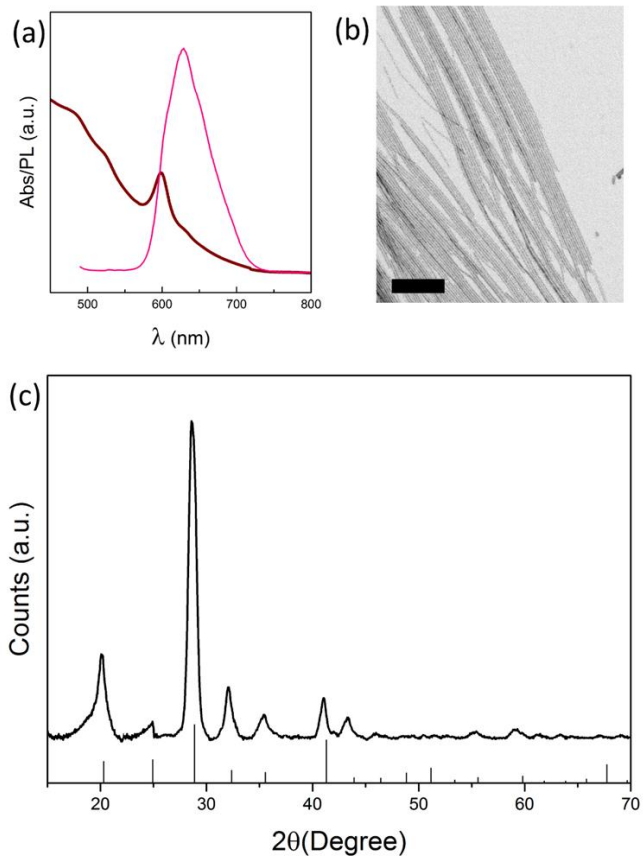

Figure 4.6: Overview of the properties of $CsPbI_3$ NWs prepared by MW irradiation: (a) Optical absorption and emission, (b) TEM image (scale bar corresponds to 200 nm), and (c) XRD spectrum with reference pattern (ICSD 98-018-1288, cubic phase).

As prepared spin-coated solutions resulted in uniform perovskite films, as observed by a scanning electron microscope (SEM) (Figure 4.7a), and exhibited strong blue emission under UV excitation (Figure 4.1f) that was stable for more than a month (Figure 4.7b).

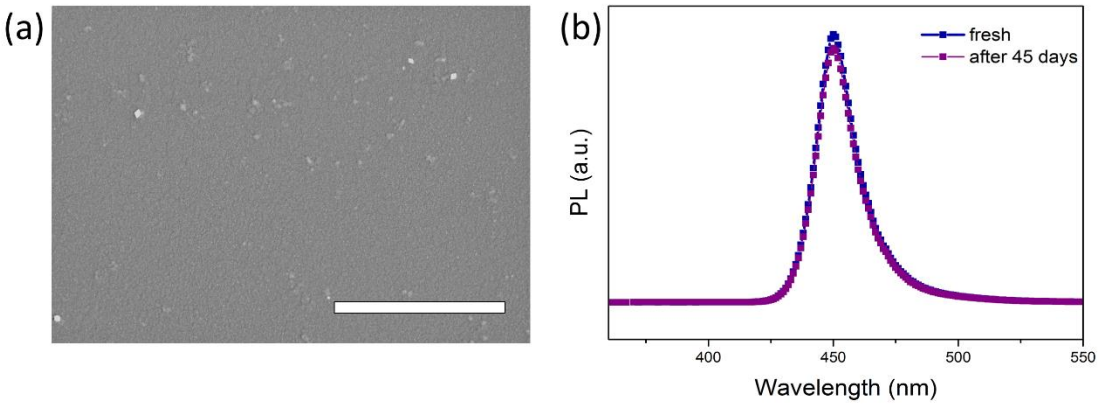

Figure 4.7: (a) SEM image of a uniform thin film prepared by spin-coating the $CsPbBr_3$ NPLs (scale bar corresponds to 3 μm); (b) PL spectra of the pristine and aged (after 45 days) NPLs thin film.

A representative PL spectrum from a NPL film is shown in Figure 4.8, manifesting a stable blue emission (peak centered at 458 nm) for more than 10 min under excitation with an LED at 385 nm at a moderate intensity of 3 mW/cm^2. A similar behavior was also observed under excitation with a laser at 400 nm.

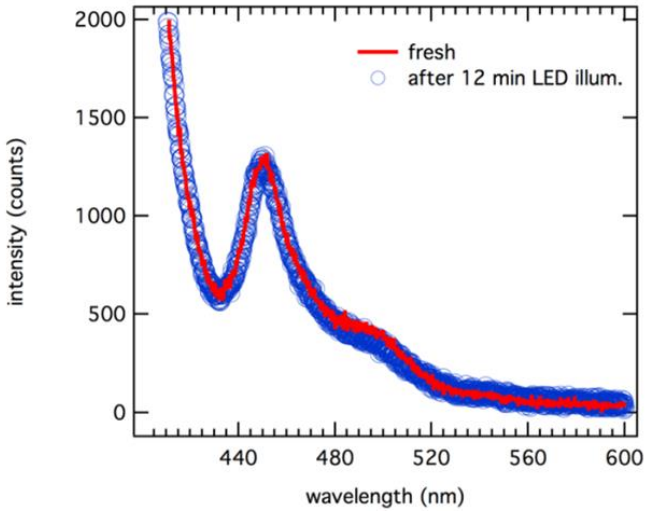

Figure 4.8: Emission spectra from a NPL thin film under excitation with an LED at 385 nm at a moderate intensity of 3 mW/cm^2 recorded immediately at LED turn on, and after 12 minutes of exposure.

However, the properties of such films can fundamentally change by exposure to UV light at a higher power. To study the morphological changes in this transformation, we deposited NPL solutions on carbon-coated TEM grids and illuminated them with an LED at 365 nm and 200 mW/cm^2 for different exposure times. The images corresponding to a 30 s, 3 min, and 5 min exposure time are shown in Figure 4.9.

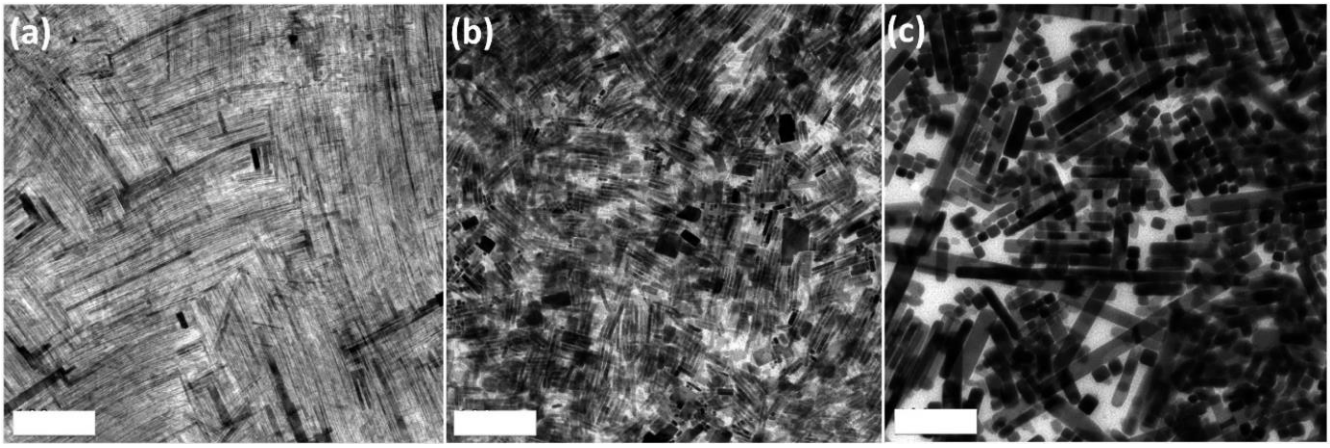

Figure 4.9: TEM images evidencing the shape evolution of $CsPbBr_3$ NPLs to NBs as a function of the LED illumination time: (a) 0.5, (b) 3, and (c) 5 min (scale bars correspond to 200 nm).

Increasing the exposure time resulted in the track-like assemblies of NPLs coalesced to larger, square and belt-shaped NCs that can be identified in Figure 4.9b,c. Focusing on Figure 4.9c, we found a

mixture of square- and rectangular-shaped NCs with widths ranging from 30 to 70 nm and lengths up to µm. A histogram on NC width and PL spectra related to this transformation are shown in Figure 4.10.

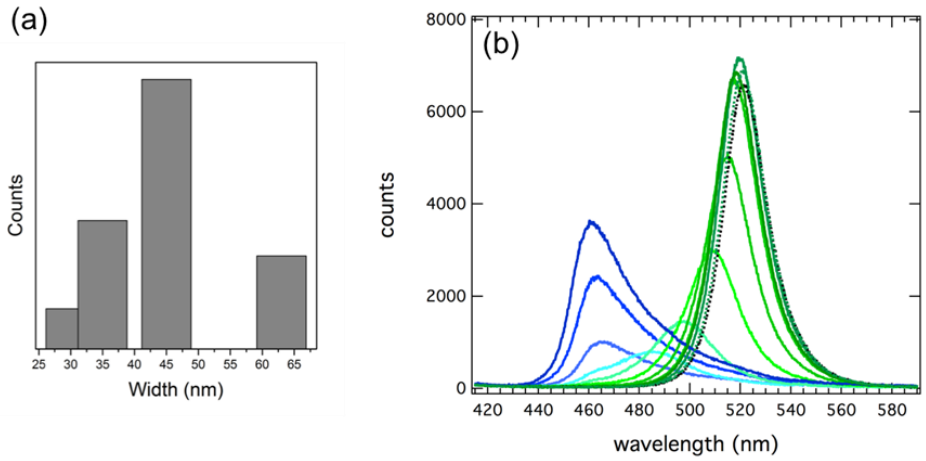

Figure 4.10: (a) A histogram on nanobelts width after transformation under UV light (LED illumination time: 5 minutes). (b) Monitoring of the change in PL during exposure with an UV LED (365 nm at 200 mW/cm^2) recorded every 30 seconds for 7 minutes.

We will refer to the rectangular structures with a large aspect ratio as "nanobelts" (NBs). The transparency of the NBs in the TEM images suggests a small thickness that most likely corresponds to the width of the original nanoplatelets. Further characterization by SEM and XRD revealed a high coverage of a thin film after transformation with an orthorhombic phase for $CsPbBr_3$ NBs (Figure 4.11).

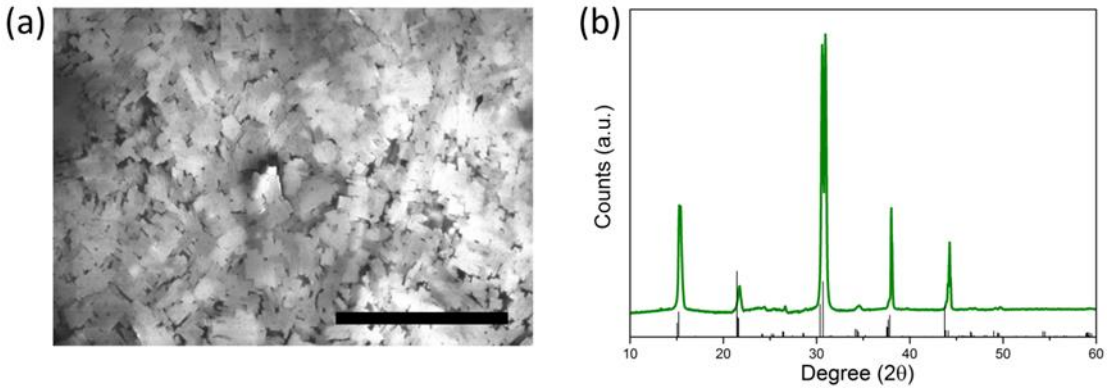

Figure 4.11: (a) SEM image (scale bar corresponds to 3 µm), and (b) XRD spectrum (reference pattern ICSD 98-009-7851) of a transformed $CsPbBr_3$ thin film by UV irradiation.

We attribute the transformation under UV light from stacked arrays of NPLs to NBs to the combined effects of lattice instability under intense light irradiation and labile surface passivation[89, 136].

The PL spectra recorded from a film on a glass substrate during 20 min of exposure to UV light at 120 mW/cm^2 under ambient conditions are reported in Figure 4.12a.b. Initially, an emission peak at 450 nm with a tail to the red is observed, similar to the emission from films under low-power excitation. With

increasing exposure time, first the blue emission is reduced, and another peak builds up at longer wavelengths that strongly increases in intensity until its center reaches approximately 520 nm, where the intensity saturates at a value much higher than the original blue emission (after around 15 min of exposure). Exposure for longer times at high illumination power can lead to a slight degradation of the green emission. The inset of Figure 4.12a shows a transformed green emitting square region surrounded by the blue-emitting film of the pristine NPLs, demonstrating that this method can be readily extended to pattern NC films by the use of shadow masks during UV exposure.

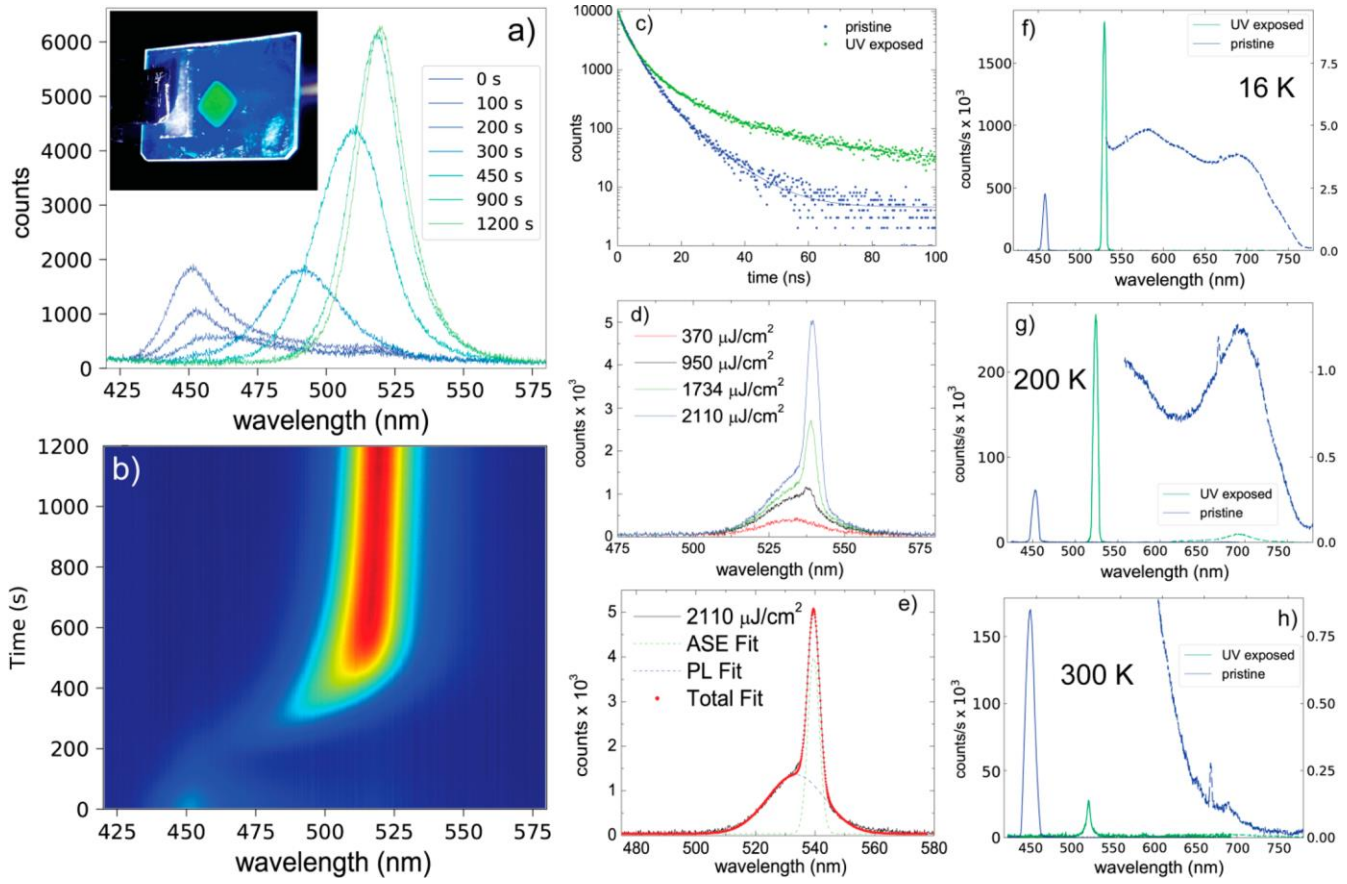

Figure 4.12: (a, b) In situ monitoring of the change in PL during exposure with a UV LED (365 nm at 120 mW/cm^2) recorded continuously for 20 min. The inset in (a) shows a photo of a spin-coated film under UV illumination, in which the central green-emitting region was transformed by UV exposure. (c) PL decay recorded at the peak maximum for the pristine and UV-exposed NPL films. (d) Emission of a film (that had been transformed by UV exposure) under excitation of femtosecond pulses with 1 kHz frequency at 400 nm for different pump flounces. Amplified spontaneous emission (ASE) occurs at a threshold of 950 μJ/cm2, manifesting a sharp ASE peak with a full width at half maximum (fwhm) of 4 nm, as evidenced by the fitting in (e). (f–h) Emission of pristine (blue) and transformed (green) films recorded under vacuum at different temperatures of 16, 200, and 300 K. The intensity of the band gap emission (sharp peaks at 450 and 520 nm) is shown on the left axes, and the defect emission intensity that occurs at longer wavelength on the right axes. Integration times were 50 ms (200 ms) for the band edge and 10 s (30 s) for the defect emission in panels (f) and (g). The weak broad signal in the defect band region in (g) is due to the background and long integration time.

Interestingly, the transformation is severely hindered under inert atmosphere. With the samples inside a glovebox, i.e., under a nitrogen atmosphere, we found that the reaction is significantly slowed down. Under these conditions, after 30 min of exposure almost no change in emission was observed, and even after 2 h of exposure the emission peak shifted only to 500 nm, manifesting a weak sideband at 520 nm (see Figure 4.13). This indicates that moisture and/or oxygen are crucial in destabilizing the NPLs under irradiation.

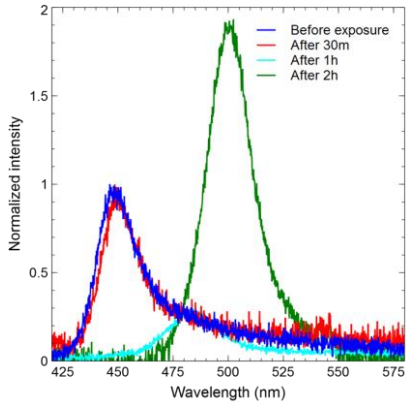

Figure 4.13: PL spectra recorded before and after 30 minutes, 1h, and 2h UV exposure of a NPL film in a glove box, i.e. under inert (N_2) atmosphere. Light power was 120 mW/cm^2.

The UV transformation occurs much faster and leads to stronger green emission, if it is performed under more humid conditions, as shown in Figure 4.14:

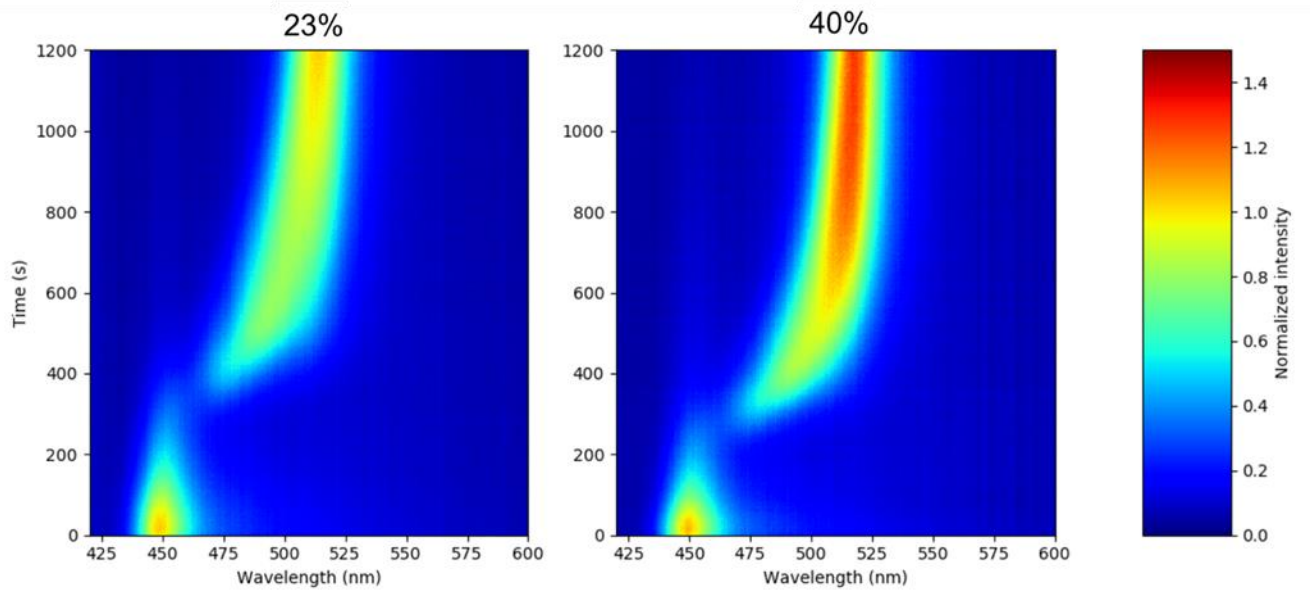

Figure 4.14: Color plots of the emission spectra recorded during UV transformation of NPL films under different humidity, but otherwise identical, conditions. Light power was 120 mW/cm^2. The spectra were normalized to the original blue PL peak of the NPL film. Clearly, the transformation occurs faster and is more efficient under higher humidity.

Defect states play an important role regarding the photoluminescence intensity of $CsPbBr_3$ crystals, and PL quenching and emission from a broad defect band around 700 nm wavelength have been reported under an inert atmosphere, which, however, can be compensated under ambient conditions due to the presence of oxygen[142]. We have measured PL spectra at different temperatures (from 16 to 320 K) under vacuum to acquire more insight into the emission dynamics of our films before and after transformation. Selected spectra are displayed in Figure 3f-h. For the pristine blue emitting films, we observe the defect band emission over the full temperature range, while for the UV-transformed films it can only be identified around 200 K. The green band gap emission of the exposed films is much stronger than the blue emission at 16 K, but it decreases strongly with increasing temperature, while the blue PL from the pristine films first decreases and then gains in intensity again at temperatures above 240 K, as shown in Figure 4.15.

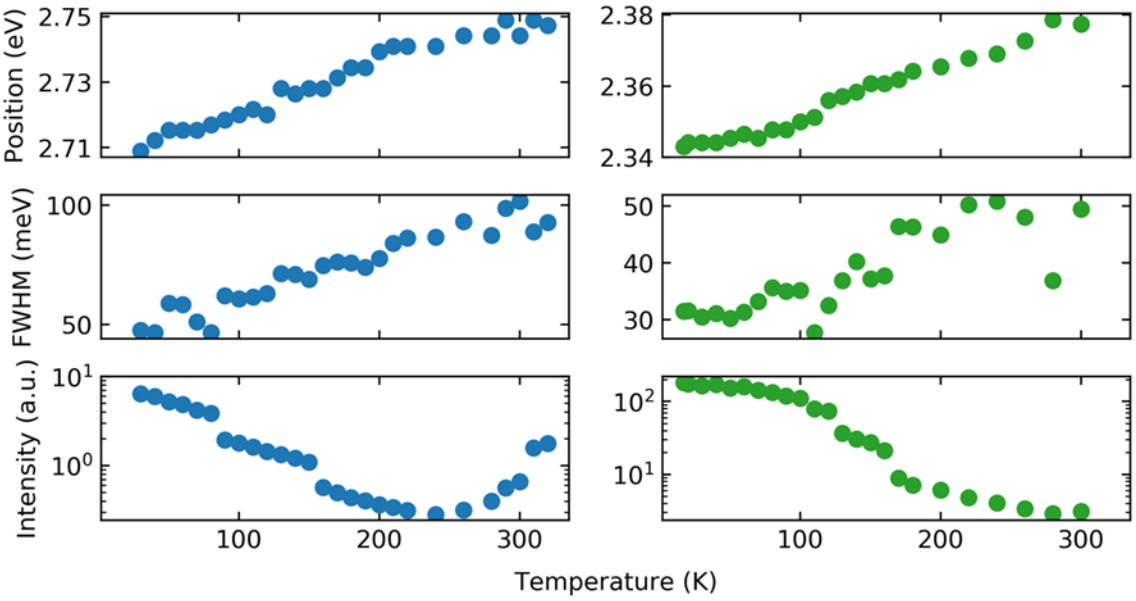

Figure 4.15: Position, FWHM and amplitude of the band edge emission versus temperature of pristine (a) and transformed (b) films measured under vacuum.

The effects occurring at temperatures above 200 K can be related to residual CO_2 that undergoes a phase change from dry ice to gas phase at 194 K, which leads to a limited supply of oxygen atoms in the atmosphere in this temperature range. These oxygen atoms can passivate defect states; therefore the band-edge emission of the pristine films is very sensitive to this effect, while that of the transformed films (with much fewer defect states) is not.

PL time decay measurements of pristine and exposed films, measured at the peak maximum (i.e., at 460 and 520 nm, respectively), are shown in Figure 4.12c. While there is little difference in the initial decay,

for longer times the transformed films manifest a slower decay that translates to an increase in the average PL lifetime from 5.18 ns to 9.51 ns after the transformation. The decay curves in Figure 4.12c were fitted with a three-exponential function:

$$A_1 \cdot e^{\left(\frac{t}{\tau_1}\right)} + A_2 \cdot e^{\left(\frac{t}{\tau_2}\right)} + A_3 \cdot e^{\left(\frac{t}{\tau_3}\right)}$$

Table 4.1: The obtained amplitudes and life times

	A_1	τ_1(ns)	A_2	τ_2(ns)	A_3	τ_3(ns)
Pristine	1904.8	1.15	7201	3.91	981	9.8
UV-Exposed	5411.3	1.56	4377	5.41	620	21.7

This increase in lifetime could be related to the suppression of a fast, nonradiative recombination caused by efficiently passivated trap states or might also originate from the reduced confinement of the transformed NCs. Furthermore, we measured PLQY with a record of 65% from the transformed films, and the UV-transformed regions exhibited amplified spontaneous emission (ASE) under femtosecond pulsed excitation with a very sharp ASE line width of 4 nm at fwhm. Such a sharp line width shows that the ASE is extremely time coherent. The stability of this sharp emission peak with respect to spot location and over time excludes random lasing as its origin. The lowest ASE threshold of 260 μJ/cm^2 was observed from specific regions of drop-cast films, while we consistently found an ASE threshold of 950 μJ/ cm^2 from spin-coated films with a thickness of around 60 nm (see Figure 4.12d,e). These ASE threshold values are considerably larger than those observed, for example, by Yakunin et al.[102], which could be related to the much smaller film thickness in our case, together with a higher roughness resulting from the change in NC morphology induced by the UV transformation.

To study the electrical properties before and after transformation, we evaporated gold pads with a spacing of 50 μm, by using a shadow mask and thermal evaporation, onto a film in which a region of approximately 5 × 5 mm^2 was transformed by UV exposure. From the nontransformed region, we were not able to measure any reproducible current, as the signal remained erratic and below our noise threshold. Therefore, we will discuss only the results obtained from the UV-exposed region. The current in the dark and under illumination with white light is shown in Figure 4.16a. We found a low, stable current-voltage (I−V) curve in the dark and a strong increase in the current under illumination, with a photocurrent to dark current ratio of 20 at 1 V. The photocurrent spectrum depicted in Figure 4.16b reflects the behavior of quasi bulk-like $CsPbBr_3$ NCs, with a dominant peak at 530 nm due to the band-edge absorption. The UV-transformed films demonstrate a very robust and relatively fast response of

the photocurrent when the light is switched on and off (Figure 4.16b,c), with rise and fall times of 20 and 46 ms, respectively. This stable (photo)current makes the transformed films appealing for photodetection and energy conversion.

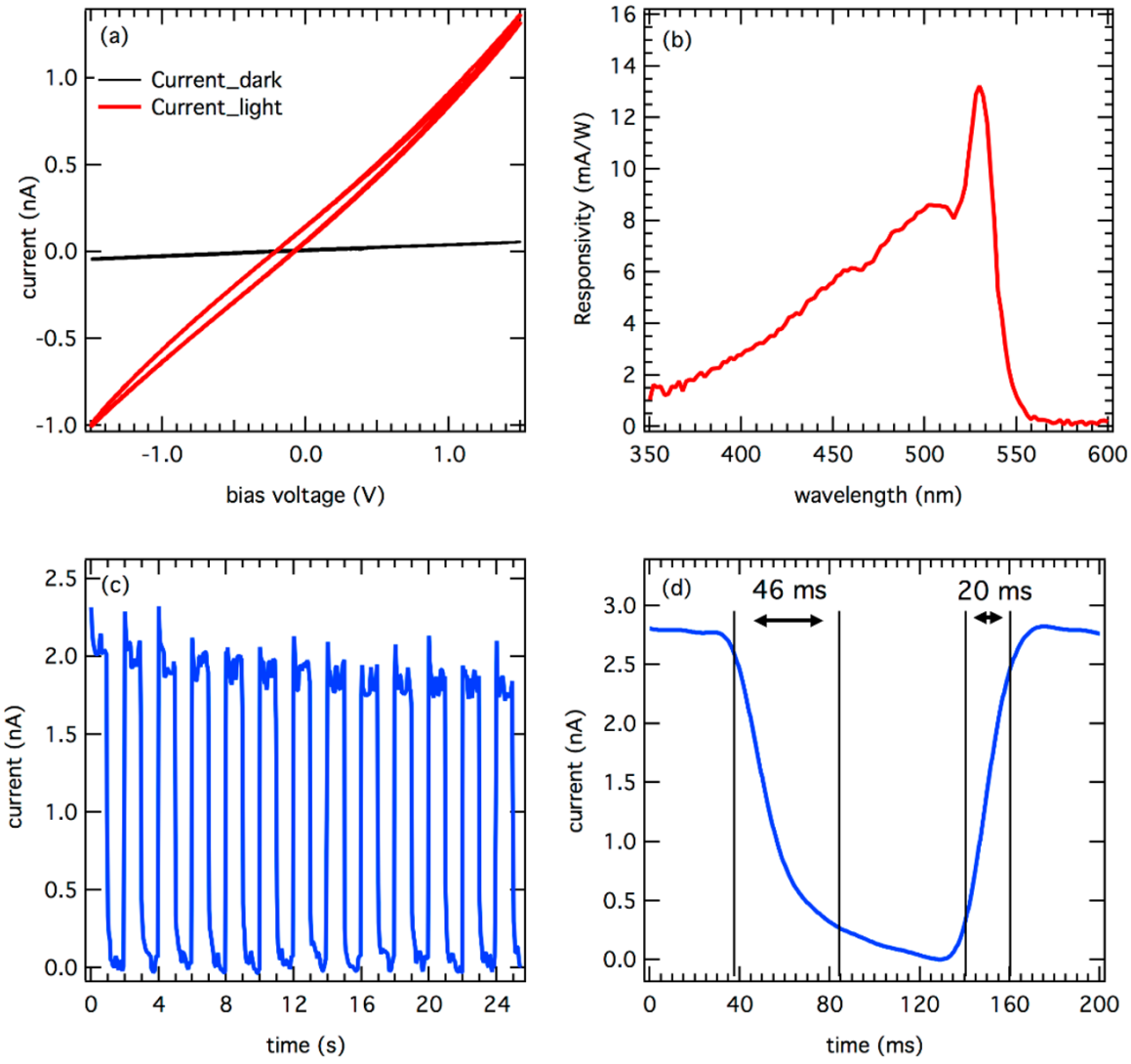

Figure 4.16: Electrical properties of UV-transformed films. (a) Current–voltage characteristics in the dark and under white light measured in air. The graph shows four consecutive scans that highlight the reproducibility of the I–Vs, with a small hysteresis in the photocurrent. (b) Photocurrent spectrum recorded under illumination with a xenon lamp coupled to a monochromator at a bias voltage of 5 V, manifesting a strong peak at 530 nm due to the band-edge absorption. (c, d) Current over time while the illumination via a white LED was switched on and off at a bias of 2 V. The rise and fall times between 90% and 10% of the maximum signal are 46 and 20 ms, respectively.

To date, most LED structures have been fabricated with an evaporated charge transport layer on top of the perovskite layer[143-148], since typically perovskite NC films are unstable in common solvents (i.e., they dissolve) and suffer from PL degradation. This severely hinders their use in all-solution processed devices, and there are few reports on all-solution processed perovskite LEDs, in which insolubility of

the perovskite film was achieved either by cross-linking of surface ligands[149] or by an amine-free synthesis[150]. The UV-transformed films described here remain stable in solvents such as methanol, ethanol, IPA, and toluene (see Figure 4.17) and maintain their excellent optical properties, unlike their pristine blue-emitting NPL film counterparts, which would dissolve once dispersed in such solvents.

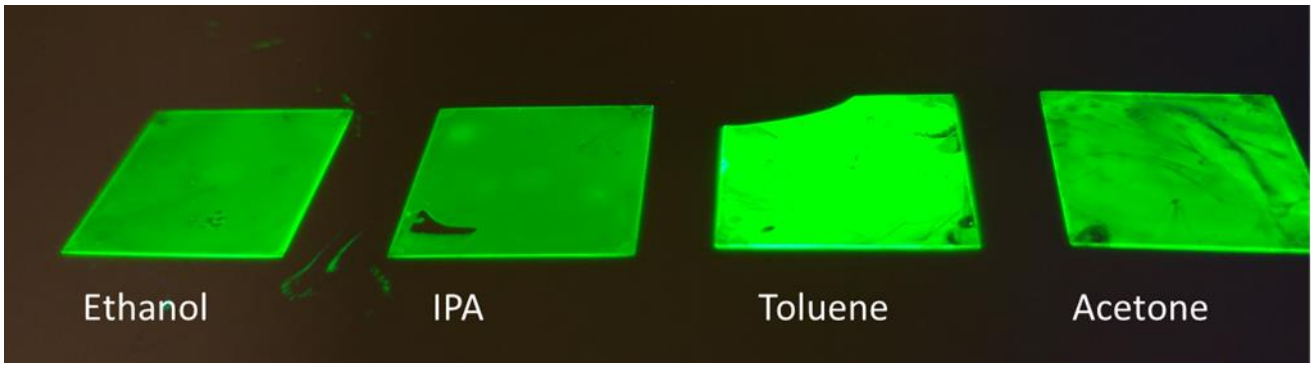

Figure 4.17: Photographs of UV-transformed thin film after treatment with different solvents under UV light.

We exploit this favorable behavior to fabricate an LED in which all layers were deposited from solutions, with the exception of the anode and cathode.

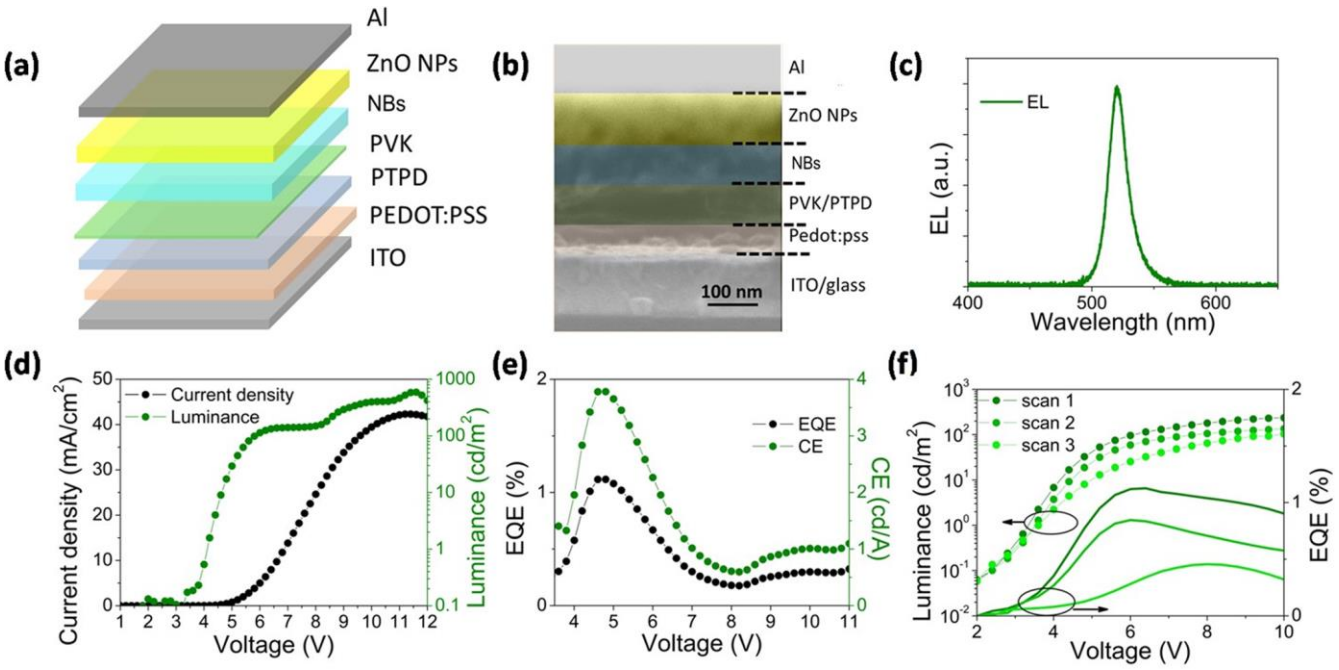

Figure 4.18: Schematic representation of the LED architecture. (b) Cross sectional SEM image showing the different layers of the LED. (c) Electroluminescence spectrum of the LED at an operating voltage of 8 V. (d) Current density and luminance versus bias voltage of a typical best device. (e) External quantum efficiency (EQE) and current efficiency (CE) as a function of voltage. (f) Luminance and EQE of the same device for several consecutive scans.

We use the architecture illustrated in Figure 5a, which consists of ITO as anode, a trilayer structure made of poly(3,4-ethylenedioxythiophene) polystyrenesulfonate (PEDOT:PSS), poly(N,N′-bis(4-butylphenyl)- N,N′-bis(phenyl)benzidine (PTPD), and poly- (vinylcarbazole) (PVK) as hole transport layers. Next, the NPL single layer was spin-coated from a toluene solution and exposed to UV light for transformation. Then, ZnO nanoparticles in ethanol were spin-coated as the electron transport layer, and finally Al was deposited by thermal evaporation as the cathode. Figure 4.18b shows a cross section SEM image of the device where the different layers can be identified. The electroluminescence reported in Figure 4.18c manifests a narrow emission peak at 520 nm with an fwhm of 17 nm. Typical turn-on voltages of our LEDs were as low as 2.2 V at 0.1 cd/m^2, with a maximum EQE of 1.1% and peak luminance of 590 cd/m^2 (Figure 4.19 shows the photograph of a perovskite NC-LED with a 40 nm thick NC layer).

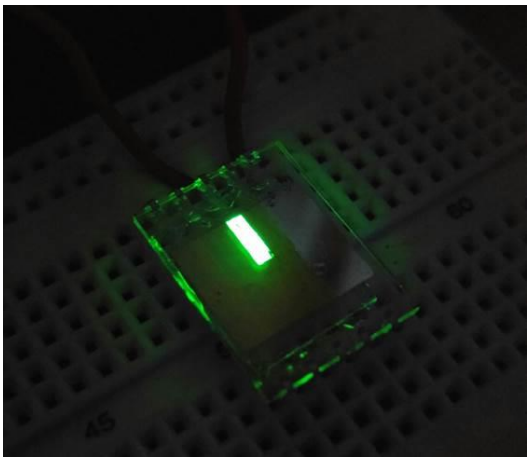

Figure 4.19: Photograph of UV-transformed NC-LED with 40-nm thick NC layer

With these characteristics, our device outperforms by a factor of 3 the green-emitting solution processed perovskite LEDs reported so far (see Table 4.2)[149, 150].

Table 4.2: Comparison of device performance by all-solution processed LED

	Reference	EL peak wavelength nm	FWHM of EL spectrum nm	Turn on voltage V	Max luminance Cd/m^2	Peak EQE %	CTL on top of perovskites film
All solution-processed CTL layers	ref[150]	510	-	2.8	934	0.32	F8 (chlorobenzene)
	ref[149]	523	-	2	2335	0.19	TFB (toluene)
	This work	520	17	2	590	1.1	ZnO NPs (ethanol)

Our devices were still functional after several consecutive bias scans up to an operating voltage of 10 V (Figure 4.18f), where we observed roughly a 50% drop in luminance from one scan to the next, accompanied by a decrease in EQE from 1.1% in the first scan to 0.8% in the second and 0.4% in the third scan. This reduction in luminance could be related to the instability of the NCs under high voltage, and indeed, subsequent luminance curves recorded in a lower bias range up to 5 V were much more reproducible (Figure 4.20)

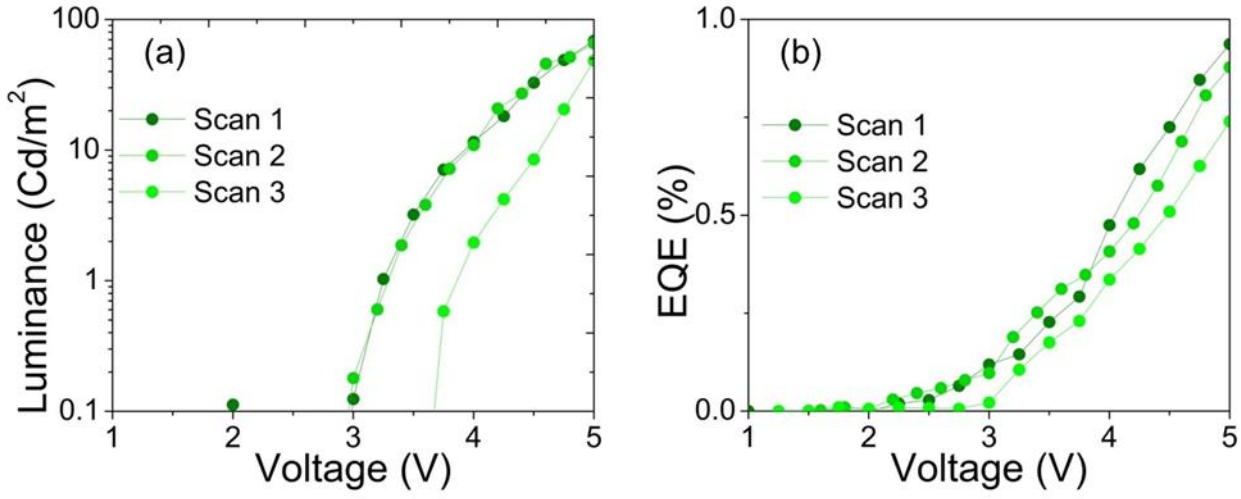

Figure 4.20: Repetitive scans measuring luminance and EQE of the LED in a low bias voltage range, up to 5V the degradation of the LED is significantly reduced if operated at lower bias.

4.4. Conclusion

In conclusion, we have reported a fast and facile method to obtain large-scale quantities of $CsPbBr_3$ NPLs by microwave synthesis that manifest stable, quantum-confined blue emission in solution and in thin films. The morphology of the NPL films could be changed by UV light exposure to obtain films of bright green-emitting NBs with a PLQY of 65% that also demonstrate robust electrical properties and high photoconductivity. This UV exposure method, which significantly improves the conductive properties, while conserving and even enhancing the optical emission, can be a very interesting alternative for the fabrication of optoelectronic devices based on perovskite nanocrystal inks. To this end, we demonstrated solution-processed green-emitting LEDs with a peak EQE of 1.1% and a luminance of 590 cd/m^2.

5. Colloidal CsX (X = Cl, Br, I) Nanocrystals and their Transformation to $CsPbX_3$ Nanocrystals by Cation Exchange

Abstract: We have developed a facile colloidal synthesis approach for nearly monodisperse CsX (X = Cl, Br, I) nanocrystals with truncated octahedral shape and simple cubic structure. Upon the partial exchange of Cs^+ with Pb^{2+} ions, these particles can be transformed to fluorescent $CsPbX_3$ (X = Cl, Br) nanocrystals, with core/shell $CsX/CsPbX_3$ (X = Cl, Br) as intermediate structures. The CsBr case has been studied extensively: In the early stages of the transformation, i.e. for CsBr NCs with thin $CsPbX_3$ shells, the particles exhibit a strong blue-shifted emission compared to the bulk band gap of $CsPbBr_3$, due to the presence of quantum confined $CsPbBr_3$ domains on the surface of the CsBr particles. These confined perovskite domains are unstable, as the emission red-shifts with time. Also, the nanocrystals undergo significant inter-particle aggregation over time if the cation exchange process is not completed. The full transformation scheme, however yields stable and monodisperse $CsPbBr_3$ NCs. This approach provides tunability of the size of the final particles, at least in the cases of $CsPbBr_3$ and $CsPbCl_3$.

Parts of this chapter have been adapted or reproduced with permission from:

Shamsi, J.; Dang, Z.; Ijaz, P.; Abdelhady, A. L.; Bertoni, G.; Moreels, I.; Manna, L., Colloidal CsX (X = Cl, Br, I) Nanocrystals and Their Transformation to CsPbX3 Nanocrystals by Cation Exchange. Chemistry of Materials 2017, 30, 79-83.

5.1. Introduction

Cesium halides (CsX, X = Cl, Br, I) are interesting materials for studying the fundamental aspects of defects and doping, and for use in scintillation detectors, as is clear from the rich literature on thin films and bulk crystals of cesium halides over the past few decades[151, 152]. In the 1960s, activated CsX crystals (with Tl, Na, and other elements) were introduced as gamma ray and charged particle detectors[153], and several studies elucidated their band structures and role of defects[154, 155]. The interest in CsX was further triggered by the discovery of specific features in the optical spectra of doped CsX salts[60]. Also, the luminescence from nanosized aggregated $CsPbX_3$ phases was initially observed in CsX single crystal hosts in 1997[78], which initiated additional investigations in the early 2000s[156, 157]. Aceves et al.[157], for example, found that Pb-doped CsBr bulk crystals have optical emission characteristics that are similar to those of Cs_4PbBr_6, $PbBr_2$ and $CsPbBr_3$ bulk crystals[157]. This indicates that Pb^{2+} ions, once inserted as substitutional dopants in the CsBr matrix, self-organize locally forming various binary and ternary Cs-Pb-Br structures.

This historical perspective above that CsX nanocrystals (NCs), and CsBr NCs in particular, are an interesting class of nanoparticles, and they can act as precursors for the synthesis of $CsPbX_3$ NCs, as we are reporting here. We were able to synthesize monodisperse colloidal CsX NCs, with truncated octahedral shapes and simple cubic structure. The size of the CsX NCs could be tuned by varying the reaction temperature, in an ambient atmosphere. CsBr NCs were then reacted with lead oleate ($Pb(OA)_2$) to form core/shell $CsBr/CsPbBr_3$ NCs and finally $CsPbBr_3$ NCs a by partial $Cs^+ \rightarrow Pb^{2+}$ cation exchange. Although the reaction was accompanied by a noticeable shrinkage in the size of the NCs, due to partial etching, there was a correlation between the initial size of the CsBr NCs and that of the $CsPbBr_3$ NCs. This means that, rather than undergoing a dissolution-recrystallization, the transformation undergoes a reorganization of the lattice following the insertion of Pb^{2+} ions and the ejection of the Cs^+ ions. This is also supported by high resolution transmission electron microscopy (HRTEM) analysis, which indicated the formation of core-shell $CsBr/CsPbBr_3$ structures as intermediates. The emission from these core/shell structures in the early stage of the exchange was strongly blue shifted from the corresponding bulk values of $CsPbBr_3$, as is to be expected from a shell thickness in the strong quantum confinement regime. This emission was, however, unstable and it red-shifted over time, even when the exchange was stopped by precipitating the particles and re-dispersing them in a clean solvent. This instability was also reflected in the aggregation of the purified particles, after overnight storage. The photoluminescence (PL) quantum yield (QY) of the fully transformed $CsPbBr_3$ NCs was stable and in the range of 32% - 50% which is, on average, lower than that of the

corresponding particles that are prepared by the standard synthesis approach (which can be in the range of 50 - 90%). This is most likely due to the presence of structural and surface defects. Surface treatments with lead thiocyanate could increase the PLQY to 60%. Similarly, starting with CsCl NCs, $CsPbCl_3$ NCs could be synthesized, again with a correlation between the size of the starting CsCl NCs and that of the $CsPbCl_3$ NCs. In the case of the CsI→ $CsPbI_3$ transformation, the control over the size of the final perovskite NCs was less accurate and resulted in polydisperse particles[158].

5.2. Experimental Section

Preparation of cesium-oleate solution:

0.325 g Cs_2CO_3 were dissolved in 5 mL OA by using heat gun until all Cs_2CO_3 reacted with OA.

Preparation of $PbBr_2$ solution:

0.072g $PbBr_2$ were solubilized in 2mL ODE, 1mL OA and 1mL OLA in a 20 mL vial on a hotplate at 100°C for 20 minutes.

Preparation of lead-oleate ($Pb(OA)_2$) solution:

0.044 g PbO were dissolved in 2 mL OA by using heat gun until all PbO reacted with OA.

Synthesis of CsX NCs:

All syntheses were carried out in air and without any pre-dried chemicals or solvents. In a typical synthesis, halide precursors (0.4 mmol) were dissolved in 2mL ODE, 1mL OA and 1mL OLA in a 20 mL vial on a hotplate at 100 °C. After complete solubilization of the halide precursors, 500 µL of CsOA was added to the solution at optimized temperature. After 5 minutes, the reaction mixture was slowly cooled to room temperature using a water bath. To collect the CsX NCs, the solution was then centrifuged at 3800 rpm for 10 min. After centrifugation, the supernatant was discarded and the NCs were redispersed in 4mL hexane or ODE (in order to carry out the transformation reactions).

Transfromation reactions:

All experiments were carried out under ambient atmosphere. In our full transformation reactions, 200 µL of as-prepared $Pb(OA)_2$ (40 µL for initial stage and 80 µL for intermediate stage) were added to the 0.5 mL of CsX NC solutions at room temperature under vigorous stirring for 30 seconds. After the washing step, the perovskite NCs were redispersed in hexane.

5.3. Results & Discussion

The CsX NCs were prepared by dissolving different types of salts as halide precursors, such as InX_3, ZnX_2, CoX_2, and tetrabutylammonium halide, in octadecene (ODE) together with oleylamine (OLA) and oleic acid (OA), then adding Cs-oleate (cesium carbonate dissolved in OA, CsOA) at different reaction temperatures, as is detailed in Table 5.1 and in the experimental section. The reaction temperature and the specific halide precursors are the key parameters for producing uniform NCs as well as for having good control of the size. All NCs had truncated octahedra shapes, unless stated otherwise. Conditions had to be adjusted for each halide composition, as is described below and is detailed in the experimental section.

CsCl. Initial tests using $CoCl_2$ led to deep blue tetragonal Cs_3CoCl_5 nanowires (Figure 5.1).

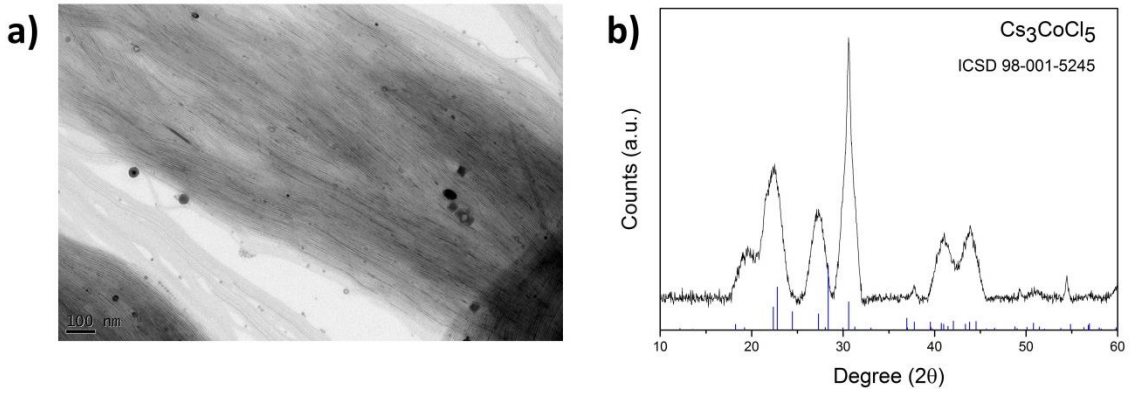

Figure 5.1: a) TEM image and b) XRD pattern of Cs_3CoCl_5 NWs

Alternatively, dissolving $ZnCl_2$ salt in the same medium yielded orthorhombic Cs_2ZnCl_4 NCs (Figure 5.2).

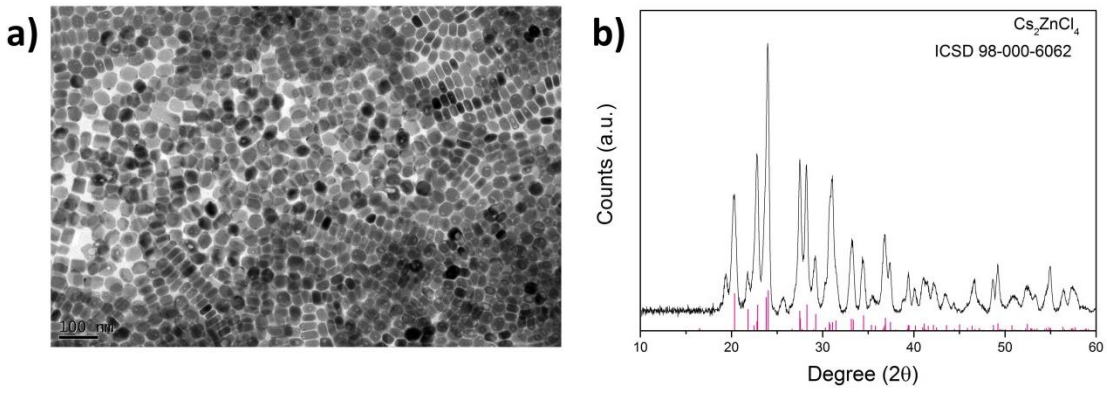

Figure 5.2: a) TEM image and b) XRD pattern of Cs_2ZnCl_4 NCs

CsCl NCs could be grown using tetrabutylammonium chloride (TBAC), but they were non-uniform and polydisperse (Figure 5.3a). CsCl NCs with uniform shapes and tunable sizes (20 - 35 nm) could be finally synthesized using $InCl_3$ as a Cl precursor (Figure 5.3b and 5.6a).

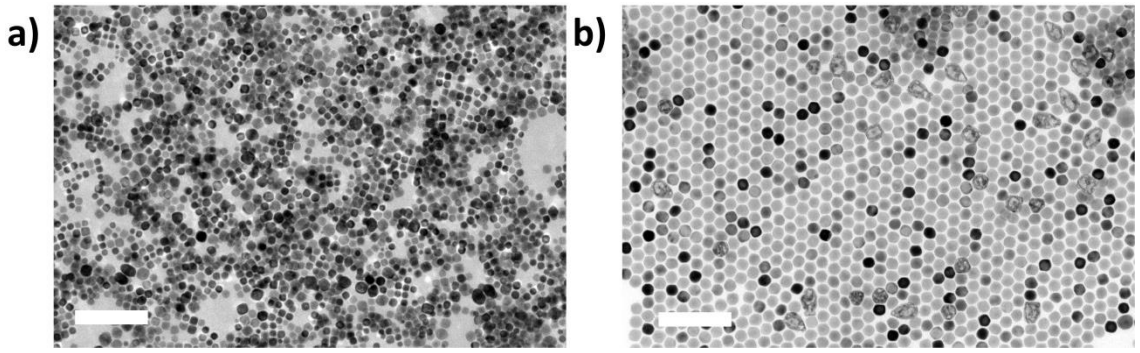

Figure 5.3: TEM images of CsCl NCs; a) by using TBAC at 90 °C; b) by using $InCl_3$ at 90°C (scale bars correspond to 100 nm)

The results of these syntheses indicate that the size of the metal cation in the halide precursor dictates the type of Cl-based compounds that can be formed. Working with small cations leads to the formation of ternary compounds, such as Cs_3CoCl_5 and Cs_2ZnCl_4. Bigger cations, however, behave as spectator cations, which leads to the formation of CsCl NCs.

CsBr. The use of tetrabutylammonium bromide (TBAB) yielded NCs with broad size distributions (Figure 5.4b). CsBr NCs with uniform shapes and tunable sizes were prepared by using either $ZnBr_2$ or $CoBr_2$ as Br precursors (Figure 5.6b and 5.4b).

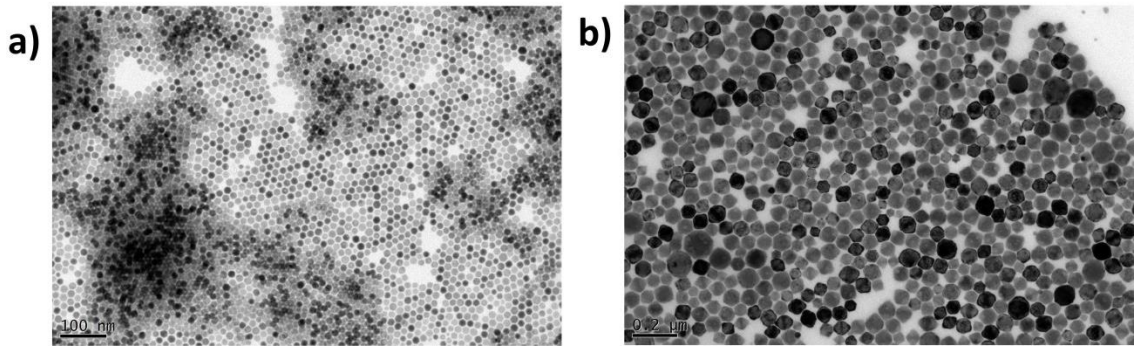

Figure 5.4: TEM images of CsBr NCs; a) by using $CoBr_2$ and b) by using TBAB (scale bars correspond to 100 nm)

By employing ZnBr, the size of the CsBr NCs could be adjusted in the range of 13 to 30 nm by varying the reaction temperature (50 – 120 °C). However, reactions at 120 °C and above resulted in a broad size distribution (Figure 5.15).

CsI. CsI NCs were prepared using ZnI_2 (Figure 5.6c). Similar to the other halides, tetrabutylammonium iodide could also be used as an iodide precursor, but this again yielded a

polydisperse product (Figure 5.5a). Interestingly (and somewhat similar to the synthesis of the $CsPbX_3$ NCs[79]), the growth of CsI NCs was faster than that of Cl- or Br-based NCs at the same temperature.

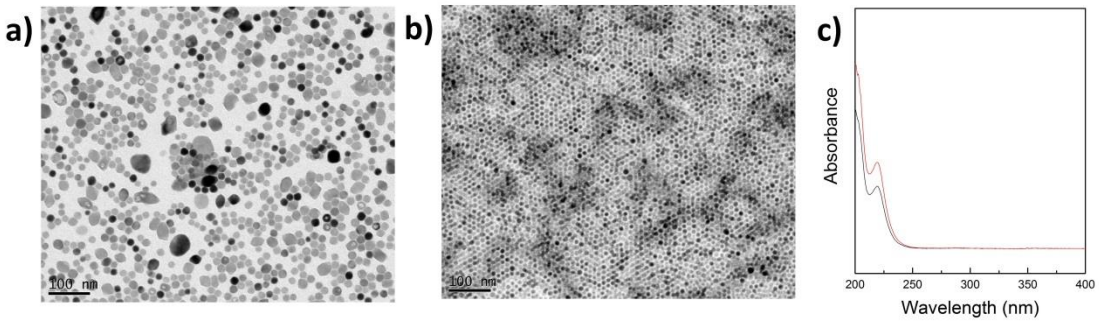

Figure 5.5: a) TEM image of CsI NCs prepared at 90 °C by using TBAI; b) TEM image of 10 nm CsI NCs synthesized at 50 °C by using ZnI_2; b) absorption spectra for two different sizes (10 nm (panel b) and 22 nm (figure 1c)).

Therefore, to better control the size of the NCs, the syntheses were performed at a lower temperature range than that of the CsCl and CsBr cases (see Table 5.1).

Table 5.1: . Reaction conditions for the synthesis of CsX NCs

CsX	Halide precursor	T (°C)	Size (nm)
CsCl	TBAC	90	PD[a] (cubes)
	$InCl_3$	90-130	20±2 - 35±3
CsBr	TBAB	90	PD (cubes + truncated octahedra
	$ZnBr_2$	50-120	13±1 - 30±4
CsI	TBAI	90	PD (irregular shapes)
	ZnI_2	50-90	10±1 - 22± 2

[a]PD: polydisperse

The absorption spectra of the CsX NCs are shown in Figure 5.6d. All these materials are essentially insulators and have large band gaps, therefore no band gap absorption should be observed down to 200 nm. Even for CsI, which has a 6.4 eV gap[159], the onset should be at around 190 nm. The peak at ~220 nm for CsI (~5.6 eV) is most likely associated with the lowest energy state of the $\Gamma(3/2,1/2)$ exciton,[160, 161] as is seen in bulk films of CsI. This exciton arises as a result of the transition from the Γ_{8^-}valence band states to the Γ_{6^+} conduction band states.[160, 161] The reason that this state is located so far below (~0.8 eV) the conduction band minimum for CsI is because CsX has highly ionic lattices[162] with low dielectric constants, therefore excitons in these materials have large binding energies. The narrow

absorption band at 220 nm is independent of the size of the CsI NCs (Figures 5.5b,c) and is comparable to that of bulk film.[160, 161]

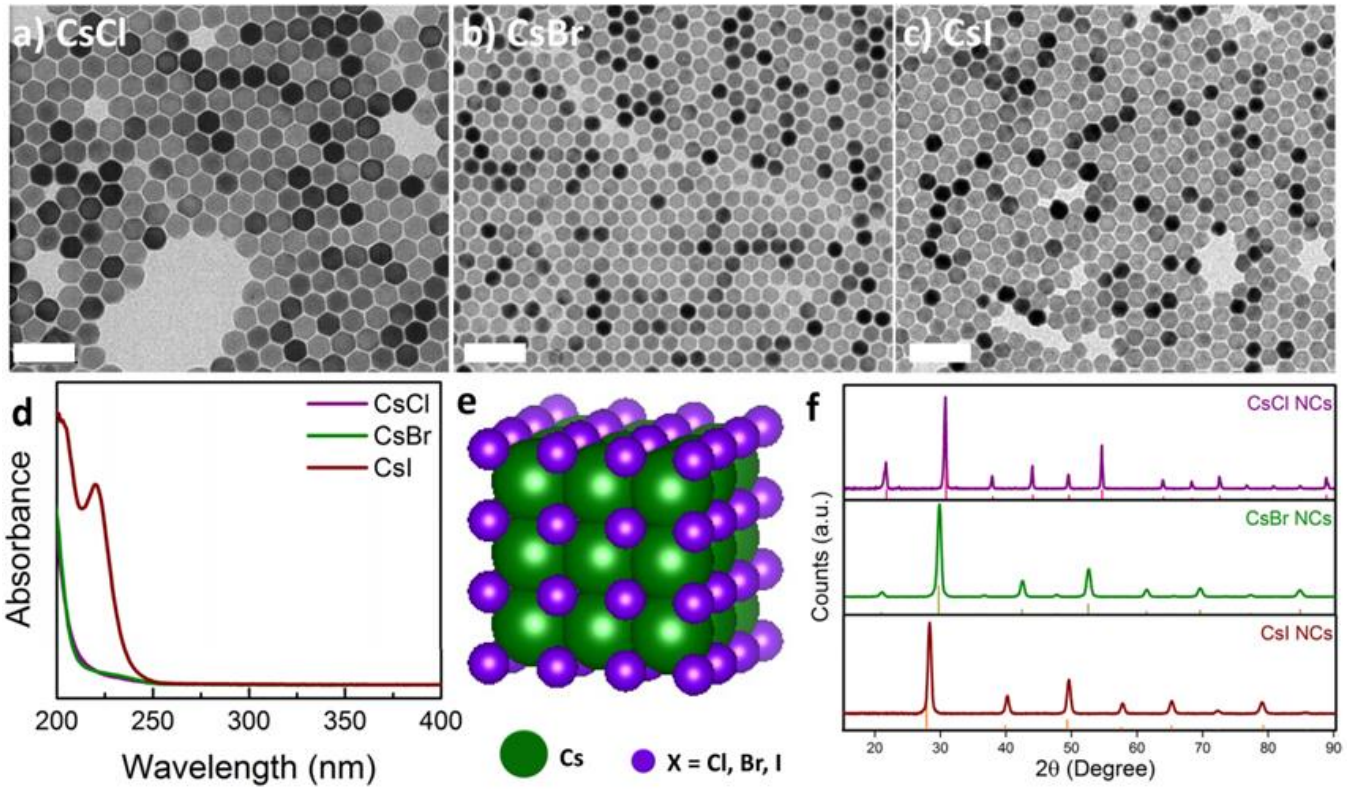

Figure 5.6: (a-c) Transmission electron microscopy (TEM) images of representative samples of CsX NCs. Scale bars are 100 nm in all images; d) Optical absorption spectra of CsX NCs dispersed in hexane; e) Sketch of the cubic structure of CsX; f) XRD patterns of the dried powders of CsX NCs, in comparison with the ICSD reference patterns (CsCl: 98-062-2366, CsBr: 98-002-2174, CsI: 98-004-4291).

This, again, is due to the strong exciton binding energy and consequent small exciton Bohr radius, hence a negligible quantum confinement effect would be seen in CsI. The absorption tails, which are in the region of 220-250 nm for CsBr and CsCl, are less understood, and might be due to deep trap states. The features around 200 nm are due to solvent absorption. X-ray diffraction (XRD) patterns of the dry powders of the as-prepared CsX NCs are in good agreement with the CsX simple cubic reference patterns, as shown in Figures 5.6e,f (both Cs^+ and X^- ions have eightfold coordination in the simple cubic structure). The absence of any other impurity phase in the patterns proves that the cations that were introduced with the halide ions in the synthesis (e.g. Zn^{2+}, In^{3+}, etc.) do not form any crystalline compounds and are eliminated during the cleaning of the NCs, as complexes with the excess surfactant molecules used in the synthesis.

The CsX NCs were then used as colloidal precursors to synthesize $CsPbX_3$ NCs. We focus most of our discussion on the transformation of CsBr to $CsPbBr_3$ NCs. Our first attempt was to react CsBr NCs with

an excess amount of $PbBr_2$ (which was dissolved in a mixture of OLA, OA and ODE) according to the scheme:

$$CsBr + PbBr_2 \rightarrow \quad CsPbBr_3 \qquad (1)$$

These reactions were only partially successful. The reactivity of this system was low at room temperature, and resulted in mixtures of $CsPbBr_3$ nanocubes and partially transformed CsBr NCs, with a double peak feature in PL (Figure 5.7) after an overnight reaction.

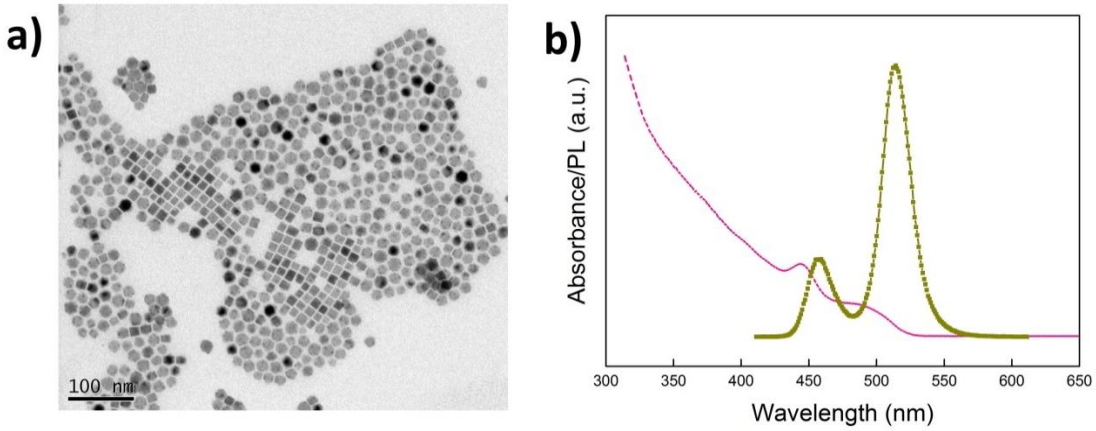

Figure 5.7: Results of transformations induced by exposing the CsBr NCs to an excess amount of $PbBr_2$ at room temperature, overnight: a) TEM image; b) optical absorption (violet) and emission (green) spectra.

Reactions at higher temperatures (70 °C) were poorly controllable, the size distribution of the $CsPbBr_3$ NCs was multimodal, as is evident from the multiple peaks in the PL spectrum (Figure 5.8)

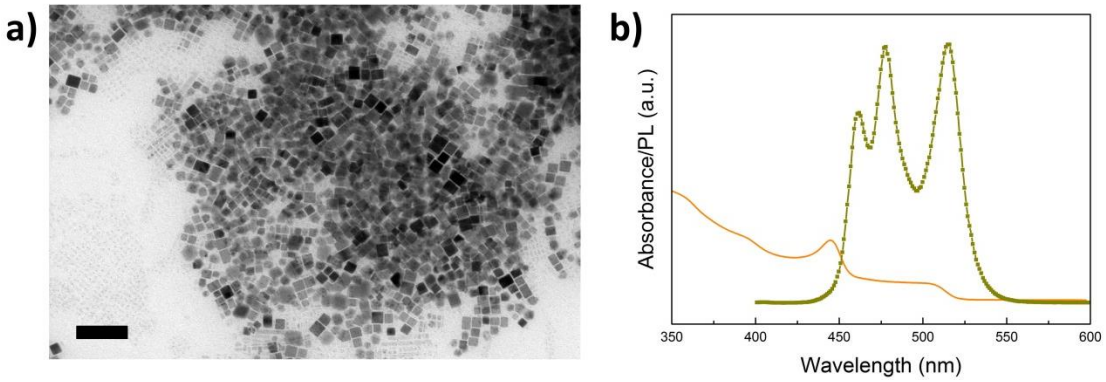

Figure 5.8: Results of transformations induced by exposing the CsBr NCs to an excess amount of $PbBr_2$ at 70 °C for 1 minute: a) TEM image (scale bar is 100 nm); b) optical absorption (violet) and emission (green) spectra.

Better control was possible by reacting the CsX NCs with Pb oleate ($Pb(OA)_2$, which was prepared by dissolving PbO in oleic acid), according to the scheme:

$$3CsX + Pb(OA)_2 \rightarrow \; CsPbX_3 + 2CsOA \qquad (2)$$

During preliminary tests, we employed small amounts of $Pb(OA)_2$ to investigate the initial stage of this reaction (see the experimental section). In this case, the solution turned fluorescent blue (with a peak at 468 nm and a PLQY of 22%), immediately after the addition. Such a blue PL was probably due to the formation of quantum confined $CsPbX_3$ domains on the surface of the CsBr NCs, whose shape remained essentially truncated octahedral at this stage (Figure 5.9).

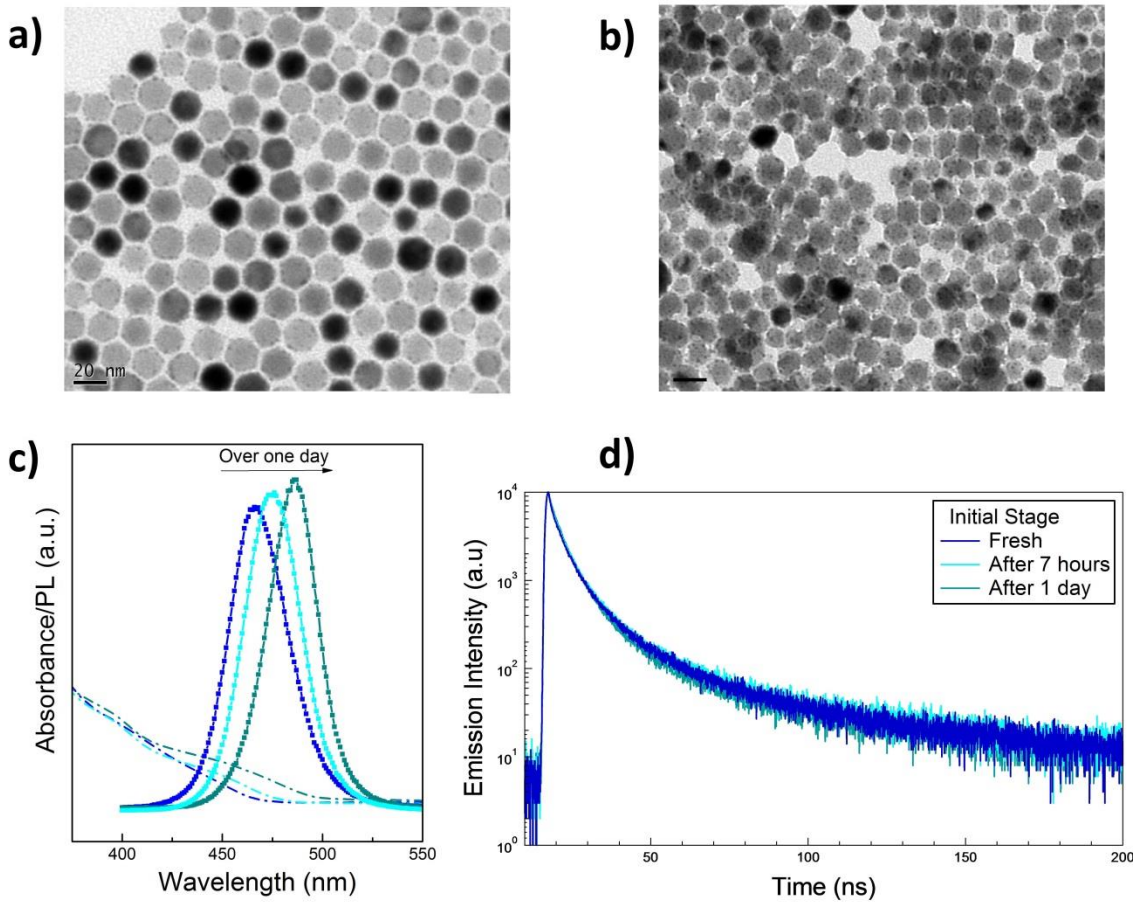

Figure 5.9: Initial stage of the CsBr to $CsPbBr_3$ transformation: TEM images of a) fresh sample and b) aged sample (scale bars are 20 nm); c) optical spectra of confined domain over one day (PL peak varies from 468 nm to 486 nm); d) corresponding time-resolved PL decays for the confined CsPbBr3 domain over one day (PL decay slightly increased from 4.49 ns to 4.81 ns).

The optical absorption and PL spectra of this sample red-shifted considerably over one day; the PL peak shifted from 468 to 486 nm, (see Figures 5.9c; and Figure 5.9d for the corresponding PL decays) and the PLQY increased to 61%. This observation suggests the formation of bigger domains over time, even after purification step (consisting of precipitating the particles and re-suspending them in toluene). TEM analysis of a sample that was aged overnight after the purification step evidenced the strong aggregation of the NCs (Figure 5.9b). Reactions with larger amounts of $Pb(OA)_2$ yielded samples with a greener PL soon after the addition of the lead complex and characterized by a variety of shapes (Figure 5.10), indicating a more advanced stage in the transformation.

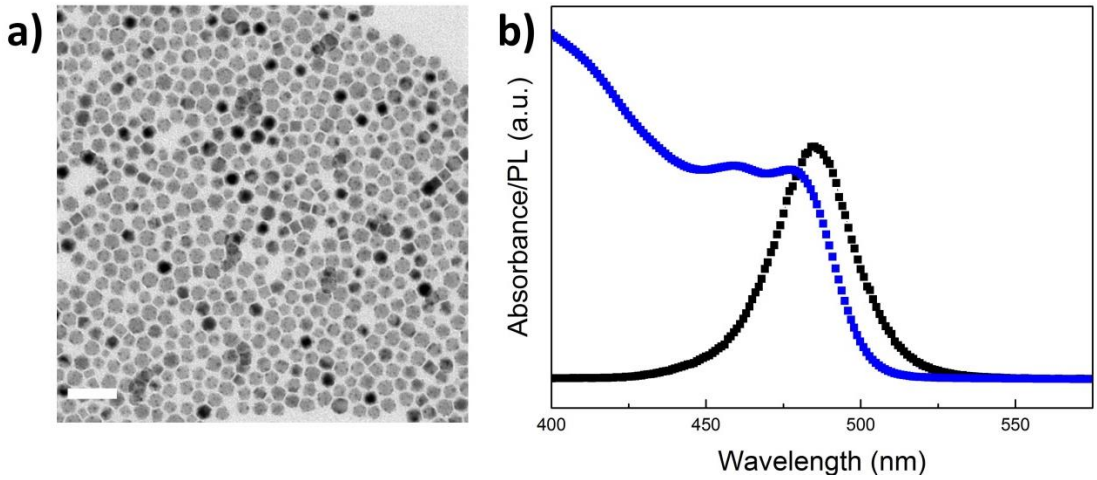

Figure 5.10: Intermediate stage of CsBr to $CsPbBr_3$ transformation a) TEM image and b)optical spectra; two absorption peaks and wide FWHM (31 nm) of PL present poor control over the shell thickness at intermediate stage (scale bar corresponds to 50 nm).

Finally, nearly monodisperse, pure $CsPbBr_3$ NCs could be prepared by adding an excess amount of $Pb(OA)_2$, as is detailed in the experimental section.

The samples at different stages of the transformation were characterized by the presence of an increasingly thicker perovskite shell on the CsBr NCs (Figure 5.11).

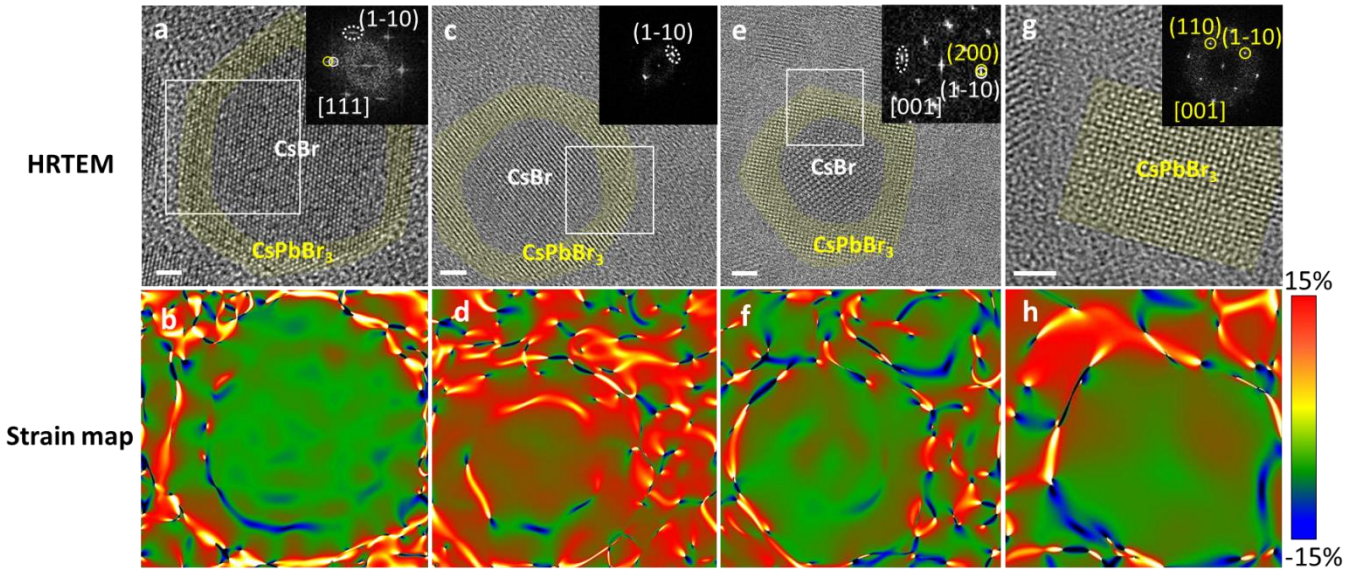

Figure 5.11: HRTEM images of NCs during different stages of the CsBr → $CsPbBr_3$ transformation (top) and corresponding strain maps (Δ_{xy}), obtained by geometric phase analysis (bottom). The perovskite domains are color coded in yellow. (Figure 5.12 shows a broader set of intermediate samples, without color coding). The scale bar is 2 nm; (a, b) A NC in its early stage, with a thin $CsPbBr_3$ shell; (c, d and e, f) Two NCs in their intermediate stages; (g, h) A fully transformed $CsPbBr_3$ NC. In panels a, c, and e, the inset is the FFT of the region which is delimited by the white box. The inset of panel g is the FFT of the whole image.

The samples at different stages of the transformation were characterized by the presence of an increasingly thicker perovskite shell on the CsBr NCs (Figure 5.11). Geometric phase analysis (GPA) was carried out on the HRTEM images of the NCs, which revealed a variation in the periodicities of the HRTEM contrast, and a strain at the interface of the core and shell regions. The initial CsBr NCs, as well as the samples in the early stages of the transformation, were often found oriented in the [111] zone axis, which is evidenced by a fast Fourier transform (FFT) showing six spots at equal angles (60˚, Figure 5.11a). Even in the early stages of the transformation, the presence of $CsPbBr_3$ can be inferred by the elongated spots in the corresponding FFT images (which is highlighted by the white elliptical contour in the inset of Figure 5.11a) and by the presence of a strained interface separating the core and the shell. The orientational relationship between the CsBr core and the $CsPbBr_3$ shell in these early samples (Figures 5.11) is CsBr [111] // $CsPbBr_3$ [001] and CsBr (1-10) // $CsPbBr_3$ (200). NCs with thicker $CsPbBr_3$ shells tended to be oriented in such a way that the CsBr lattice is in the [001] zone axis (Figures 5.11e, f). Notably, in samples with thicker $CsPbBr_3$ shells (Figures 5.11e, f), the orientational relationship between the core and the shell is different to that of thin shell samples, and is as follows: CsBr [001] // $CsPbBr_3$ [001], CsBr (1-10) // $CsPbBr_3$ (200) (see Figure 5.12 for more HRTEM images of the intermediate stages). Interestingly, this shape reduced the strain at the interface (see Figure 5.11f). The progressive transformation, namely the full conversion to $CsPbBr_3$ (Figure 5.11g, h) was indeed accompanied by a morphological change of the whole particle.

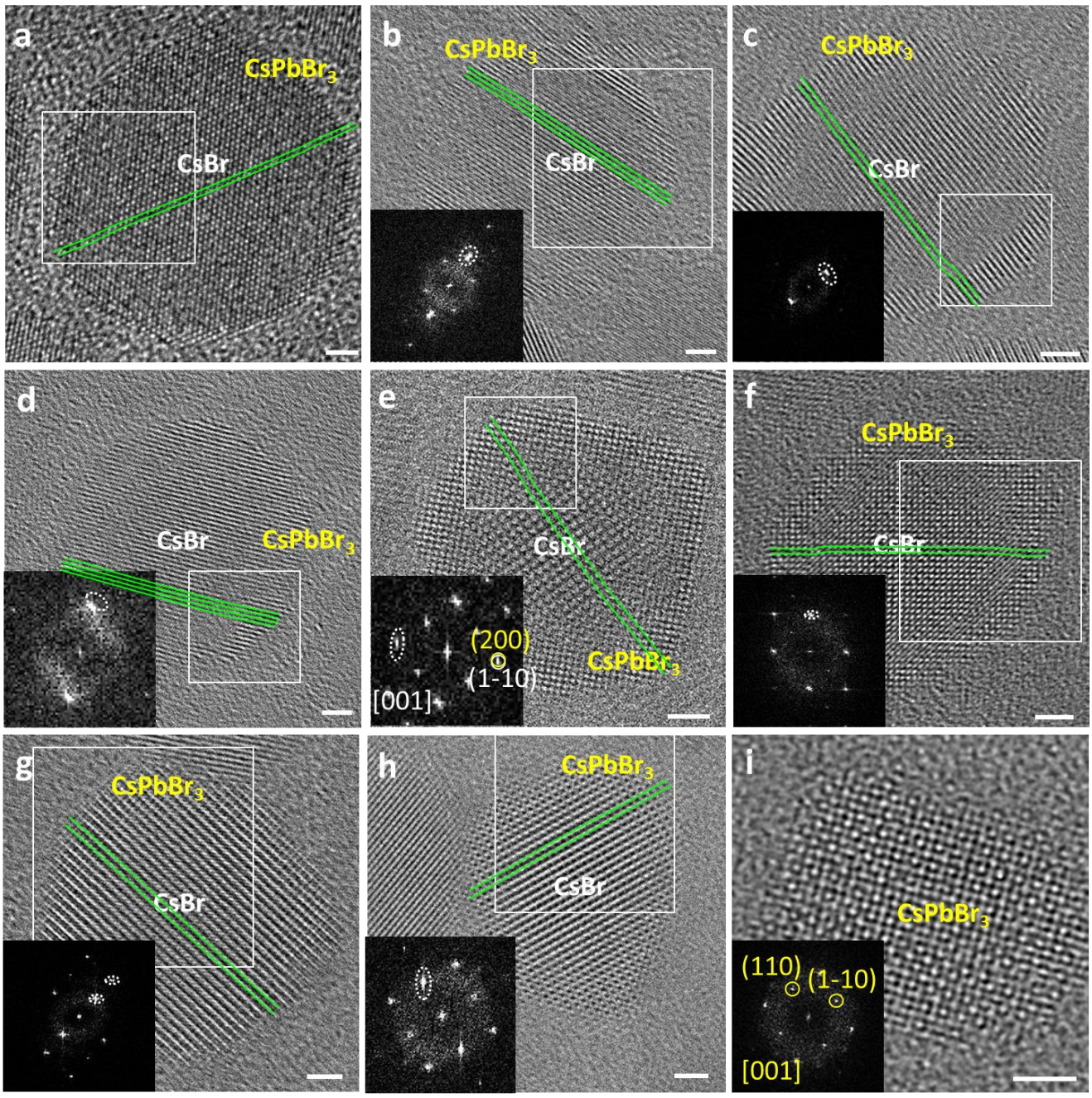

Figure 5.12: A set of HRTEM images related to intermediate stages (a-h) and final stage (i) of the transformation of CsBr NCs to $CsPbBr_3$ NCs (scale bar is 2 nm in all images). Green lines are drawn along the fringes

The presence of the (Pb rich) perovskite shell in the intermediate samples was further confirmed by scanning TEM (STEM)-energy dispersive spectroscopy (EDS) analysis (see Figure 5.13): EDS evidenced a higher concentration of Pb in the outer regions of the NCs with respect to the central regions[163].

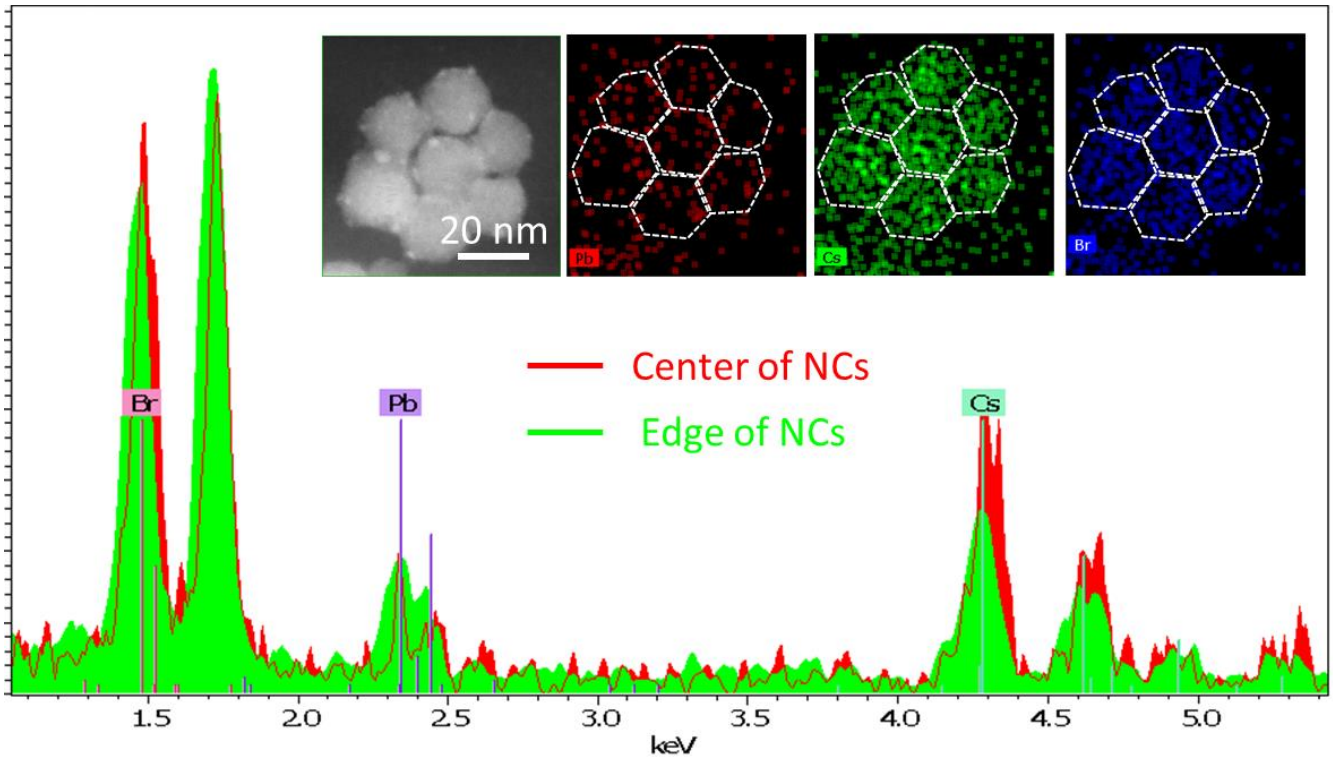

Figure 5.13: EDS analysis of CsBr NCs that had been partially converted to $CsPbBr_3$. The Main plot reports EDS spectra. The red signal corresponds to a sum of several EDS spectra collected from the edge regions of the NCs. The green signal corresponds instead to a sum of several EDS spectra collected from the edge regions of the NCs. The central regions are richer in Cs and poorer in Pb compared to the edge regions. This fits into a model of a core/shell $CsBr/CsPbBr_3$ for these partially converted NCs. Insets: from left to right: HAADF-STEM image and corresponding elemental maps of Pb, Cs, and Br.

CsBr NCs within a range of sizes (13-30 nm) could be fully transformed into $CsPbBr_3$ NCs (7-23 nm) at room temperature by adding an excess amount of $Pb(OA)_2$, as shown in Figure 5.14 for three different sizes of the starting CsBr NCs. In this case, not only did the NCs undergo a shape transformation (from truncated octahedral to cubic) but their overall size was also reduced. Although the transformation from CsBr to $CsPbBr_3$ entails the expulsion of two Cs^+ ions per every Pb^{2+} ion added, one should not expect such a large change in the volume of the particles, since the two materials have similar densities (4.44 g/cm^3 for CsBr and 4.75 g/cm^3 for $CsPbBr_3$) [164]. The initial NCs therefore appeared to have undergone partial dissolution during the transformation, and this is understandable if one considers that the lattice needs to reorganize considerably when going from cubic CsBr (with both Cs^+ and Br^- ions in octahedral coordination) to the perovskite structure. However, as can be seen from Figure 5.14, the size of the final $CsPbBr_3$ NCs is correlated to that of the initial CsBr NCs. This fact, and the evidence that $CsPbBr_3$ NCs were not observed growing separately from the CsBr NCs, while instead only intermediate core/shell structures were observed, excludes that the overall transformation goes

through the dissolution of the CsBr NCs followed by the recrystallization of $CsPbBr_3$. Optical data and XRD analyses further confirmed the full transformation of CsBr to $CsPbBr_3$, as shown in Figure 5.14d,e (additional two sizes of initial CsBr and final $CsPbBr_3$ NCs are shown in Figure 5.15).

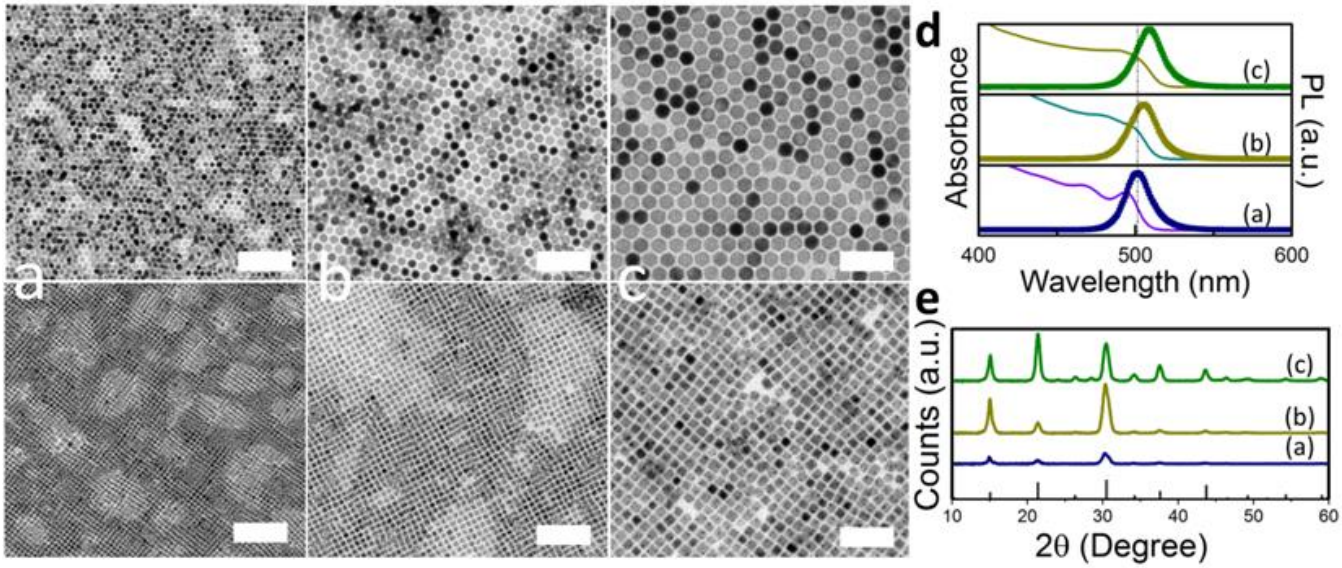

Figure 5.14: TEM images of CsBr NCs of three representative sizes (top panels) and corresponding TEM images of the resulting $CsPbBr_3$ NCs (bottom panels). Scale bars correspond to 50 nm in all images; (d) Corresponding optical spectra and (e) XRD patterns of the resulting $CsPbBr_3$ NCs (ICSD reference pattern: 98-009-7852).

All data related to the transformation such as the size of the starting NCs as well as the transformed NCs and PL peak positions with full width at half-maxima are listed in Table 5.2.

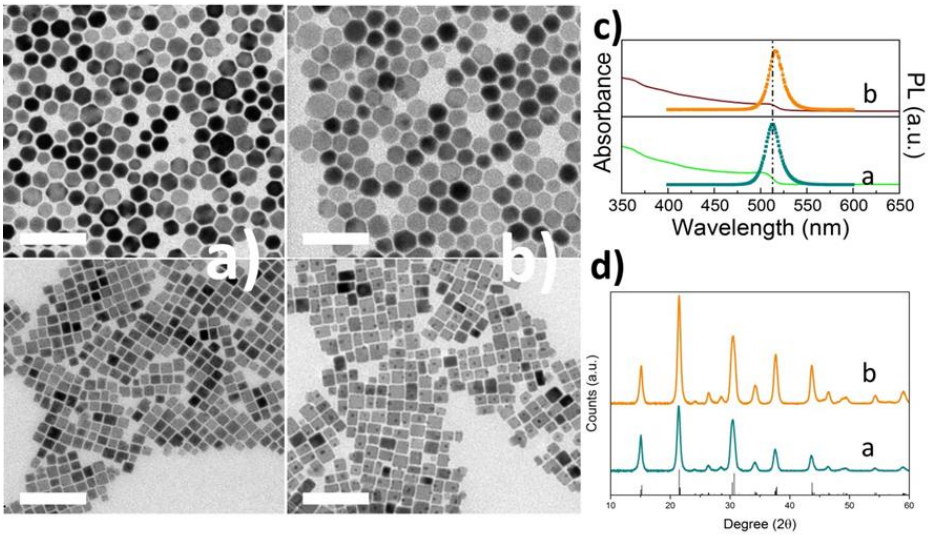

Figure 5.15: (a, b) TEM images of CsBr NCs of two additional sizes (24 and 30 nm, top panels) and corresponding TEM images of the resulting CsPbBr3 NCs (16 and 23 nm, bottom panels). Scale bars correspond to 100 nm in all images; (c) Optical spectra and (d) XRD patterns of the resulting CsPbBr3 NCs (ICSD reference pattern: 98-009-7851).

The relatively lower values of PLQY (ranging from 32% to 50%) of the $CsPbBr_3$ NCs prepared with our approach compared to those of the NCs prepared by direct synthesis (50% – 90 %) demonstrate the formation of structural and surface defects acting as trap states during such a conversion. These are probably also the reason for the non-exponential PL decay of all samples (Figure 5.16). For the fitting we required a sum of four exponentials (Table 5.2).

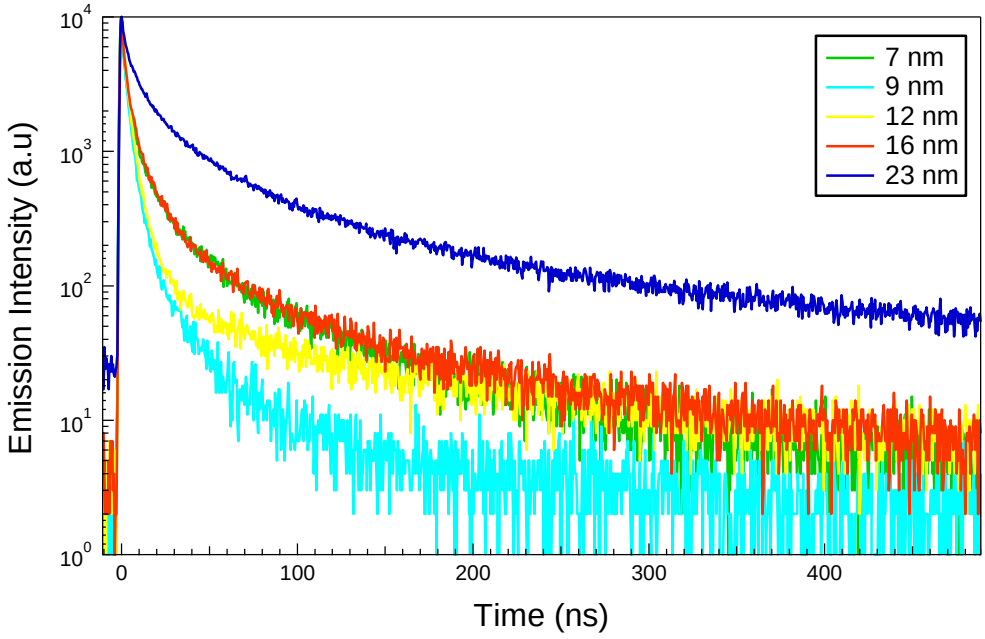

Figure 5.16: Time-resolved PL decays for all different sizes of $CsPbBr_3$ NC samples

We calculated the amplitude-averaged decay time, and found values of 3 ns - 5 ns for all $CsPbBr_3$ NCs except those with a 23 nm diameter, for which we obtained 17 ns. These values are generally in line with those of $CsPbBr_3$ NCs prepared by direct synthesis[79].

Table 5.2: Dataset of full transformation of CsBr NCs

Sample	Reaction Temperature of CsBr (°C)	Size of CsBr (nm)	Size of $CsPbBr_3$	PL Peak (nm)	FWHM (nm)	PLQY % (pretreatment)	Average PL lifetime (ns)
Figure 5.14a	50	13 ± 1	7 ± 0.5	500	20.6	49.1	4.48
Figure 5.14b	80	16 ± 1	9 ± 1	504	22.6	50.9	2.91
Figure 5.14c	90	20 ± 1	12 ± 1	509	21.7	50.1	3.89
Figure 5.15a	100	24 ± 3	16 ± 3	512	20.1	38.1	5.02
Figure 5.15b	120	30 ± 4	23 ± 3	517	20	32.5	17.16

Recently, Koscher et al. have reported a postsynthetic modification of $CsPbBr_3$ NCs in which adding a thiocyanate salt to the as-prepared perovskite NCs could effectively decrease the nonradiative exciton recombination[165]. We followed a modification of that protocol here, by adding a solution of $Pb(SCN)_2$ dissolved in OLA and OA and ODE to the NCs before the washing step. This treatment greatly improved the PLQY. As an example, in the case of the 16 nm $CsPbBr_3$ NCs the PLQY went from 38% to 60%. Adding a high excess of $Pb(SCN)_2$ solution did not raise the QY further. Although the overall increase was remarkable, the PLQY still did not reach the record values of the one-step grown $CsPbBr_3$ NCs, suggesting that our NCs have residual structural defects. In addition, the lower PLQY of the bigger $CsPbBr_3$ NCs is a possible indication that structural defects were also present inside the NCs, and these are more likely to occur in bigger NCs.

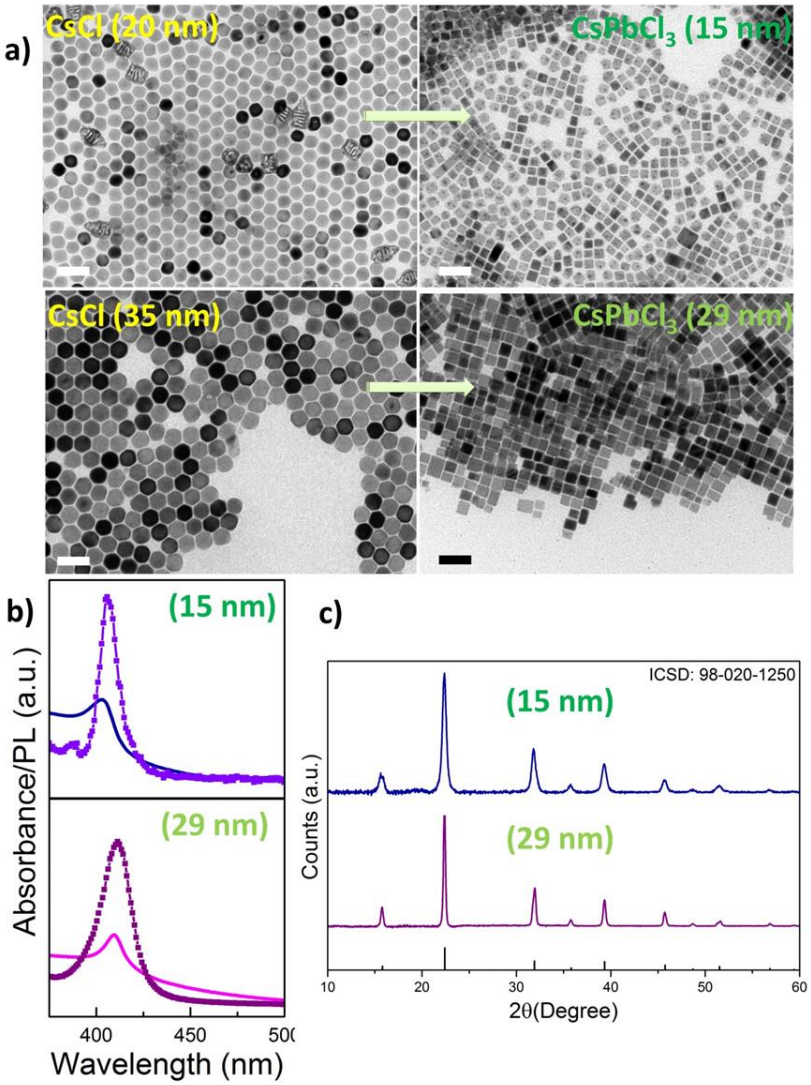

Figure 5.17: A) TEM images of initial CsCl NCs (two different sizes, 20 nm (synthesized at 90 °C) and 35 nm (synthesized at 130 °C)) and the corresponding $CsPbCl_3$ NCs (15 and 29 nm, respectively). Scale bars correspond to 50 nm; b) optical spectra and c) XRD patterns of the two samples of $CsPbCl_3$ NCs.

CsCl and CsI NCs could also undergo the same type of transformation, delivering the corresponding perovskite NCs under the same reaction conditions. In the case of the CsCl NCs, there was a clear correlation between the size of the initial NCs and that of the corresponding perovskite NCs. For example, starting from two different sizes of CsCl NCs (20, 35 nm) we could prepare $CsPbCl_3$ NCs with average sizes of 15 and 29 nm, respectively. Figure 5,17 reports TEM images of the initial CsCl NCs, as well as optical, structural and morphological characteristics of the final $CsPbCl_3$ NCs. For CsI, the final $CsPbI_3$ NCs were considerably polydisperse (see Figure 5.18). In addition further investigation was in part compromised by the fast degradation of the final $CsPbI_3$ NCs.

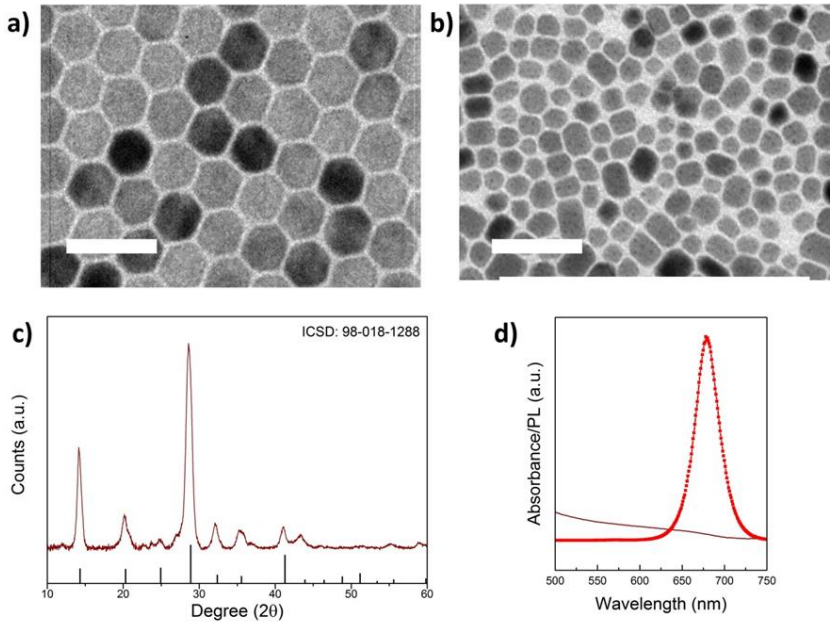

Figure 5.18: a-b) TEM images of a sample of a) CsI NCs (22 nm, synthesized at 90 °C)) and; b) corresponding $CsPbI_3$ NCs after the transformation. Scale bars correspond to 50 nm in both images; c) XRD pattern and d) optical spectra of the $CsPbI_3$ NCs.

Other Pb compounds were also tested to react with the CsX NCs in the attempt to transform them into $CsPbX_3$ NCs. We tested for example hexaphenyl lead (HPL, powder), which is easily soluble in toluene. This compound did not react with the CsX NCs at room temperature, as it required higher temperatures (100◦C or higher) to decompose and release Pb^{2+} ions. Unfortunately, under these conditions the CsX NCs were dissolved. A similar outcome was seen when employing $Pb(SCN)_2$, this time dissolved in a mixture of OLA, OA and ODE. Like the $PbBr_2$ and HPL cases, this compound was not enough reactive towards the CsX NCs at room temperature.

5.4. Conclusion

In summary, we have reported a simple colloidal synthesis of CsX (X = Cl, Br, I) NCs with uniform shape and tunable size. Such NCs can then be used as colloidal precursors to synthesize $CsPbX_3$ NCs upon reaction with Pb^{2+} ions. A potential advantage of having monodisperse CsX NCs is that they should serve as precursors for other types of NCs including Cs^+ and halide ions in their composition, in addition to the halide perovskite NCs reported here.

6. N-Methylformamide as a Source of Methylammonium Ions in the Synthesis of Lead Halide Perovskite Nanocrystals and Bulk Crystals

Abstract: We report chemical routes for the synthesis of both nanocrystals and bulk crystals of methylammonium (MA) lead halide perovskites employing N-Methylformamide (NMF) as a source of MA ions. Colloidal nanocrystals were prepared by a transamidation reaction between NMF and an alkyl amine (oleylamine). The nanocrystals showed photoluminescence quantum yields reaching 74% for $MAPbBr_3$ and 60% for $MAPbI_3$. Bulk crystals were grown at room temperature, with no need for an antisolvent, by the acid hydrolysis of NMF. Important advantages of using NMF instead of MA salts are that the syntheses involve fewer steps and less toxic and less expensive chemicals.

Parts of this chapter have been adapted or reproduced with permission from:

Shamsi, J.; Abdelhady, A. L.; Accornero, S.; Arciniegas, M.; Goldoni, L.; Kandada, A. R.; Petrozza, A.; Manna, L., N-Methylformamide as a Source of Methylammonium Ions in the Synthesis of Lead Halide Perovskite Nanocrystals and Bulk Crystals. *ACS Energy Lett* 2016, 1, 1042-1048.

6.1. Introduction

The rapid increase in the power conversion efficiencies of solution-processed hybrid lead trihalide perovskite solar cells, which have reached 22.1%[166] to date, has captured their worldwide attention and has started a race on developing new synthesis approaches and studying the many fascinating properties of these materials.[22, 167-169] Besides solar cells, hybrid perovskites have demonstrated significant performance as active layers in several other optoelectronic devices, including photodetectors[48, 170, 171] and light emitting diodes[172, 173]. Another notable feature of hybrid perovskite-based devices is their facile solution processability. Hybrid perovskites can be fabricated as nanocrystals (NCs), thin films, or single crystals. Each of these forms has peculiar optical and/or electrical properties. For instance, NCs of $CH_3NH_3PbBr_3$ ($MAPbBr_3$) have an absorption onset at 505 nm[174, 175] while the thin films and single crystals counterparts have absorption onsets at 544 nm[176] and 570 nm,[177] respectively. Each of these forms has its own preferred fields of applications: thin films are ideal for solar cell devices,[176 178] while NCs are superior in display technology, due to their higher photoluminescence quantum yield (PLQY).[177] On the other hand, single crystals, besides having been employed in optoelectronic devices,[45, 49] represent the best platform to determine the actual properties of the material such as carriers' diffusion length and lifetime.[174, 175]

To date, the synthesis of $MAPbX_3$ ($X = Cl^-$, Br^- or I^-) perovskites has been carried out using MAX salts as precursors for MA ions. These salts are generally prepared by the dropwise addition of HX to an ethanolic solution of methylamine.[179] After 2 hours of stirring in an ice bath, MAX is then recrystallized and dried overnight. The in-house synthesis of MAX is a common step in most research groups, as the commercially available MAX salts are costly. The second step involves mixing the dried MAX with the corresponding PbX_2 salt in the appropriate solvent. Dimethyl sulfoxide (DMSO),[171, 180] *N*,*N*-dimethylformamide (DMF)[171, 174, 175, 181] and γ-butyrolactone (GBL)[171, 174, 175, 181] are the apt solvents to fabricate bulk scale Cl-, Br- and I-based perovskites, respectively. This is attributed to the different solubilities of the precursors in these solvents. In case of colloidal perovskite NCs, multiple synthetic methodologies, including ligand-assisted reprecipitation[177] and hot-injection techniques[79], have been developed for the synthesis. Unlike the all-inorganic $CsPbX_3$ NC counterparts, which are mainly obtained in cube shapes of around 7- 8 nm in size,[182, 183] $MAPbX_3$ NCs are synthesized in roughly spherical shapes with sizes around 3.3- 6 nm.[177, 184-186] A recent hot injection synthesis by Vybornyi *et al.*[87] could deliver cubic shapes for $MAPbI_3$ NCs and nanoplatelets for $MAPbBr_3$, but apparently could not be extended to $MAPbCl_3$ NCs.

Herein, we report a general route involving fewer steps, less toxic chemicals[187] and reduced cost for the fabrication of $MAPbX_3$ perovskites in both NCs and bulk forms, compared to the various previous approaches. Our method proceeds without firstly synthesizing and purifying MAX, as well as avoiding the procurement of the expensive MA salts and eliminating the use of toxic DMF. We used instead *N*-methylformamide (NMF) as a source of MA, through a transamidation reaction between NMF and oleylamine (OLA, scheme 1), by which we could synthesize colloidal $MAPbX_3$ NCs with a record PLQY of 60% for the $MAPbI_3$ NCs[188]. Bulk crystals were grown from NMF and PbX_2 in the presence of a hydrohalic acid (HX, aqueous solution) as a result of the acid-catalyzed hydrolysis of NMF (Scheme 6.1), as previously reported for DMF[189, 190] and other amides.[190]

Table 6.1: Summary on previous reports for bulk crystal synthesis of $MAPbI_3$

	Solvent	Anti-solvent	Temperature	Time	Reference
Inverse Temperature Crystallization (ITC)	GBL	-	110 °C	3 hours	Saidaminov, M. et. al., *Nat. Commun.*, **2015**, *6*, 7586
Antisolvent Vapor-Assisted Crystallization (AVC)	GBL	CH_2Cl_2	RT	1 week	Shi, D. et. al., *Science*, **2015**, *347*, 519
Cooling	Aqueous HI	-	Heating to 108 °C then cooling to 60 °C	1 month	Lian, Z. et. al., *J. Am. Chem. Soc.* **2016**, 138, 9409
This work	Aqueous HI - NMF	-	RT	48 hours	

Unlike other $MAPbX_3$ crystallization techniques (Table 6.1),[174, 175, 191, 192] our free-standing Cl-, Br- and I-based bulk crystals (in addition to the mixed Cl/Br and mixed Br/I bulk crystals that we could prepare) could be grown at room temperature, and without any anti-solvent.

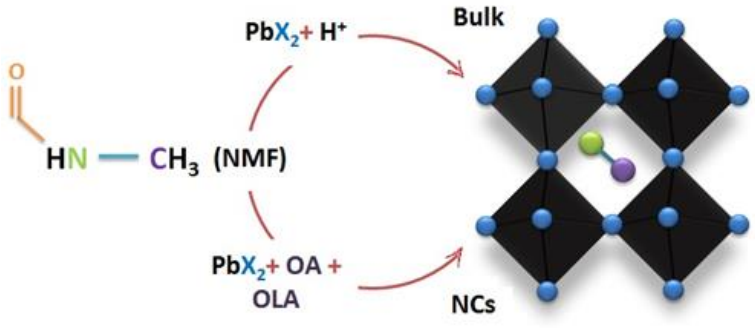

Scheme 6.1: A sketch of the two different routes, both employing N-methylformamide (NMF) as a source of methylammonium ions, for the synthesis of either perovskite nanocrystals (NCs) or bulk crystals.

6.2. Experimental Section

Nanocrystals syntheses

Preparation of stock solutions:

0.188 mmol of PbX_2 (corresponding to 0.052g of $PbCl_2$, or 0.069g of $PbBr_2$, or 0.087g of PbI_2) together with 500 µL OA and 200 µL of OLA were dissolved in 1mL of N-Methylformamide (NMF) at 100°C under vigorous stirring for 10 min. The mixture was then stored as a stock solution at room temperature (25 °C).

Synthesis of $MAPbX_3$ NCs:

An optimized amount of stock solution (corresponding to 50 µL for Cl- and Br-NCs and 20 µL for I-NCs) was injected into a given volume of dichlorobenzene (DCB, 3ML, for $MAPbCl_3$ and $MAPbBr_3$) or chloroform ($CHCl_3$, 5mL, for $MAPbI_3$) at a desired temperature (120 ◦C for $MAPbCl_3$ NCs, 100 ◦C for $MAPbBr_3$ NCs and room temperature (RT) for $MAPbI_3$ NCs) under vigorous stirring. Finally, the reaction mixture was quickly cooled by the ice-water bath.

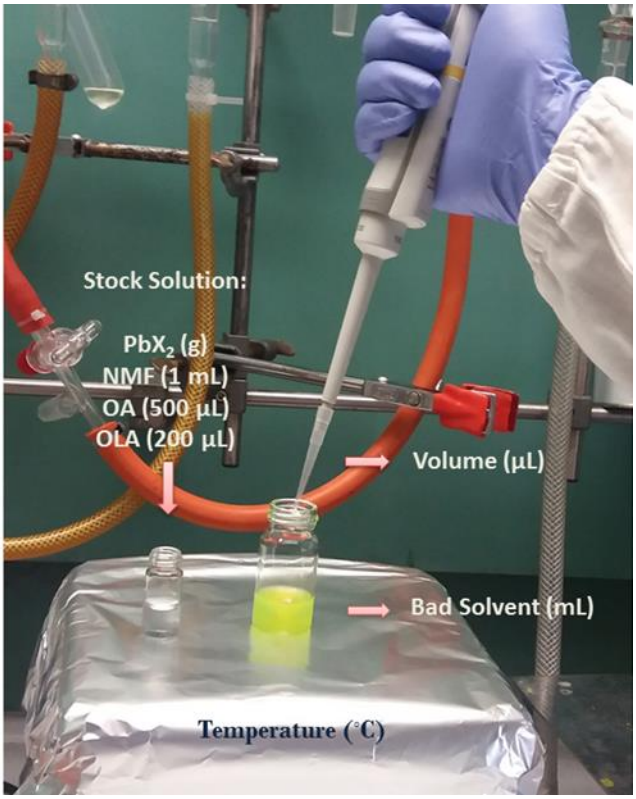

Scheme 6.2: A schematic illustration of the $MAPbX_3$ NCs synthesis

Table 6.2: Reaction conditions for the synthesis of $MAPbX_3$ NCs (DCB: 1,2-dichlorobenzene)

NCs	Salt (g)	Injection Solution Volume (µL)	Bad Solvent (mL)	Injection Temperature (°C)
$MAPbCl_3$	$PbCl_2$ (0.052)	50	DCB (3)	120
$MAPbBr_3$	$PbBr_2$ (0.069)	50	DCB (3)	100
$MAPbI_3$	PbI_2 (0.084)	20	$CHCl_3$ (5)	RT

Bulk crystals syntheses

Single crystal growth:

0.2 M $PbCl_2$ solution was prepared in HCl/NMF (1:9), 1 M $PbBr_2$ solution was prepared in HBr/NMF (1:5.7) and 0.8 M PbI_2 or $Pb(Ac)_2$ solution was prepared in HI/NMF (10:1) with the aid of vortex to dissolve the lead salts. The prepared solutions were then filtered using 0.2 µm PTFE filter syringe. 2 ml of each solution were placed in a separate vial or 10 ml in a crystallization dish and kept undisturbed for 12 - 48 hours.

6.3. Results & Discussion

We start our discussion on the release of methylamine from NMF by either transamidation or acid hydrolysis as shown in Scheme 6.3. Figure 6.1a,b reports the nuclear magnetic resonance (NMR) analysis involving ^{1}H NMR and ^{13}C NMR combined with heteronuclear single quantum coherence (HSQC), on the transamidation reaction of NMF with OLA. It reveals that there is a partial transformation of the amine (OLA) into amide (N-oleyl formamide) and in parallel the partial conversion of the starting amide (NMF) to amine (methylamine). According to the ^{1}H NMR spectrum recorded in DMSO-d6 after 10 minutes of mixing at 100 °C, two new signals at 3.05 ppm (a *pseudo quartet, J* = 6.70, 6.47 Hz) and a singlet at 2.25 ppm, were observed. The intensities of the new signals became more pronounced if the reaction was left for longer times. The multiplicity edited HSQC for the CH_2 signal in position α to an N group, returned a cross peak (2) at 2.49 and 41.4 ppm for the amine (OLA), while the cross peak (1) was shifted to 3.05 and 37.5 ppm for the amide, which are compatible with the transformation of the amine (OLA) into amide. Opposite shifts from 2.6 and 24.6 ppm to 2.25

and 28.6 ppm for the CH signal are observed (cross peak 4 and 5), indicating the formation of methylamine from NMF. Further support of the amide formation was inferred from the heteronuclear multiple-bond correlation spectroscopy (HMBC) inset in Figure 6.1b. A 1,3 interaction was observed between the signal 1 and the ^{13}C resonance at 161.2 ppm, which is typical of an amidic CO group but is different from those of NMF (161.8 and 165.2 ppm).

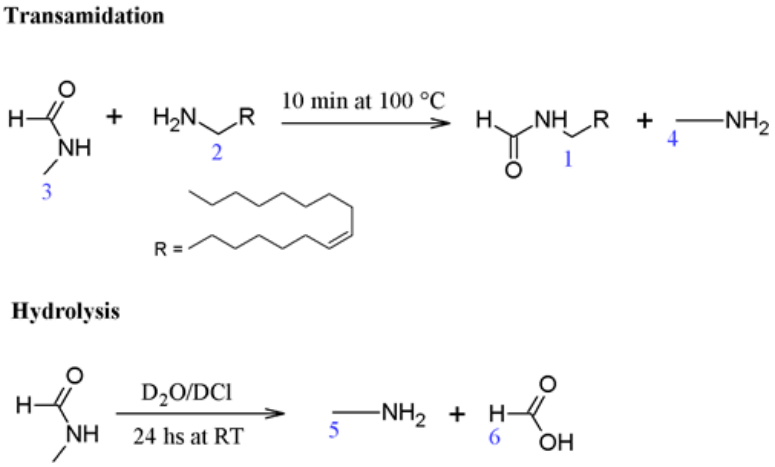

Scheme 6.3: Reaction scheme for NMF transamidation and acid hydrolysis with numbering of the highlighted protons.

Next, we investigated the *in-situ* formation of methylamine through NMF acid hydrolysis. Using deuterium chloride (DCl), 35 w% in D_2O, at a DCl:NMF volume ratio of 1:9, no hydrolysis took place after immediate mixing; the NMR spectrum was identical to that of NMF in D_2O. However, if the mixture was left stirring for 24 hours before analysis, 2 extra peaks were observed in the ^{1}H NMR (Figure 6.1c). Those two extra peaks correspond to a CH_3 bound to an amine group (5), and a C-H of formic acid (6). Similarly, 2 extra peaks were observed in the ^{13}C NMR, as shown in Figure 6.1d, corresponding to a C of a methyl bound to an amine group and to the CO of formic acid (its identity was further confirmed by spiking the sample with authentic formic acid, observing, in this way, an intensity increment of the signals). These data indicate partial hydrolysis of NMF and the possibility of the *in-situ* formation of methylammonium formate (MAF) which was previously reported to be used as an additive in the perovskite solution to promote a slower crystallization process, resulting in larger-grains perovskite thin-films.[193]

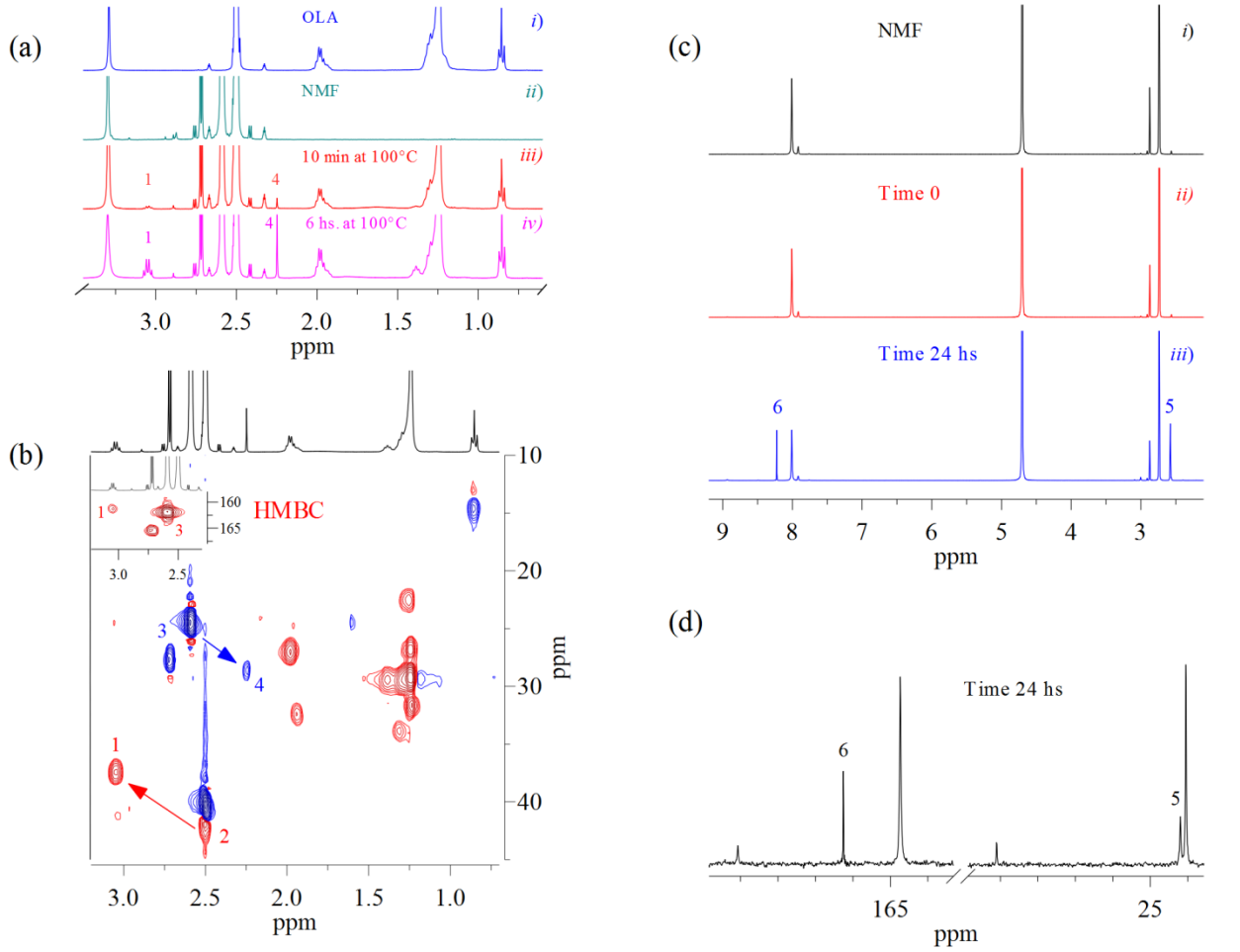

Figure 6.1: NMR analysis of transamidation and acid hydrolysis of NMF. All spectra were recorded on a Bruker AvanceIII 400 MHz spectrometer equipped with a BBI probe. (a) Superimposed 1H NMR spectra in DMSO-d6 i) OLA and ii) NMF. iii) After 10min at 100 °C, and iv) After 6hs at 100°C. (b) Multiplicity edited 1H-13C HSQC in DMSO-d6. The edited HSQC experiment returns cross peaks with opposite phases for CH_2 (in red) and for CH/CH3 (in blue). Inset: heteronuclear multiple-bond correlation spectroscopy. (c) Superimposed 1H NMR of NMF i) in D_2O ii) in D_2O/DCl Time 0, iii) in D_2O/DCl Time 24 hs. (d) 13C NMR of NMF in D_2O/DCl. Time 24 hs.

We then exploited the transamidation of NMF with OLA as a means of delivering MA ions in the synthesis of colloidal $MAPbX_3$ NCs. We adapted the synthesis described by Huang *et al.*,[184] but used NMF instead of DMF and the methyl ammonium halide (MAX). In the present system, PbX_2 and the capping ligands oleic acid (OA) and oleylamine (OLA) were dissolved in NMF, forming a precursor solution that contained all the reactants needed for the synthesis. After this solution was heated at 100 °C for 10 minutes, it was cooled at room temperature (RT) and then injected into a "bad solvent", such as dichlorobenzene (DCB) or chloroform ($CHCl_3$), heated at the desired temperature (from RT up to 120 °C), under vigorous stirring. Almost immediately after the injection, a strong fluorescence from the flask indicated the formation of the $MAPbX_3$ NCs. Pre-heating of the precursor solution at 100 °C, as well as

the presence of oleylamine in it, were necessary for the synthesis. According to the NMR data discussed earlier, MA ions are produced in the precursor solution upon heating, by a transamidation reaction between NMF and OLA, (in analogy with various types of transamidation reaction reported in the literature).[194]

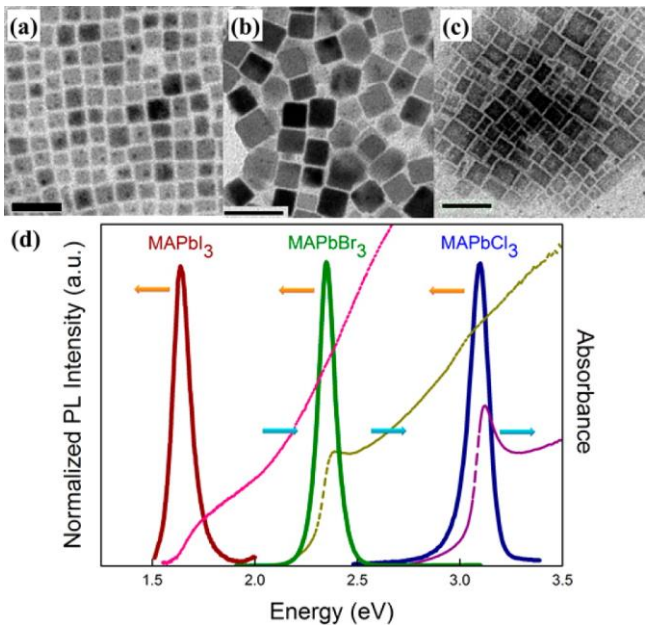

Figure 6.2: (a-c) Transmission electron microscopy (TEM) images of I-, Br- and Cl-NCs, respectively and (d) corresponding absorbance (dashed) and PL spectra (solid). All scale bars in the TEM images represent 50 nm

X-ray diffraction (XRD) patterns of the various NC samples confirmed the cubic structure for both Cl- and Br-NCs and the tetragonal phase for the I-NCs (Figure 6.3). This method enabled the synthesis of uniform, phase-pure colloidal NCs of Cl-, Br- and I–based perovskites. Figure 6.2a-c reports transmission electron microscopy (TEM) images of representative samples having cubic shapes. The resulting $MAPbX_3$ nanocubes had an average length of 21 ± 7 nm for Cl-NCs, 25 ± 3 nm for Br-NCs and 17 ± 5 for I-NCs. The $MAPbBr_3$ and $MAPbI_3$ NCs remained well dispersed for weeks. The $MAPbCl_3$ NCs had broader size distribution than the $MAPbBr_3$ and $MAPbI_3$ NCs, which resulted in tailing in the absorbance spectrum of the $MAPbCl_3$ sample and a partial sedimentation of NCs after a couple of days. The absorbance onsets and PL peak positions with full width half maxima of 0.116, 0.108 and 0.092 eV for the chloride, bromide and iodide-based NCs, respectively, were in good agreement with previously reported data (Figure 6.2d).[195, 196] Remarkably, the Br-NCs and the I-NCs had high PLQYs (74% and 60%, respectively). To the best of our knowledge, the PLQY measured for the $MAPbI_3$ NCs is the highest reported so far. Previous syntheses of $MAPbI_3$ NCs have reported typical PLQY values between 20 and 30%.[197] The $MAPbCl_3$ NCs had instead low PLQY (~3%). Similar trends

in PLQYs of halide perovskite NCs (with the Cl-NCs hitting lowest values among the three halides) have also been reported for $CsPbX_3$ NCs.[182, 198]

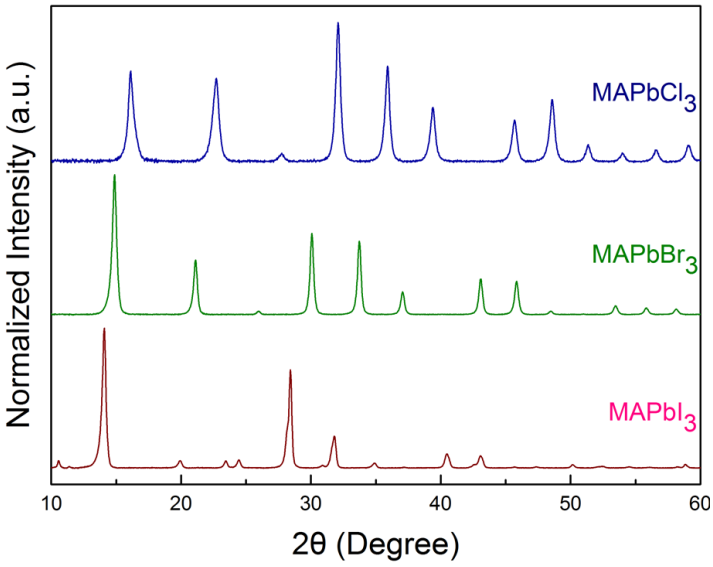

Figure 6.3: XRD patterns of the $MAPbX_3$ NCs samples

One important parameter of this approach was the injection temperature. For example, in the synthesis of $MAPbBr_3$ NCs, by adjusting the temperature of the bad solvent (in this case DCB was used), it was possible to synthesize blue-emitting spherical particles (at 60 °C, see Figure 6.4) or green-emitting cubic shaped NCs (at 100 °C, see Figure 6.2b).

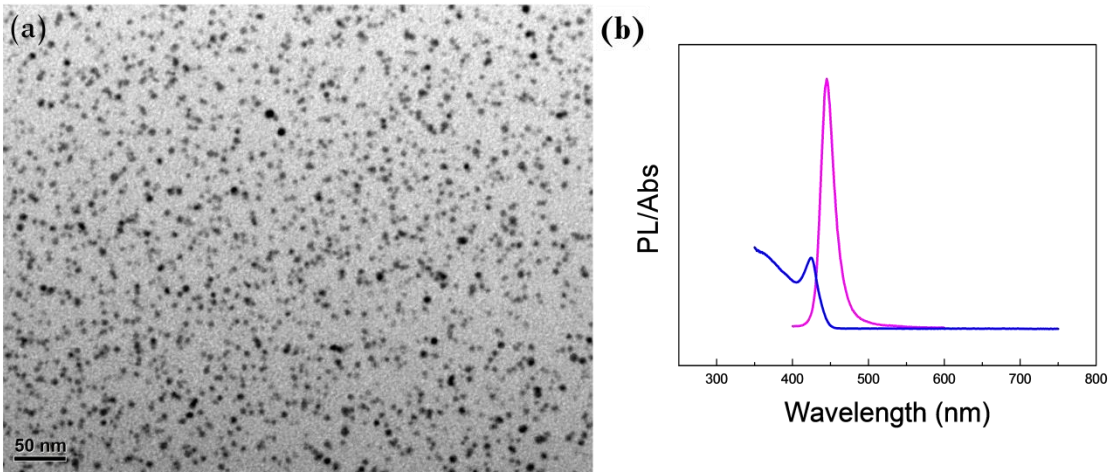

Figure 6.4: Synthesis of $MAPbBr_3$ quantum confined spherical NCs. Reaction condition: 0.069g $PbBr_2$, 0.5 mL OA, 0.2 mL OLA, 1mL NMF, 50µL of precursor solution to 3mL of DCB at 60 °C

The same reaction, at higher temperature (130 °C) yielded sheets with broad lateral size distributions (Figure 6.5a).

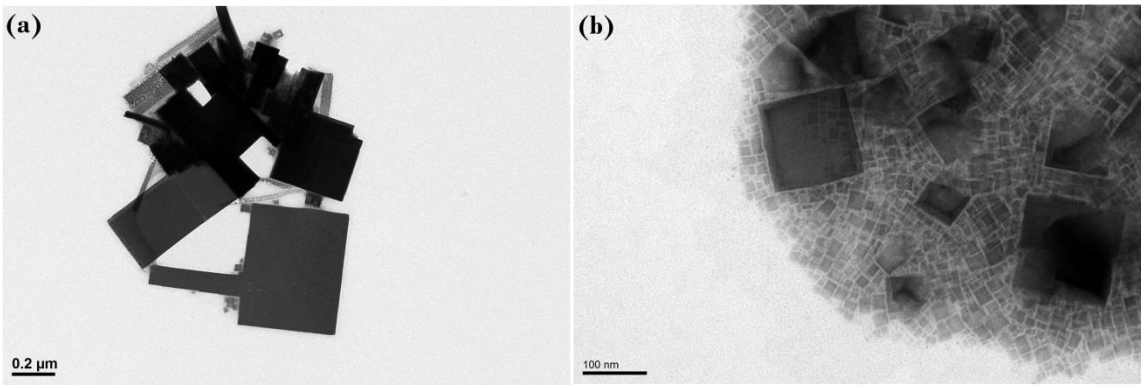

Figure 6.5: effect of higher reaction temperature and higher reaction time on MAPbBr3NCs. Reaction condition: (a) 0.069g $PbBr_2$, 0.5 mL OA, 0.2 mL OLA, 1mL NMF, 50µL of precursor solution to 3mL of DCB at 130 °C. (b) 0.069g $PbBr_2$, 0.5 mL OA, 0.2 mL OLA, 1mL NMF, 50µL of precursor solution to 3mL of DCB at 100 °C, reaction time: 10 s.

As it is known from previous works, the growth of I-NCs is faster than that of Br- or Cl-based NCs[79]. The same trend was found here. For example, cubic-shaped $MAPbCl_3$ could be grown only by heating the bad solvent at 120 °C (Figure 6.2c), while in the case of $MAPbI_3$ NC, heating the bad solvent yielded bulk, non-emitting particles (Figure 6.6a). Even a RT synthesis (still using DCB as bad solvent) in this case led to a non-emitting sample formed by bulky nanowires (Figure 6.6b).

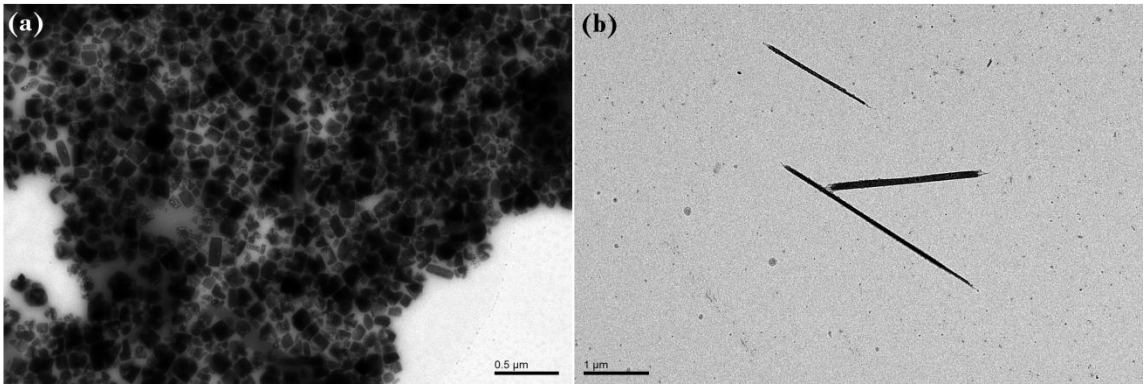

Figure 6.6: Effect of (a) heating the bad solvent, (b) using DCB as a bad solvent on $MAPbI_3$ NCs. Reaction condition: (A) 0.084g PbI_2, 0.5 mL OA, 0.2 mL OLA, 1mL NMF, 20µL of precursor solution to 5mL of $CHCl_3$ at 50 °C. (B) 0.084g PbI_2, 0.5 mL OA, 0.2 mL OLA, 1mL NMF, 20µL of precursor solution to 5mL of DCB at RT.

Instead, strongly fluorescent, cubic-shaped NCs could be grown using $CHCl_3$ as a bad solvent (Figure 6.2a). The rapid cooling of the flask after the injection was another crucial step in order to avoid the growth of large and poorly emitting NCs. For instance, in case of Br-NCs, increasing the reaction time up to 10 seconds led to NCs with lower PLQY (50% - see Figure 6.5b).

This synthetic route too could be easily scaled-up to a larger batch that yielded 0.4 L of $MAPbBr_3$ NC solution (Figure 6.7).

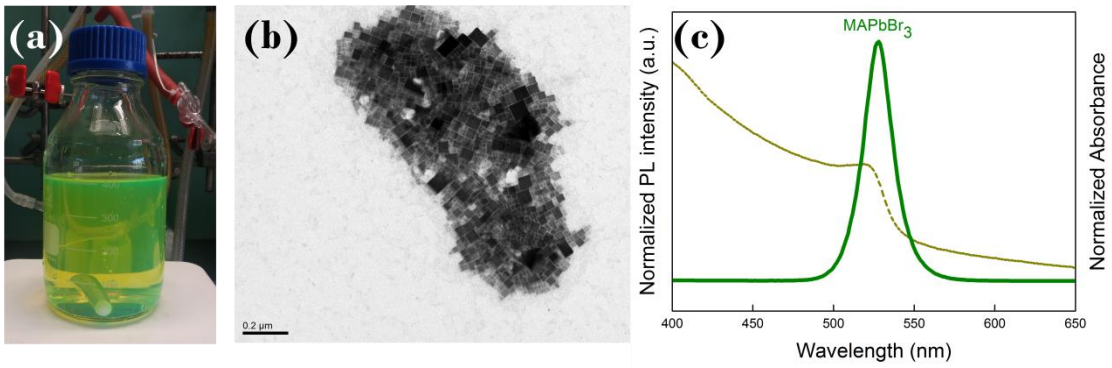

Figure 6.7: (a) Photographs of $MAPbBr_3$ NCs solution (b) TEM image and (c) optical properties of $MAPbBr_3$ NCs prepared by large-scale synthesis

Interestingly, by replacing NMF with NEF in our reaction medium, the transamidation reaction resulted ethyl ammonium-based layered perovskite (Figure 6.8), as previously reported in bulk scale[199]:

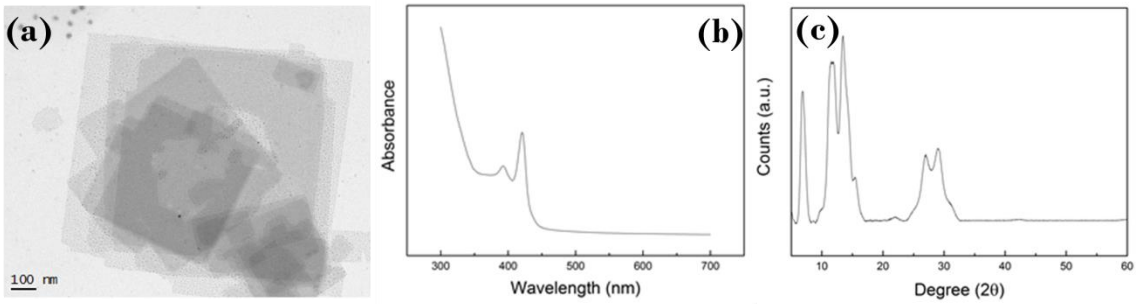

Figure 6.8: (a) TEM image, (b) absorbance spectrum and (c) XRD pattern of EA_xPbBr_y NSs

We then explored how the acid hydrolysis of NMF could act as a source of MA ions in the synthesis of bulk $MAPbX_3$ crystals. Bulk crystals of different halide perovskites were successfully grown within 12-48 hours at room temperature (RT), by a judicious choice of the Pb precursor concentration and the HX:NMF ratio, as shown in Scheme 6.1 and Table 6.1. Bulk Br-crystals (4 × 4 × 2 mm) with a relatively smooth surface (Figure 6.9) were formed with a $PbBr_2$ concentration range of 1 M to 0.8 M with a HBr:NMF volume ratio of 1:5.7. Crystals grown from 1 M $PbBr_2$ solution could reach 7 × 7 × 3 mm if kept in the solution for 4 weeks (Figure 6.9).

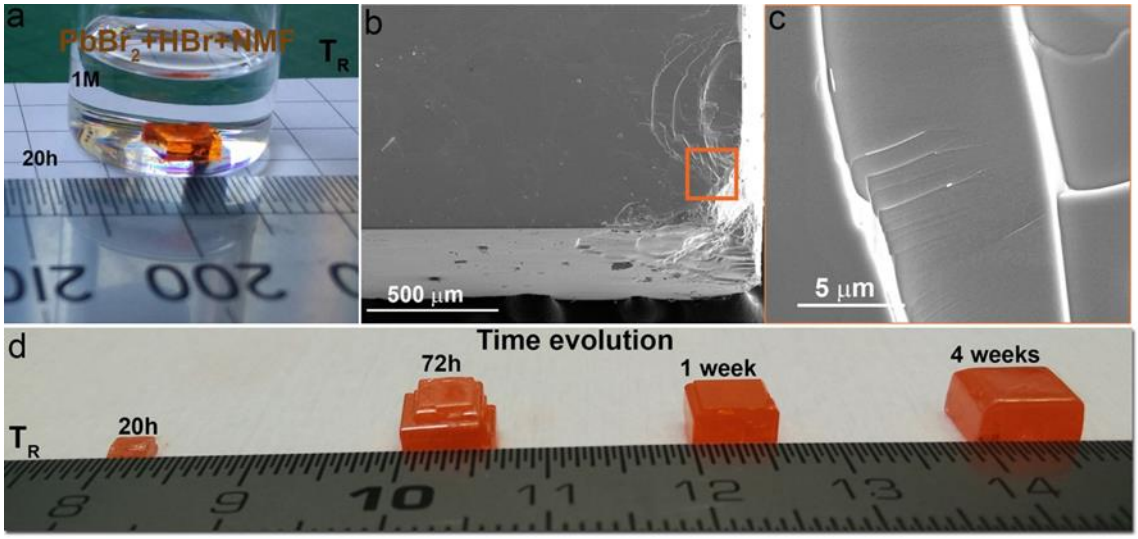

Figure 6.9: a) photograph of a representative bulk crystal of $MAPbBr_3$ ca. 3 × 3 × 1 mm formed when a mixture solution of 1 M $PbBr_2$ in HBr:NMF volume ratio of 1:5.7 is allowed to evolve for 20h at room temperature. b-c) HRSEM images of the crystal showing the flat and smooth surface obtained through this protocol. d) Size crystal evolution, from a side length of approx. 3 mm in less than a day to ca. 7 mm in a month time. The growth rate is notable higher at the beginning of the reaction (ca. 48 µm/h), particularly in the lateral directions and it slowly decrease with time (ca. 4 µm/h) due to the precursors consumption.

Lower concentrations did not produce any crystals even if left for several days. The crystallization speed could be increased if the process was carried out at temperatures higher than room temperature or by using higher HBr concentrations. In these cases, however, several aggregated crystals were formed (Figure 6.10).

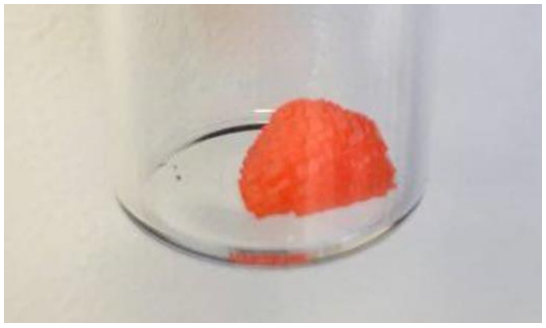

Figure 6.10: Aggregates of small $MAPbBr_3$ crystals synthesized at 60 °C

It is worth mentioning that bulk perovskites could also be grown using lead acetate or lead thiocyanate instead of lead bromide (Figure 6.11a).

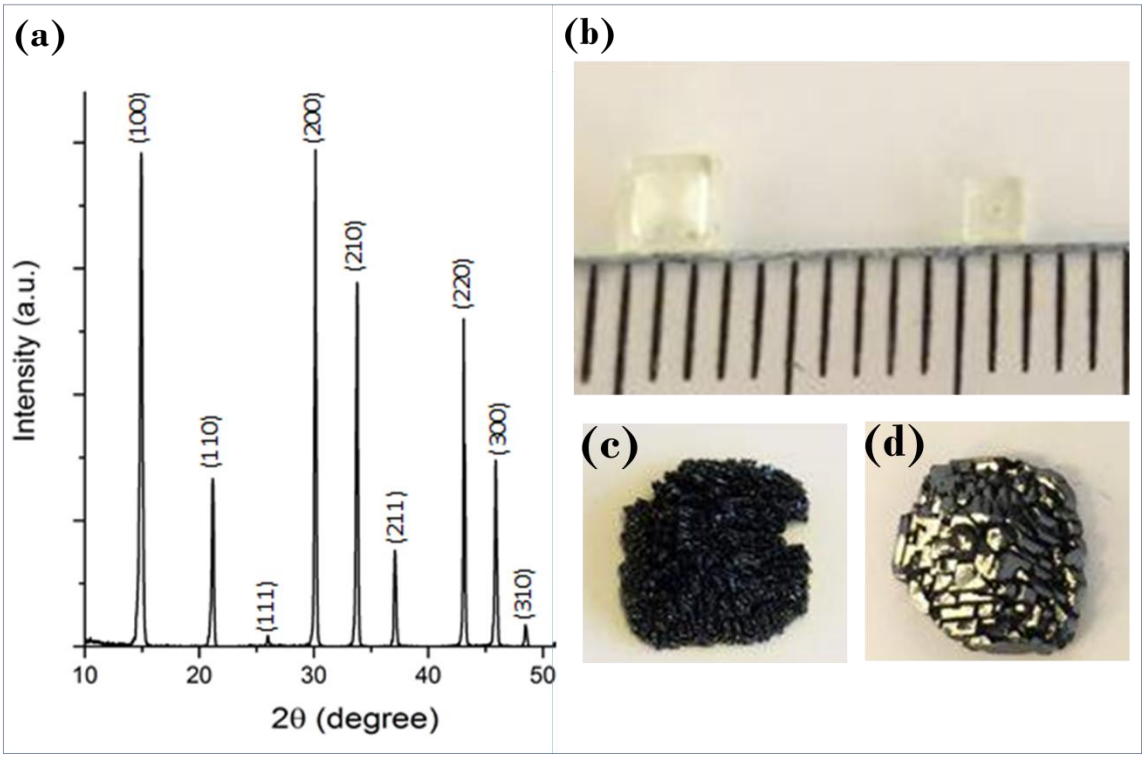

Figure 6.11: a) XRD pattern of $MAPbBr_3$ ground crystals synthesized from 1 M $Pb(SCN)_2$, with HBr:NMF volume ratio of 1:5.7. b) $MAPbCl_3$ bulky crystals synthesized using HCl:NMF 1:9 (left) and HCl:NMF 1:8 (right). c) Aggregate of $MAPbI_3$ crystals grown using 0.8 M PbI_2 (left) and 0.8 M $Pb(C_2H_3O_2)_2$ (right) and unstabilized HI with a volume ratio of HI:NMF of 10:1.

In the case of the Cl-crystals, a single nucleation in the crystallization vial was possible by lowering the concentration to 0.2 M with a HCl:NMF ratio of 1:9. The final crystals were about 3 × 3 × 2 mm large, but were not fully transparent. Smaller crystals (2 × 2 mm) with higher transparency could be formed at earlier stages of crystallization or by working at higher HCl content, but these conditions induced multiple nucleation events (Figure 6.11b).

Table 6.3: Bulk $MAPbX_3$ synthetic conditions

	Pb precursor concentration	HX	HX:NMF volume ratio
$MAPbCl_3$	0.2 M $PbCl_2$	37 w% aqueous HCl	1:9
$MAPbBr_3$	1 M $PbBr_2$	48 w% aqueous HBr	1:5.7
$MAPI_3$	0.8 M $Pb(Ac)_2$	57 w% aqueous HI, H_3PO_2 stabilized	10:1

On the other hand, the I-based perovskites could precipitate out of the HI/NMF solution mixture only if the NMF content was reduced below 20% of the total volume. In this process, NMF plays the dual role of solvent and of source of MAX. NMF, as a highly polar solvent, can bind strongly to the iodide precursors, hence the I-crystals are stable only at a lower NMF content. This appears to be in agreement with previous reports, according to which the less polar GBL, rather than the strongly polar DMF, is used for the crystallization of $MAPbI_3$.[174, 175]

The RT grown I- crystals using low NMF content (HI:NMF 10:1) were small and formed aggregates in the crystallization vial (Figure 6.11c). Aggregates made up of much larger $MAPbI_3$ crystals could be grown using lead acetate ($Pb(Ac)_2$) instead of PbI_2, (Figure 6.11c).

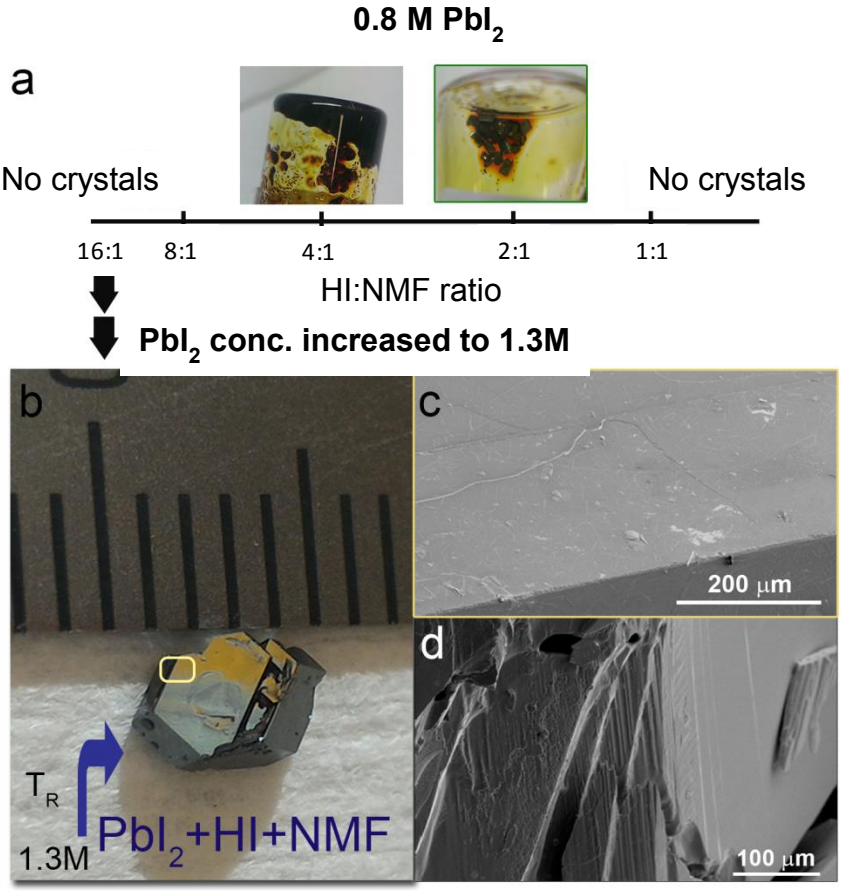

Figure 6.12: a) $MAPbI_3$ crystals using a 0.8 M PbI_2 solution, nucleated in a narrow range of HI:NMF ratio (between 4:1 and 2:1), exhibiting different sizes; excess of one of the components does not promote their formation (red crosses in the image). b) By increasing the PbI_2 content to 1.3 M with a higher HI:NMF ratio of 16:1 large crystals are formed after 48h. c,d) High resolution scanning electron microscopy (HRSEM) tilted view and cross-section of a bulk $MAPbI_3$ crystal showing the low surface roughness and the different cleavage planes denoting its classical brittle character.

This aggregation problem could be overcome by two different routes: either by using a concentrated (1.3 M) PbI_2 solution in a HI:NMF ratio of 16:1 (Figure 6.12) or by using stabilized HI (H_3PO_2-containing HI) (Figure 6.13).

Crystals prepared using stabilized HI had to be heated at ~ 60 °C for 30 minutes, after being removed from the crystallization dish, otherwise they turned yellow within few seconds. On the other hand, after the heating process they remained black for days. The free I_2 or the HI_3 present in the unstabilized HI may be the reason for the aggregation, as they may engage in halogen bonding with under-coordinated halide ions. As a result of this halogen bonding, a passivating layer could be formed on the surface of the $MAPbI_3$ crystals grown from unstabilized HI (I_3^-containing HI). Therefore, these $MAPbI_3$ crystals did not require post-heating treatment. Importantly, whether stabilized or unstabilized HI was used, the collected crystals had a smooth shiny surface.

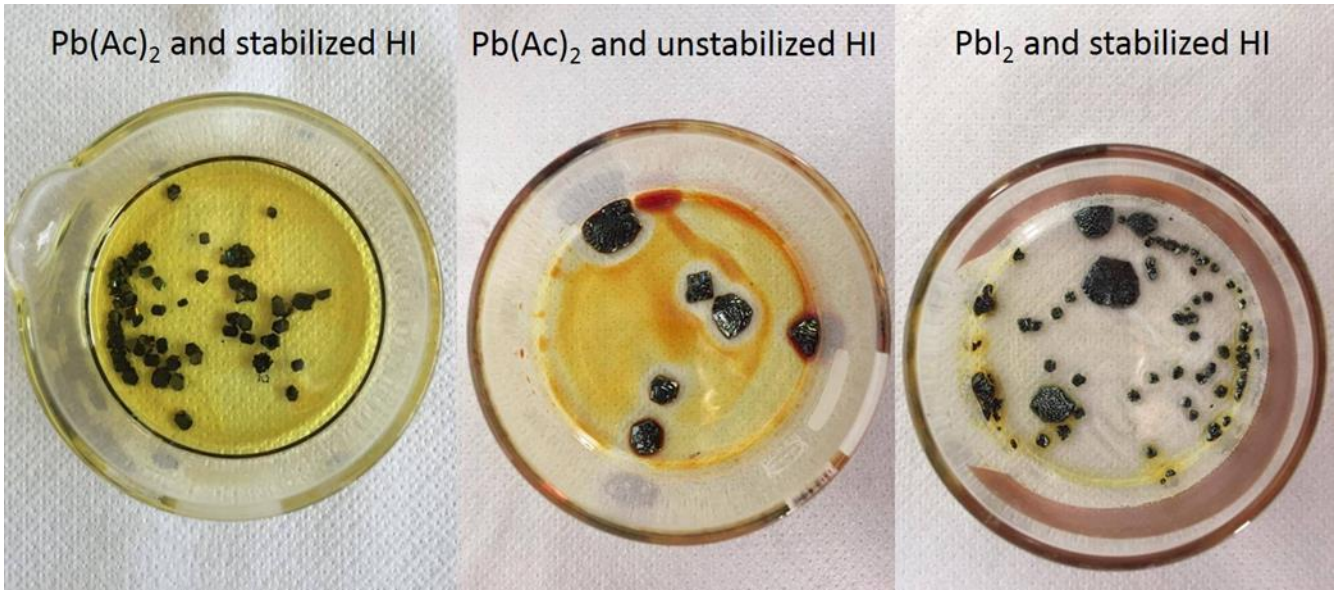

Figure 6.13: Bulk $MAPbI_3$ crystals grown using different precursors with HI:NMF volume ratio of 10:1. $Pb(Ac)_2$ and stabilized HI form more individual (less aggregated) $MAPbI_3$ bulk crystals.

According to the X-ray diffraction (XRD) patterns of ground crystals, their phases matched with those of the previously reported samples of the same materials, namely the cubic phase for $MAPbCl_3$[180] and $MAPbBr_3$,[174, 175] and the tetragonal phase for $MAPbI_3$[174, 175] (Figure 6.14a). The XRD pattern of the Cl- and Br-based as-grown crystals (Figure 6.15) produced diffraction peaks belonging mainly to the 001 family of planes, revealing their preferential surface termination.[200] The absorbance onset at 436 nm, 577 nm, and 853 nm for $MAPbCl_3$, $MAPbBr_3$, and $MAPbI_3$ respectively, were also in agreement with the reported best-quality single crystals (Figure 6.14b).[174, 175,180, 201]

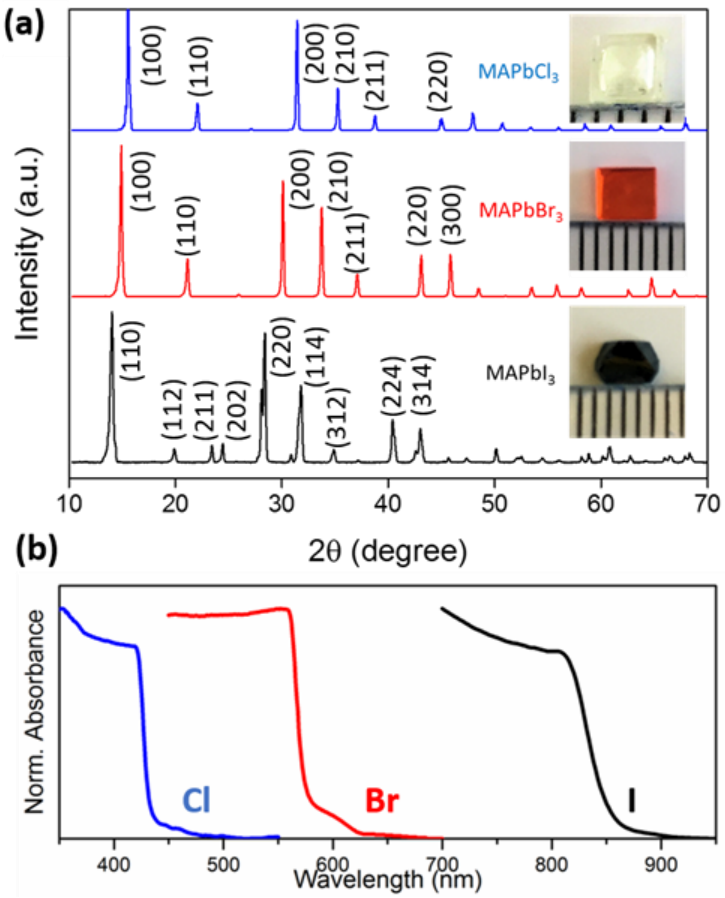

Figure 6.14: (a) Indexed XRD patterns of ground $MAPbX_3$ crystals. Inset: picture of the corresponding crystal and (b) absorbance spectra of $MAPbX_3$ crystals

The PL spectrum from bulk $MAPbBr_3$ crystals, collected using a commercial spectrophotometer, is in agreement with that of previous reports (Figure 6.16c).[174, 201]

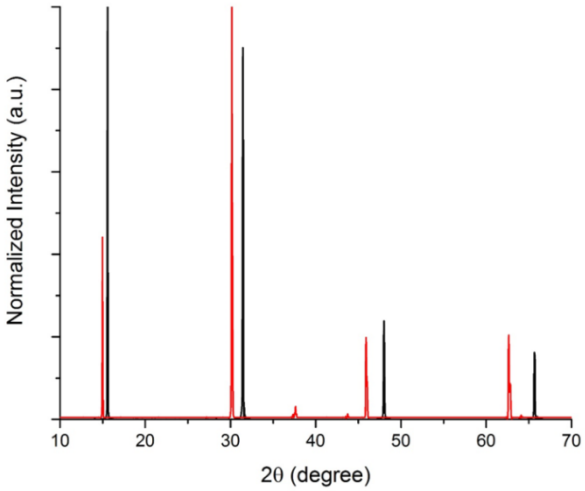

Figure 6.15: XRD patterns of $MAPbCl_3$ (black) and $MAPbBr_3$ (red) as-grown crystals. $MAPbCl_3$ crystal was grown from a 0.2 M $PbCl_2$ in a HCl:NMF volume ratio of 1:9. $MAPbBr_3$ crystal was grown from a 1 M $PbBr_2$ in a HBr:NMF volume ratio of 1:5.7.

On the other hand, when the PL was excited with one-photon laser excitation, which has a shallow penetration depth, it was blue shifted. For example, the PL spectra from the bromide and iodide bulk crystals were peaked at 550 nm and 780 nm, respectively (Figure 6.16a,b). Both values are blue shifted from the corresponding bulk values (580 nm for bromide crystal and 820 nm for the iodide crystal).[174, 201]

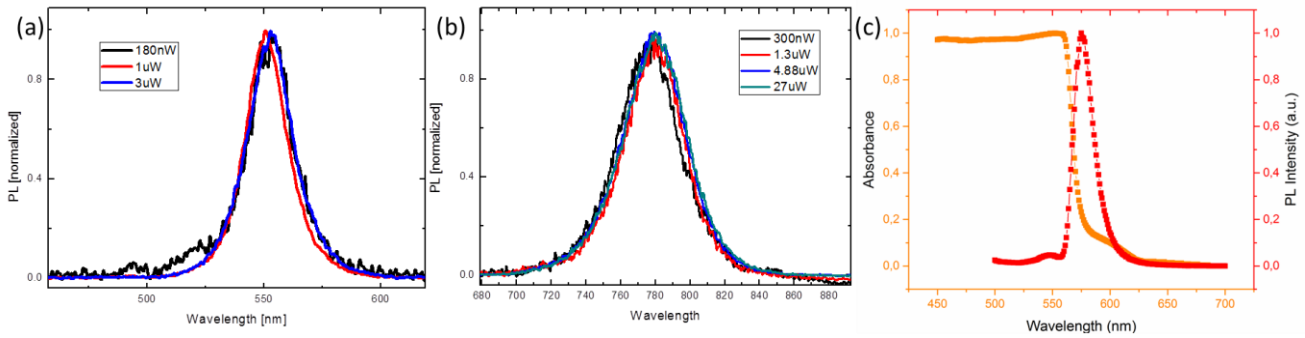

Figure 6.16: PL of (a) $MAPbBr_3$ (b) $MAPbI_3$ bulk crystal in air using one-photon laser excitation with different excitation powers. (c) Absorbance and PL of $MAPbBr_3$ crystal. PL obtained using a standard spectrophotometer.

In Figure 6.17 we show the time-resolved PL dynamics and spectra collected from bulk crystals of $MAPbI_3$ and $MAPbBr_3$. The excitation for both samples was tuned to 480 nm and the measurements were performed in ambient conditions. In the case of the iodide crystals, we observed an intensity dependent dynamics, with clear bimolecular recombination evident at high excitation densities. Similar dynamics have already been observed in other single crystals[175] and are indicative of efficient radiative recombination after the saturation of carrier traps.[202]

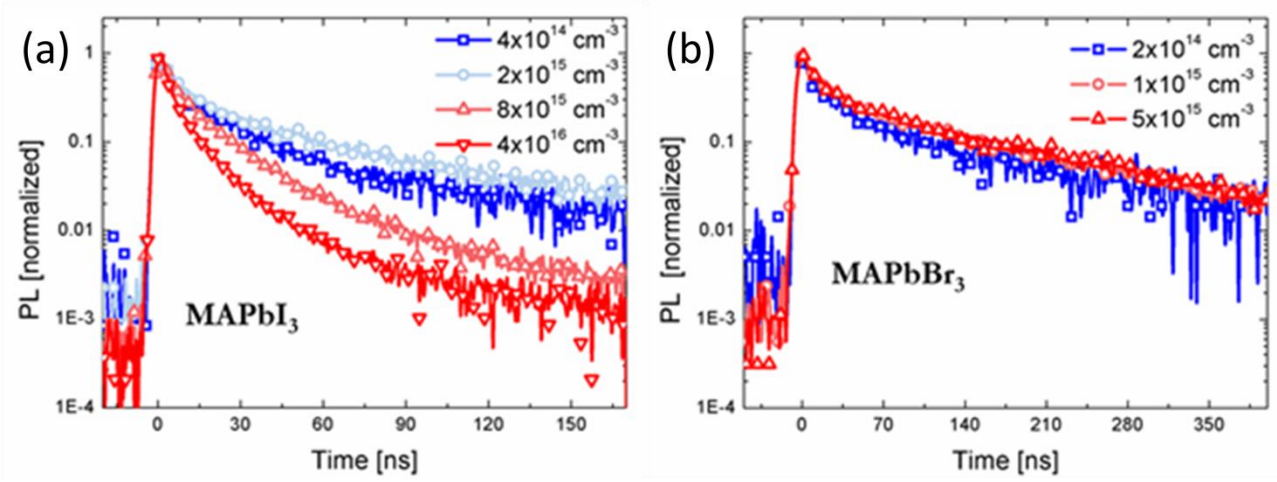

Figure 6.17: Time-resolved PL dynamics and spectra collected in ambient conditions from the single crystals of (a) $MAPbI_3$ and (b) $MAPbBr_3$. The excitation for both samples was tuned to 480 nm and dynamics are taken at excitation densities in the range between 10^{14} cm^{-3} and 10^{16} cm^{-3} as indicated in the figure legend.

The excitation density at which the bimolecular recombination becomes strongly evident qualitatively represents the available trap density. Following the density dependence shown in Figure 6.17, we

conclude that the trap density in these crystals is lower or around 10^{16} cm^{-3}. It must be noted that this value is lower than what is typically observed in polycrystalline thin films..[203] However, due to the limited penetration depth of the excitation, we were predominantly probing the dynamics at the crystals surface, which is inherently prone to higher density of defects with respect to the bulk. In fact, when the sample was kept at under vacuum, due to the absence of passivating oxygen,[204] we observed slower trap-limited dynamics due to enhanced defect density (Figure 6.18a). In the case of $MAPbBr_3$, on the other hand, we observe intensity independent dynamics at the probed excitation densities (Figure 6.17), suggesting that we were well within the trap-limited regime with higher density of defects than $MAPbI_3$. Here again, we observed a quenching of the lifetimes when the sample was kept under vacuum, due to the increase in the defect density (Figure 6.18b).

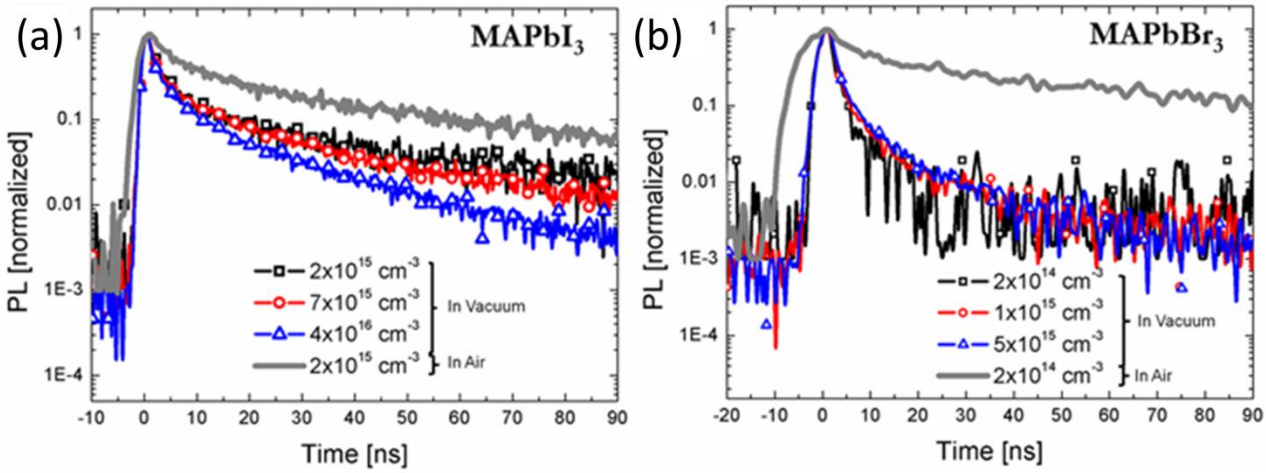

Figure 6.18: Time-resolved PL dynamics and spectra collected in vacuum from the single crystals of (a) $MAPbI_3$ and (b) $MAPbBr_3$. The excitation for both samples was tuned to 480 nm.

Very recently, $MAPbI_3$ crystals grown from an aqueous HI solution was reported to possess higher crystallinity and lower trap-state density compared to crystals grown from GBL solution.[192] Additionally, in hybrid perovskite thin films, it has been previously reported that an optimal amount of water assists the perovskite crystallization and leads to larger grain size.[205] In our process, the water content was adjusted indirectly by the proper choice of the HX:NMF ratio. Generally, water in the perovskite precursors solution may dissolve the organic cation but cannot dissolve the PbX_2 precursor, leading to a non-stoichiometric material. This is not the case in our crystals, as the XRD patterns showed no extra peaks corresponding to any PbX_2 salts. Another possible effect of the water content in our procedure is in regulating the rate of NMF hydrolysis, which is the vital step for the controlled release of MA.

The present NMF-assisted procedure could be also used to synthesize mixed halide perovskite bulk crystals, as indicated from the XRD pattern shift and the color of the crystals (Figure 6.19).

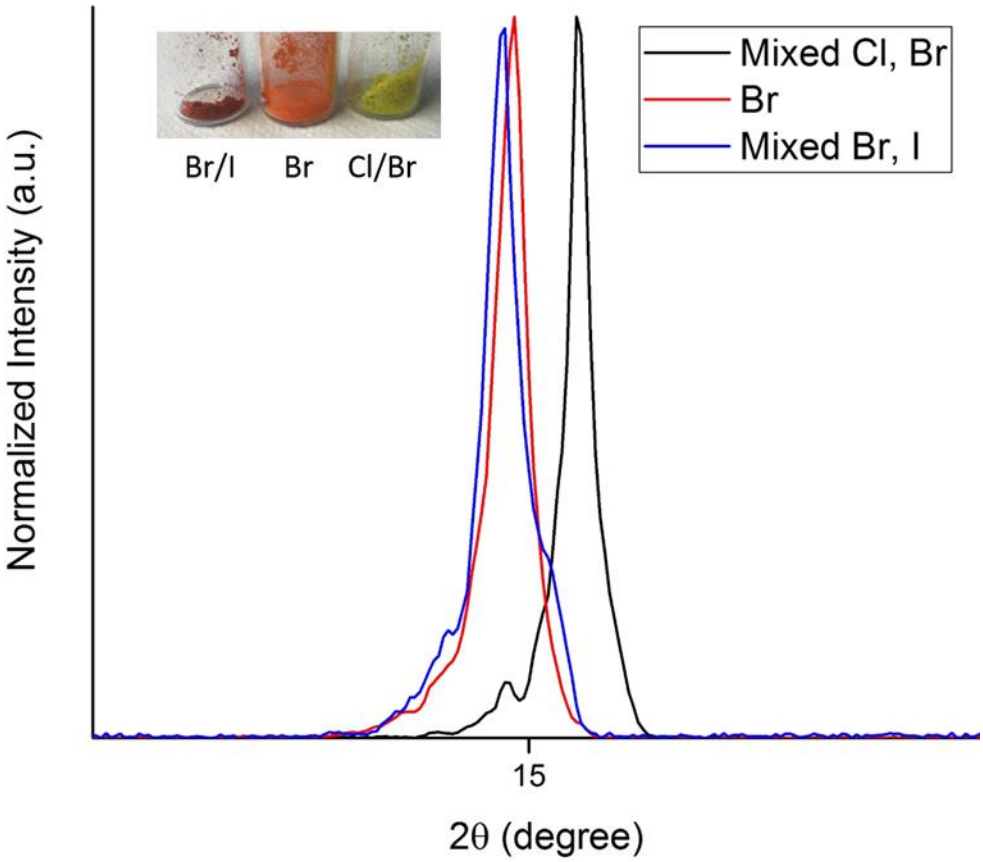

Figure 6.19: XRD patterns of pure $MAPbBr_3$, and mixed Cl/Br and Br/I of the ground crystals. Inset: photograph of corresponding ground crystals. Mixed Cl/Br crystal was synthesized using 1 M $PbBr_2$ and HCl:NMF volume ratio of 1:5.7. Mixed Br/I crystal was synthesized using 1 M $PbBr_2$ and HBr:NMF volume ratio of 1:5.7 followed by the addition of 250 µl of HI to 1 ml of the mentioned solution.

Mixed Cl/Br crystals were grown using $PbBr_2$ and HCl, while the mixed Br/I were formed using the same conditions for pure $MAPbBr_3$ bulk crystals (1M $PbBr_2$ in HBr:NMF, 1:5.7), followed by the addition of 250 µl of HI to a 1 ml of the bromide solution. The minor shift in case of the mixed Br/I could be attributed to the stronger complexation between Pb^{2+} and Br^- compared to Pb^{2+} and I^-.[206] When using $PbBr_2$ and HI, without any HBr added, pure $MAPbI_3$ crystals were formed. While single crystals represent the ideal form to investigate the materials properties, their large thickness limits their use in high-performance device applications.

To this end, as a proof of concept, we exploited such NMF procedure to fabricate planar-integrated single-crystal (ISC) perovskites-microcrystalline films made of interconnected micron-sized crystals (Figure 6.20), similar to what was previously reported to fabricate one of the best performing $MAPbBr_3$-based photodetectors[170]. By introducing some stirring force into the crystallization dish, microcrystalline films could be formed on both glass and ITO substrates.

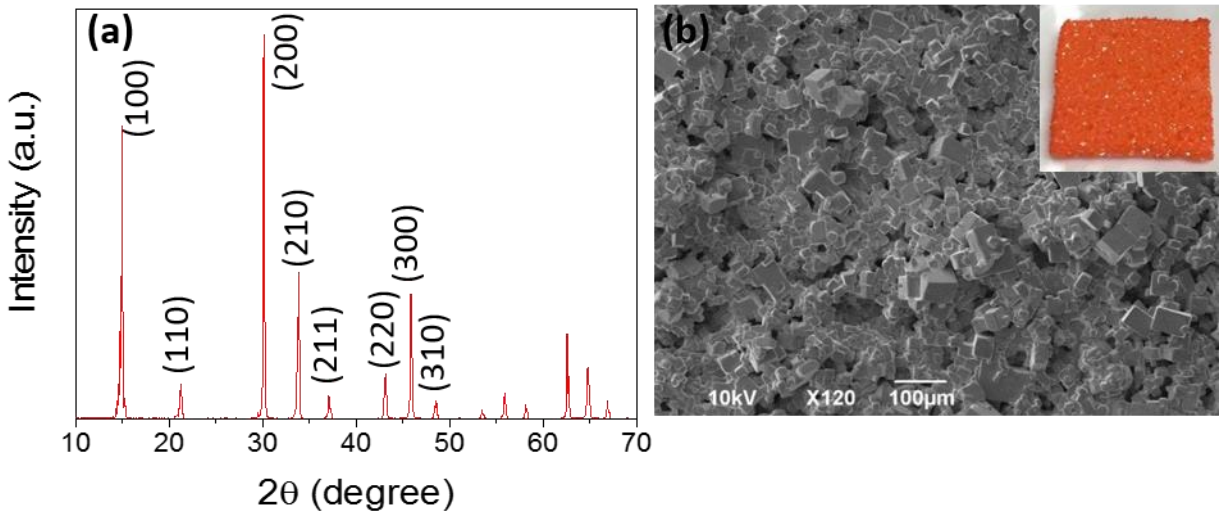

Figure 6.20: (a) XRD pattern and (b) SEM image of microcrystalline film of $MAPbBr_3$. Inset: picture of 1.5 × 1.5 cm film

6.4. Conclusion

In conclusion, we have developed a general and effective procedure for the synthesis of NCs and bulk crystals of $MAPbX_3$. This procedure takes advantage of the *in-situ* formation of MA *via* transamidation with alkylamine or acid-catalyzed hydrolysis of NMF, hence, reducing the amount of work, chemicals toxicity and cost required to realize high quality perovskites. Importantly, strongly fluorescent $MAPbX_3$ NCs (with record PLQY for the $MAPbI_3$ NCs – 60%) could be synthesized using NMF and OLA by a simple reprecipitation process, without the need of degassing any solvents. Moreover, only through this NMF-hydrolysis strategy, bulk crystals can be grown without heating and without any anti-solvent. In principle, with the method described here, MA ions can be released "on-demand" during a process, for example by increasing the acidity of the medium or by raising the local temperature, which might enable a better control on the fabrication of this important class of materials. These possibilities are currently being studied in our groups.

7. Conclusion and future prospects

7.1. Conclusion

In our quest for LHP-based optoelectronic applications, we carried out systematic experiments to discover and examine different synthetic chemistry methodologies of LHP NCs. We started off with the synthesis of the $CsPbBr_3$ NPLs by adding excess amount of oleic acid to the cesium precursors in the standard hot injection method. We found that the strong one dimensional confinement of the carriers at low thickness (~ 3nm) is responsible for the narrow PL, the strong excitonic absorption and the blue shift of the optical band gap of more than 0.47 eV compared to that of bulk $CsPbBr_3$.

We then elaborated this method by introducing short ligands to the reaction mixture in order to promote the lateral size of NPLs, resulting in large $CsPbBr_3$ NSs. We found that the impact of lateral size (in the 300nm – 5μm range) of such confined system on the PL is negligible.

Although the NPLs and NSs exhibited a narrow emission peak with unimodal distribution of thicknesses but the spin coating of as-prepared solution was mostly accompanied with the emergence of a green emission in thin films. In addition, the hot injection methods did not yield NPLs in quantities sufficient for their implementation in optoelectronic devices. These disadvantages motivated us to find an alternative technique to produce LHP NPLs.

Heat up method could address the large scale issue where we were able to synthesize ~ 7g NPLs which spontaneously self-assemble into stacked lamellar structures in solution. This unique structure enabled NPLs to preserve their pure blue emission even in solid state without the green impurity. Interesting, such blue emitting NPL films can transform to the stable green emitting films by exposure to UV light. This simple technique offers two promising advantages: 1) bright green emitting films with the PLQY of 65% 2) robust perovskite films under treatment with different solvents. We exploited these advantages of transformed films to fabricate all-solution-processed LED which displayed an external quantum efficiency of 1.1% and a luminance of 590 Cd/m^2.

We next focused on another challenge of hot injection method which is the fast nucleation and growth of LHP NCs. Thanks to the colloidal precursors, we developed an indirect approach to grow LHP domains. We synthesized CsX NCs as colloidal seeds which can be (partially or fully) transformed to $CsPbX_3$ NCs at room temperature. We showed that the transformation of CsBr to $CsPbBr_3$ goes through core/shell $CsBr/CsPbBr_3$ nanocrystals as intermediate structures. Although this novel route enabled us to produce different size of monodisperse $CsPbBr_3$ NCs at room temperature, but the size of confined

domain was not precisely controllable in the intermediate stage and this part need to be further investigated.

Finally, we reported a novel feature of LARP method in which the good solvent (NMF) can *in-situ* release the A-site cation (MA^+) into the reaction mixture. Compared with the standard LARP, we achieved a better control over the size and shape of $MAPbX_3$ NCs. The nanocrystals showed photoluminescence quantum yields reaching 74% for $MAPbBr_3$ and 60% for $MAPbI_3$. Our method proceeds without firstly synthesizing and purifying MAX, as well as avoiding the procurement of the expensive MA salts and eliminating the use of toxic DMF. Interestingly, we showed that such a solvent can also be used to grow LHP bulk crystals at room temperature.

7.2. Perspectives

Future research should bridge the gap between the synthesis and the application of the LHP NCs. This gap is *LHP NC thin films*. Many researchers neglect the behavior of LHP NCs in solid state where optical and structural properties are influenced by deposition. In this respect, solid-state ligand exchange should be investigated and this could possibly improve the stability of LHP NC thin films.

The fabrication of bright blue emitting thin film remains undeveloped for all-solution-processed applications. Although we have reported the optically stable blue emitting film but the as-prepared film was not stable with respect to the solvents (e.g. toluene). As the Cl/Br mixed halide perovskites do not exhibit strong PL at room temperature and they also suffer from the color instability due to the halide segregation, the quantum confined Br-based NCs are still promising candidate for pure blue emitting devices.

In this final section, I would like to state my personal opinion, concerning the future advancement of LHP NCs. I have to confess that the instability of LHP NC blurs the future of such material for optoelectronic applications. Although many groups have reported some tricks in order to improve the stability of LHP NCs in solution, such as using “different surface ligands” or “dopants” but LHP NCs degrade very fast under high voltage. We might modify the surface of LHP NCs, but we cannot change the nature of such materials. LHP NCs are soft and chemically unstable substances with respect to light, temperature and the environment. There is an urgent need to introduce a proper shell for LHP NCs in order to isolate them from the environment. However, this structure will just allow us to study and

understand the optical and structural properties of perovskites as core and will not guarantee the stability of LHP NCs.

The biggest remaining question is that *shall we keep trying to discover more and make them stable or is it time to work on a new material?*

Bibliography

1. Gallinet, B.; Butet, J.; Martin, O. J. F., Numerical methods for nanophotonics: standard problems and future challenges. *Laser & Photonics Reviews* 2015, 9, 577-603.
2. Dietrich, C. P.; Fiore, A.; Thompson, M. G.; Kamp, M.; Höfling, S., GaAs integrated quantum photonics: Towards compact and multi-functional quantum photonic integrated circuits (Laser Photonics Rev. 10(6)/2016). *Laser & Photonics Reviews* 2016, 10, 857-857.
3. Polavarapu, L.; Nickel, B.; Feldmann, J.; Urban, A. S., Advances in Quantum-Confined Perovskite Nanocrystals for Optoelectronics. *Advanced Energy Materials* 2017, 1700267.
4. Manser, J. S.; Christians, J. A.; Kamat, P. V., Intriguing Optoelectronic Properties of Metal Halide Perovskites. *Chemical reviews* 2016, 116, 12956-13008.
5. Smith, A. M.; Nie, S., Semiconductor Nanocrystals: Structure, Properties, and Band Gap Engineering. *Accounts of chemical research* 2010, 43, 190-200.
6. Liang, J.; Liu, J.; Jin, Z., All-Inorganic Halide Perovskites for Optoelectronics: Progress and Prospects. *Solar Rrl* 2017, 1, 1700086-n/a.
7. Shim, J.; Park, H. Y.; Kang, D. H.; Kim, J. O.; Jo, S. H.; Park, Y.; Park, J. H., Electronic and Optoelectronic Devices based on Two-Dimensional Materials: From Fabrication to Application. *Advanced Electronic Materials* 2017, 3, 1600364-n/a.
8. Tudor, J., A brief history of ... semiconductors. *Physics Education* 2005, 40, 430.
9. Wilson, A. H., The Theory of Electronic Semi-Conductors. *Proceedings of the Royal Society A: Mathematical, Physical and Engineering Sciences* 1931, 133, 458-491.
10. Jaffé, G., Theory of Conductivity of Semiconductors. *Physical Review* 1952, 85, 354-363.
11. Sivula, K.; van de Krol, R., Semiconducting materials for photoelectrochemical energy conversion. *Nature Reviews Materials* 2016, 1, 15010.
12. Sze, S. M.; Ng, K. K., Physics and Properties of Semiconductors—A Review. In *Physics of Semiconductor Devices*, John Wiley & Sons, Inc.: 2006; pp 5-75.
13. Stoumpos, C. C.; Kanatzidis, M. G., Halide Perovskites: Poor Man's High-Performance Semiconductors. *Advanced materials* 2016, 28, 5778-93.
14. Petrus, M. L.; Schlipf, J.; Li, C.; Gujar, T. P.; Giesbrecht, N.; Müller-Buschbaum, P.; Thelakkat, M.; Bein, T.; Hüttner, S.; Docampo, P., Capturing the Sun: A Review of the Challenges and Perspectives of Perovskite Solar Cells. *Advanced Energy Materials* 2017, 7, 1700264.
15. Saparov, B.; Mitzi, D. B., Organic-Inorganic Perovskites: Structural Versatility for Functional Materials Design. *Chemical reviews* 2016, 116, 4558-96.
16. Zhao, Y.; Zhu, K., Organic-inorganic hybrid lead halide perovskites for optoelectronic and electronic applications. *Chemical Society reviews* 2016, 45, 655-89.
17. Gao, P.; Grätzel, M.; Nazeeruddin, M. K., Organohalide lead perovskites for photovoltaic applications. *Energy Environ. Sci.* 2014, 7, 2448-2463.
18. Amgar, D.; Aharon, S.; Etgar, L., Inorganic and Hybrid Organo-Metal Perovskite Nanostructures: Synthesis, Properties, and Applications. *Advanced Functional Materials* 2016, 26, 8576-8593.
19. Li, X.; Cao, F.; Yu, D.; Chen, J.; Sun, Z.; Shen, Y.; Zhu, Y.; Wang, L.; Wei, Y.; Wu, Y.; Zeng, H., All Inorganic Halide Perovskites Nanosystem: Synthesis, Structural Features, Optical Properties and Optoelectronic Applications. *Small* 2017, 13.
20. Wang, Y.; Sun, H., All-Inorganic Metal Halide Perovskite Nanostructures: From Photophysics to Light-Emitting Applications. *Small Methods* 2017, 1700252.
21. Kovalenko, M. V.; Bodnarchuk, M. I., Lead Halide Perovskite Nanocrystals: From Discovery to Self-assembly and Applications. *Chimia* 2017, 71, 461-470.
22. Sutherland, B. R.; Sargent, E. H., Perovskite photonic sources. *Nature Photonics* 2016, 10, 295-302.

23. Travis, W.; Glover, E. N. K.; Bronstein, H.; Scanlon, D. O.; Palgrave, R. G., On the application of the tolerance factor to inorganic and hybrid halide perovskites: a revised system. *Chem. Sci.* 2016, 7, 4548-4556.
24. Kovalenko, M. V.; Protesescu, L.; Bodnarchuk, M. I., Properties and potential optoelectronic applications of lead halide perovskite nanocrystals. *Science* 2017, 358, 745-750.
25. Li, C.; Lu, X.; Ding, W.; Feng, L.; Gao, Y.; Guo, Z., Formability of ABX3 (X = F, Cl, Br, I) halide perovskites. *Acta crystallographica. Section B, Structural science* 2008, 64, 702-7.
26. MØLler, C. K., Crystal Structure and Photoconductivity of Cæsium Plumbohalides. *Nature* 1958, 182, 1436.
27. Kojima, A.; Teshima, K.; Shirai, Y.; Miyasaka, T., Organometal halide perovskites as visible-light sensitizers for photovoltaic cells. *Journal of the American Chemical Society* 2009, 131, 6050-1.
28. Kieslich, G.; Sun, S.; Cheetham, A. K., Solid-state principles applied to organic–inorganic perovskites: new tricks for an old dog. *Chem. Sci.* 2014, 5, 4712-4715.
29. Liu, X.; Zhao, W.; Cui, H.; Xie, Y. a.; Wang, Y.; Xu, T.; Huang, F., Organic–inorganic halide perovskite based solar cells – revolutionary progress in photovoltaics. *Inorg. Chem. Front.* 2015, 2, 315-335.
30. Luo, S.; Daoud, W. A., Recent progress in organic–inorganic halide perovskite solar cells: mechanisms and material design. *J. Mater. Chem. A* 2015, 3, 8992-9010.
31. Berhe, T. A.; Su, W.-N.; Chen, C.-H.; Pan, C.-J.; Cheng, J.-H.; Chen, H.-M.; Tsai, M.-C.; Chen, L.-Y.; Dubale, A. A.; Hwang, B.-J., Organometal halide perovskite solar cells: degradation and stability. *Energy Environ. Sci.* 2016, 9, 323-356.
32. Ganose, A. M.; Savory, C. N.; Scanlon, D. O., Beyond methylammonium lead iodide: prospects for the emergent field of ns2 containing solar absorbers. *Chemical communications* 2016, 53, 20-44.
33. Kang, J.; Wang, L. W., High Defect Tolerance in Lead Halide Perovskite CsPbBr3. *The journal of physical chemistry letters* 2017, 8, 489-493.
34. Eperon, G. E.; Stranks, S. D.; Menelaou, C.; Johnston, M. B.; Herz, L. M.; Snaith, H. J., Formamidinium lead trihalide: a broadly tunable perovskite for efficient planar heterojunction solar cells. *Energ Environ Sci* 2014, 7, 982.
35. Li, G.; Ho, J. Y.-L.; Wong, M.; Kwok, H. S., Reversible Anion Exchange Reaction in Solid Halide Perovskites and Its Implication in Photovoltaics. *The Journal of Physical Chemistry C* 2015, 119, 26883-26888.
36. Noh, J. H.; Im, S. H.; Heo, J. H.; Mandal, T. N.; Seok, S. I., Chemical management for colorful, efficient, and stable inorganic-organic hybrid nanostructured solar cells. *Nano letters* 2013, 13, 1764-9.
37. Ball, J. M.; Petrozza, A., Defects in perovskite-halides and their effects in solar cells. *Nature Energy* 2016, 1, 16149.
38. Whalley, L. D.; Crespo-Otero, R.; Walsh, A., H-Center and V-Center Defects in Hybrid Halide Perovskites. *ACS Energy Letters* 2017, 2, 2713-2714.
39. Manser, J. S.; Saidaminov, M. I.; Christians, J. A.; Bakr, O. M.; Kamat, P. V., Making and Breaking of Lead Halide Perovskites. *Accounts of chemical research* 2016, 49, 330-8.
40. Chen, Y.; He, M.; Peng, J.; Sun, Y.; Liang, Z., Structure and Growth Control of Organic–Inorganic Halide Perovskites for Optoelectronics: From Polycrystalline Films to Single Crystals. *Advanced Science* 2016, 3, 1500392-n/a.
41. Shi, D.; Adinolfi, V.; Comin, R.; Yuan, M.; Alarousu, E.; Buin, A.; Chen, Y.; Hoogland, S.; Rothenberger, A.; Katsiev, K.; Losovyj, Y.; Zhang, X.; Dowben, P. A.; Mohammed, O. F.; Sargent, E. H.; Bakr, O. M., Solar cells. Low trap-state density and long carrier diffusion in organolead trihalide perovskite single crystals. *Science* 2015, 347, 519-22.
42. Dong, Q.; Fang, Y.; Shao, Y.; Mulligan, P.; Qiu, J.; Cao, L.; Huang, J., Electron-hole diffusion lengths > 175 μm in solution-grown CH₃NH₃PbI₃ single crystals. *Science* 2015, 347, 967-970.
43. Dang, Y.; Ju, D.; Wang, L.; Tao, X., Recent progress in the synthesis of hybrid halide perovskite single crystals. *CrystEngComm* 2016, 18, 4476-4484.
44. Dong, Q.; Fang, Y.; Shao, Y.; Mulligan, P.; Qiu, J.; Cao, L.; Huang, J., Solar cells. Electron-hole diffusion lengths > 175 mum in solution-grown CH3NH3PbI3 single crystals. *Science* 2015, 347, 967-70.

45. Dong, Q.; Song, J.; Fang, Y.; Shao, Y.; Ducharme, S.; Huang, J., Lateral-Structure Single-Crystal Hybrid Perovskite Solar Cells via Piezoelectric Poling. *Advanced Materials* 2016, 28, 2816-2821.
46. Peng, W.; Wang, L.; Murali, B.; Ho, K. T.; Bera, A.; Cho, N.; Kang, C. F.; Burlakov, V. M.; Pan, J.; Sinatra, L.; Ma, C.; Xu, W.; Shi, D.; Alarousu, E.; Goriely, A.; He, J. H.; Mohammed, O. F.; Wu, T.; Bakr, O. M., Solution-Grown Monocrystalline Hybrid Perovskite Films for Hole-Transporter-Free Solar Cells. *Adv Mater* 2016, 28, 3383-90.
47. Maculan, G.; Sheikh, A. D.; Abdelhady, A. L.; Saidaminov, M. I.; Haque, M. A.; Murali, B.; Alarousu, E.; Mohammed, O. F.; Wu, T.; Bakr, O. M., CH3NH3PbCl3 Single Crystals: Inverse Temperature Crystallization and Visible-Blind UV-Photodetector. *J Phys Chem Lett* 2015, 6, 3781-6.
48. Fang, Y.; Dong, Q.; Shao, Y.; Yuan, Y.; Huang, J., Highly narrowband perovskite single-crystal photodetectors enabled by surface-charge recombination. *Nature Photonics* 2015, 9, 679-686.
49. Shaikh, P. A.; Shi, D.; Retamal, J. R. D.; Sheikh, A. D.; Haque, M. A.; Kang, C.-F.; He, J.-H.; Bakr, O. M.; Wu, T., Schottky junctions on perovskite single crystals: light-modulated dielectric constant and self-biased photodetection. *Journal of Materials Chemistry C* 2016, 4, 8304-8312.
50. Cao, M.; Tian, J.; Cai, Z.; Peng, L.; Yang, L.; Wei, D., Perovskite heterojunction based on CH3NH3PbBr3 single crystal for high-sensitive self-powered photodetector. *Applied Physics Letters* 2016, 109, 233303.
51. Yakunin, S.; Dirin, D. N.; Shynkarenko, Y.; Morad, V.; Cherniukh, I.; Nazarenko, O.; Kreil, D.; Nauser, T.; Kovalenko, M. V., Detection of gamma photons using solution-grown single crystals of hybrid lead halide perovskites. *Nature Photonics* 2016.
52. Cha, J.-H.; Han, J. H.; Yin, W.; Park, C.; Park, Y.; Ahn, T. K.; Cho, J. H.; Jung, D.-Y., Photoresponse of CsPbBr3 and Cs4PbBr6 Perovskite Single Crystals. *The Journal of Physical Chemistry Letters* 2017, 565-570.
53. Rao, H.-S.; Li, W.-G.; Chen, B.-X.; Kuang, D.-B.; Su, C.-Y., In Situ Growth of 120 cm2 CH3NH3PbBr3 Perovskite Crystal Film on FTO Glass for Narrowband-Photodetectors. *Advanced Materials* 2017, 1602639-n/a.
54. Wei, H.; Fang, Y.; Mulligan, P.; Chuirazzi, W.; Fang, H.-H.; Wang, C.; Ecker, B. R.; Gao, Y.; Loi, M. A.; Cao, L.; Huang, J., Sensitive X-ray detectors made of methylammonium lead tribromide perovskite single crystals. *Nat Photon* 2016, 10, 333-339.
55. Saidaminov, M. I.; Haque, M. A.; Almutlaq, J.; Sarmah, S.; Miao, X.-H.; Begum, R.; Zhumekenov, A. A.; Dursun, I.; Cho, N.; Murali, B.; Mohammed, O. F.; Wu, T.; Bakr, O. M., Inorganic Lead Halide Perovskite Single Crystals: Phase-Selective Low-Temperature Growth, Carrier Transport Properties, and Self-Powered Photodetection. *Advanced Optical Materials* 2016, 1600704-n/a.
56. Saidaminov, M. I.; Abdelhady, A. L.; Murali, B.; Alarousu, E.; Burlakov, V. M.; Peng, W.; Dursun, I.; Wang, L.; He, Y.; Maculan, G.; Goriely, A.; Wu, T.; Mohammed, O. F.; Bakr, O. M., High-quality bulk hybrid perovskite single crystals within minutes by inverse temperature crystallization. *Nat Commun* 2015, 6, 7586.
57. Liu, Y.; Yang, Z.; Cui, D.; Ren, X.; Sun, J.; Liu, X.; Zhang, J.; Wei, Q.; Fan, H.; Yu, F.; Zhang, X.; Zhao, C.; Liu, S. F., Two-Inch-Sized Perovskite CH3 NH3 PbX3 (X = Cl, Br, I) Crystals: Growth and Characterization. *Adv Mater* 2015, 27, 5176-83.
58. Lian, Z.; Yan, Q.; Gao, T.; Ding, J.; Lv, Q.; Ning, C.; Li, Q.; Sun, J. L., Perovskite CH3NH3PbI3(Cl) Single Crystals: Rapid Solution Growth, Unparalleled Crystalline Quality, and Low Trap Density toward 10(8) cm(-3). *Journal of the American Chemical Society* 2016, 138, 9409-12.
59. Saidaminov, M. I.; Adinolfi, V.; Comin, R.; Abdelhady, A. L.; Peng, W.; Dursun, I.; Yuan, M.; Hoogland, S.; Sargent, E. H.; Bakr, O. M., Planar-integrated single-crystalline perovskite photodetectors. *Nat Commun* 2015, 6, 8724.
60. Murali, B.; Yengel, E.; Yang, C.; Peng, W.; Alarousu, E.; Bakr, O. M.; Mohammed, O. F., The Surface of Hybrid Perovskite Crystals: A Boon or Bane. *ACS Energy Letters* 2017.
61. Murali, B.; Dey, S.; Abdelhady, A. L.; Peng, W.; Alarousu, E.; Kirmani, A. R.; Cho, N.; Sarmah, S. P.; Parida, M. R.; Saidaminov, M. I.; Zhumekenov, A. A.; Sun, J.; Alias, M. S.; Yengel, E.; Ooi, B. S.; Amassian, A.; Bakr, O. M.; Mohammed, O. F., Surface Restructuring of Hybrid Perovskite Crystals. *ACS Energy Letters* 2016, 1119-1126.
62. Wu, B.; Nguyen, H. T.; Ku, Z.; Han, G.; Giovanni, D.; Mathews, N.; Fan, H. J.; Sum, T. C., Discerning the Surface and Bulk Recombination Kinetics of Organic-Inorganic Halide Perovskite Single Crystals. *Advanced Energy Materials* 2016, 6, 1600551.

63. Grancini, G.; D'Innocenzo, V.; Dohner, E. R.; Martino, N.; Srimath Kandada, A. R.; Mosconi, E.; De Angelis, F.; Karunadasa, H. I.; Hoke, E. T.; Petrozza, A., CH3NH3PbI3perovskite single crystals: surface photophysics and their interaction with the environment. *Chem. Sci.* 2015, 6, 7305-7310.
64. Abate, A.; Saliba, M.; Hollman, D. J.; Stranks, S. D.; Wojciechowski, K.; Avolio, R.; Grancini, G.; Petrozza, A.; Snaith, H. J., Supramolecular Halogen Bond Passivation of Organic–Inorganic Halide Perovskite Solar Cells. *Nano Letters* 2014, 14, 3247-3254.
65. Noel, N. K.; Abate, A.; Stranks, S. D.; Parrott, E. S.; Burlakov, V. M.; Goriely, A.; Snaith, H. J., Enhanced Photoluminescence and Solar Cell Performance via Lewis Base Passivation of Organic–Inorganic Lead Halide Perovskites. *ACS nano* 2014, 8, 9815-9821.
66. deQuilettes, D. W.; Koch, S.; Burke, S.; Paranji, R. K.; Shropshire, A. J.; Ziffer, M. E.; Ginger, D. S., Photoluminescence Lifetimes Exceeding 8 μs and Quantum Yields Exceeding 30% in Hybrid Perovskite Thin Films by Ligand Passivation. *ACS Energy Letters* 2016, 1, 438-444.
67. Gao, L.; Zeng, K.; Guo, J.; Ge, C.; Du, J.; Zhao, Y.; Chen, C.; Deng, H.; He, Y.; Song, H.; Niu, G.; Tang, J., Passivated Single-Crystalline CH3NH3PbI3 Nanowire Photodetector with High Detectivity and Polarization Sensitivity. *Nano Letters* 2016.
68. Son, D.-Y.; Lee, J.-W.; Choi, Y. J.; Jang, I.-H.; Lee, S.; Yoo, P. J.; Shin, H.; Ahn, N.; Choi, M.; Kim, D.; Park, N.-G., Self-formed grain boundary healing layer for highly efficient CH3 NH3 PbI3 perovskite solar cells. *Nature Energy* 2016, 1, 16081.
69. Aristidou, N.; Eames, C.; Sanchez-Molina, I.; Bu, X.; Kosco, J.; Islam, M. S.; Haque, S. A., Fast oxygen diffusion and iodide defects mediate oxygen-induced degradation of perovskite solar cells. *Nature Communications* 2017, 8, 15218.
70. Dirin, D. N.; Cherniukh, I.; Yakunin, S.; Shynkarenko, Y.; Kovalenko, M. V., Solution-Grown CsPbBr3 Perovskite Single Crystals for Photon Detection. *Chemistry of Materials* 2016, 28, 8470-8474.
71. Saidaminov, M. I.; Abdelhady, A. L.; Murali, B.; Alarousu, E.; Burlakov, V. M.; Peng, W.; Dursun, I.; Wang, L.; He, Y.; Maculan, G.; Goriely, A.; Wu, T.; Mohammed, O. F.; Bakr, O. M., High-quality bulk hybrid perovskite single crystals within minutes by inverse temperature crystallization. *Nature communications* 2015, 6, 7586.
72. Owen, J.; Brus, L., Chemical Synthesis and Luminescence Applications of Colloidal Semiconductor Quantum Dots. *Journal of the American Chemical Society* 2017.
73. Carey, G. H.; Abdelhady, A. L.; Ning, Z.; Thon, S. M.; Bakr, O. M.; Sargent, E. H., Colloidal Quantum Dot Solar Cells. *Chemical reviews* 2015, 115, 12732-63.
74. de Mello Donega, C., Synthesis and properties of colloidal heteronanocrystals. *Chemical Society reviews* 2011, 40, 1512-46.
75. Im, J. H.; Lee, C. R.; Lee, J. W.; Park, S. W.; Park, N. G., 6.5% efficient perovskite quantum-dot-sensitized solar cell. *Nanoscale* 2011, 3, 4088-93.
76. Kojima, A.; Ikegami, M.; Teshima, K.; Miyasaka, T., Highly Luminescent Lead Bromide Perovskite Nanoparticles Synthesized with Porous Alumina Media. *Chemistry Letters* 2012, 41, 397-399.
77. Schmidt, L. C.; Pertegas, A.; Gonzalez-Carrero, S.; Malinkiewicz, O.; Agouram, S.; Minguez Espallargas, G.; Bolink, H. J.; Galian, R. E.; Perez-Prieto, J., Nontemplate synthesis of CH3NH3PbBr3 perovskite nanoparticles. *Journal of the American Chemical Society* 2014, 136, 850-3.
78. Nikl, M.; Nitsch, K.; Polák, K.; Mihókova, E.; Zazubovich, S.; Pazzi, G. P.; Fabeni, P.; Salvini, L.; Aceves, R.; Barbosa-Flores, M.; Salas, R. P.; Gurioli, M.; Scacco, A., Quantum size effect in the excitonic luminescence of CsPbX3-like quantum dots in CsX (X = Cl, Br) single crystal host. *Journal of Luminescence* 1997, 72-74, 377-379.
79. Protesescu, L.; Yakunin, S.; Bodnarchuk, M. I.; Krieg, F.; Caputo, R.; Hendon, C. H.; Yang, R. X.; Walsh, A.; Kovalenko, M. V., Nanocrystals of Cesium Lead Halide Perovskites (CsPbX(3), X = Cl, Br, and I): Novel Optoelectronic Materials Showing Bright Emission with Wide Color Gamut. *Nano letters* 2015, 15, 3692-6.
80. Hitoshi, K.; Hari Singh, N.; Hidetoshi, O.; Shuji, O.; Hiro, M.; Nobutsugu, M.; Atsushi, K.; Katsumichi, O.; Akio, M.; Hachiro, N., A Novel Preparation Method of Organic Microcrystals. *Japanese Journal of Applied Physics* 1992, 31, L1132.
81. Sun, S.; Yuan, D.; Xu, Y.; Wang, A.; Deng, Z., Ligand-Mediated Synthesis of Shape-Controlled Cesium Lead Halide Perovskite Nanocrystals via Reprecipitation Process at Room Temperature. *ACS nano* 2016, 10, 3648-57.

82. <MA QDs ACS Nano.pdf>.
83. Teunis, M. B.; Johnson, M. A.; Muhoberac, B. B.; Seifert, S.; Sardar, R., Programmable Colloidal Approach to Hierarchical Structures of Methylammonium Lead Bromide Perovskite Nanocrystals with Bright Photoluminescent Properties. *Chemistry of Materials* 2017, 29, 3526-3537.
84. Zhang, F.; Zhong, H.; Chen, C.; Wu, X.-g.; Hu, X.; Huang, H.; Han, J.; Zou, B.; Dong, Y., Brightly Luminescent and Color-Tunable Colloidal CH3NH3PbX3 (X = Br, I, Cl) Quantum Dots: Potential Alternatives for Display Technology. *ACS nano* 2015, 9, 4533-4542.
85. Zhang, F.; Huang, S.; Wang, P.; Chen, X.; Zhao, S.; Dong, Y.; Zhong, H., Colloidal Synthesis of Air-Stable CH3NH3PbI3 Quantum Dots by Gaining Chemical Insight into the Solvent Effects. *Chemistry of Materials* 2017, 29, 3793-3799.
86. Shekhirev, M.; Goza, J.; Teeter, J. D.; Lipatov, A.; Sinitskii, A., Synthesis of Cesium Lead Halide Perovskite Quantum Dots. *Journal of Chemical Education* 2017, 94, 1150-1156.
87. Vybornyi, O.; Yakunin, S.; Kovalenko, M. V., Polar-solvent-free colloidal synthesis of highly luminescent alkylammonium lead halide perovskite nanocrystals. *Nanoscale* 2016, 8, 6278-83.
88. Protesescu, L.; Yakunin, S.; Bodnarchuk, M. I.; Bertolotti, F.; Masciocchi, N.; Guagliardi, A.; Kovalenko, M. V., Monodisperse Formamidinium Lead Bromide Nanocrystals with Bright and Stable Green Photoluminescence. *Journal of the American Chemical Society* 2016, 138, 14202-14205.
89. De Roo, J.; Ibanez, M.; Geiregat, P.; Nedelcu, G.; Walravens, W.; Maes, J.; Martins, J. C.; Van Driessche, I.; Kovalenko, M. V.; Hens, Z., Highly Dynamic Ligand Binding and Light Absorption Coefficient of Cesium Lead Bromide Perovskite Nanocrystals. *ACS nano* 2016, 10, 2071-81.
90. Pan, Q.; Hu, H.; Zou, Y.; Chen, M.; Wu, L.; Yang, D.; Yuan, X.; Fan, J.; Sun, B.; Zhang, Q., Microwave-assisted synthesis of high-quality "all-inorganic" CsPbX3 (X = Cl, Br, I) perovskite nanocrystals and their application in light emitting diodes. *J Mater Chem C* 2017, 5, 10947-10954.
91. Long, Z.; Ren, H.; Sun, J.; Ouyang, J.; Na, N., High-throughput and tunable synthesis of colloidal CsPbX3 perovskite nanocrystals in a heterogeneous system by microwave irradiation. *Chem. Commun.* 2017.
92. Epps, R. W.; Felton, K. C.; Coley, C. W.; Abolhasani, M., Automated microfluidic platform for systematic studies of colloidal perovskite nanocrystals: towards continuous nano-manufacturing. *Lab on a chip* 2017.
93. Tong, Y.; Bladt, E.; Ayguler, M. F.; Manzi, A.; Milowska, K. Z.; Hintermayr, V. A.; Docampo, P.; Bals, S.; Urban, A. S.; Polavarapu, L.; Feldmann, J., Highly Luminescent Cesium Lead Halide Perovskite Nanocrystals with Tunable Composition and Thickness by Ultrasonication. *Angewandte Chemie* 2016, 55, 13887-13892.
94. Chen, M.; Zou, Y.; Wu, L.; Pan, Q.; Yang, D.; Hu, H.; Tan, Y.; Zhong, Q.; Xu, Y.; Liu, H.; Sun, B.; Zhang, Q., Solvothermal Synthesis of High-Quality All-Inorganic Cesium Lead Halide Perovskite Nanocrystals: From Nanocube to Ultrathin Nanowire. *Advanced Functional Materials* 2017, 27, 1701121.
95. Akkerman, Q. A.; D'Innocenzo, V.; Accornero, S.; Scarpellini, A.; Petrozza, A.; Prato, M.; Manna, L., Tuning the Optical Properties of Cesium Lead Halide Perovskite Nanocrystals by Anion Exchange Reactions. *Journal of the American Chemical Society* 2015, 137, 10276-81.
96. Nedelcu, G.; Protesescu, L.; Yakunin, S.; Bodnarchuk, M. I.; Grotevent, M. J.; Kovalenko, M. V., Fast Anion-Exchange in Highly Luminescent Nanocrystals of Cesium Lead Halide Perovskites (CsPbX3, X = Cl, Br, I). *Nano letters* 2015, 15, 5635-40.
97. Protesescu, L.; Yakunin, S.; Kumar, S.; Bar, J.; Bertolotti, F.; Masciocchi, N.; Guagliardi, A.; Grotevent, M.; Shorubalko, I.; Bodnarchuk, M. I.; Shih, C. J.; Kovalenko, M. V., Dismantling the "Red Wall" of Colloidal Perovskites: Highly Luminescent Formamidinium and Formamidinium-Cesium Lead Iodide Nanocrystals. *ACS nano* 2017, 11, 3119-3134.
98. Koscher, B. A.; Swabeck, J. K.; Bronstein, N. D.; Alivisatos, A. P., Essentially Trap-Free CsPbBr3 Colloidal Nanocrystals by Postsynthetic Thiocyanate Surface Treatment. *Journal of the American Chemical Society* 2017, 139, 6566-6569.
99. Liu, F.; Zhang, Y.; Ding, C.; Kobayashi, S.; Izuishi, T.; Nakazawa, N.; Toyoda, T.; Ohta, T.; Hayase, S.; Minemoto, T.; Yoshino, K.; Dai, S.; Shen, Q., Highly Luminescent Phase-Stable CsPbI3 Perovskite Quantum Dots Achieving Near 100% Absolute Photoluminescence Quantum Yield. *ACS nano* 2017, 11, 10373-10383.

100. Sichert, J. A.; Tong, Y.; Mutz, N.; Vollmer, M.; Fischer, S.; Milowska, K. Z.; Garcia Cortadella, R.; Nickel, B.; Cardenas-Daw, C.; Stolarczyk, J. K.; Urban, A. S.; Feldmann, J., Quantum Size Effect in Organometal Halide Perovskite Nanoplatelets. *Nano letters* 2015, 15, 6521-7.
101. Wang, D.; Wu, D.; Dong, D.; Chen, W.; Hao, J.; Qin, J.; Xu, B.; Wang, K.; Sun, X., Polarized emission from CsPbX3 perovskite quantum dots. *Nanoscale* 2016, 8, 11565-11570.
102. Yakunin, S.; Protesescu, L.; Krieg, F.; Bodnarchuk, M. I.; Nedelcu, G.; Humer, M.; De Luca, G.; Fiebig, M.; Heiss, W.; Kovalenko, M. V., Low-threshold amplified spontaneous emission and lasing from colloidal nanocrystals of caesium lead halide perovskites. *Nature communications* 2015, 6, 8056.
103. He, X.; Qiu, Y.; Yang, S., Fully-Inorganic Trihalide Perovskite Nanocrystals: A New Research Frontier of Optoelectronic Materials. *Advanced materials* 2017.
104. Yoon, H. C.; Oh, J. H.; Lee, S.; Park, J. B.; Do, Y. R., Circadian-tunable Perovskite Quantum Dot-based Down-Converted Multi-Package White LED with a Color Fidelity Index over 90. *Scientific reports* 2017, 7, 2808.
105. Kamtekar, K. T.; Monkman, A. P.; Bryce, M. R., Recent advances in white organic light-emitting materials and devices (WOLEDs). *Advanced materials* 2010, 22, 572-82.
106. Geim, A. K., Graphene: status and prospects. *Science* 2009, 324, 1530-4.
107. Zhao, W.; Ribeiro, R. M.; Eda, G., Electronic structure and optical signatures of semiconducting transition metal dichalcogenide nanosheets. *Accounts of chemical research* 2015, 48, 91-9.
108. Zhang, H., Ultrathin Two-Dimensional Nanomaterials. *ACS nano* 2015, 9, 9451-69.
109. Ataca, C.; Şahin, H.; Ciraci, S., Stable, Single-Layer MX2 Transition-Metal Oxides and Dichalcogenides in a Honeycomb-Like Structure. *The Journal of Physical Chemistry C* 2012, 116, 8983-8999.
110. Lin, Y.; Williams, T. V.; Connell, J. W., Soluble, Exfoliated Hexagonal Boron Nitride Nanosheets. *The journal of physical chemistry letters* 2010, 1, 277-283.
111. Tan, C.; Zhang, H., Wet-chemical synthesis and applications of non-layer structured two-dimensional nanomaterials. *Nature communications* 2015, 6, 7873.
112. Wang, F.; Wang, Y.; Liu, Y.-H.; Morrison, P. J.; Loomis, R. A.; Buhro, W. E., Two-Dimensional Semiconductor Nanocrystals: Properties, Templated Formation, and Magic-Size Nanocluster Intermediates. *Accounts of chemical research* 2015, 48, 13-21.
113. Lhuillier, E.; Pedetti, S.; Ithurria, S.; Nadal, B.; Heuclin, H.; Dubertret, B., Two-dimensional colloidal metal chalcogenides semiconductors: synthesis, spectroscopy, and applications. *Accounts of chemical research* 2015, 48, 22-30.
114. Zhu, F.; Men, L.; Guo, Y.; Zhu, Q.; Bhattacharjee, U.; Goodwin, P. M.; Petrich, J. W.; Smith, E. A.; Vela, J., Shape evolution and single particle luminescence of organometal halide perovskite nanocrystals. *ACS nano* 2015, 9, 2948-59.
115. Dou, L.; Wong, A. B.; Yu, Y.; Lai, M.; Kornienko, N.; Eaton, S. W.; Fu, A.; Bischak, C. G.; Ma, J.; Ding, T.; Ginsberg, N. S.; Wang, L. W.; Alivisatos, A. P.; Yang, P., Atomically thin two-dimensional organic-inorganic hybrid perovskites. *Science* 2015, 349, 1518-21.
116. Zhang, D.; Eaton, S. W.; Yu, Y.; Dou, L.; Yang, P., Solution-Phase Synthesis of Cesium Lead Halide Perovskite Nanowires. *Journal of the American Chemical Society* 2015, 137, 9230-3.
117. Akkerman, Q. A.; Motti, S. G.; Srimath Kandada, A. R.; Mosconi, E.; D'Innocenzo, V.; Bertoni, G.; Marras, S.; Kamino, B. A.; Miranda, L.; De Angelis, F.; Petrozza, A.; Prato, M.; Manna, L., Solution Synthesis Approach to Colloidal Cesium Lead Halide Perovskite Nanoplatelets with Monolayer-Level Thickness Control. *Journal of the American Chemical Society* 2016, 138, 1010-6.
118. Bekenstein, Y.; Koscher, B. A.; Eaton, S. W.; Yang, P.; Alivisatos, A. P., Highly Luminescent Colloidal Nanoplates of Perovskite Cesium Lead Halide and Their Oriented Assemblies. *Journal of the American Chemical Society* 2015, 137, 16008-11.
119. Yantara, N.; Bhaumik, S.; Yan, F.; Sabba, D.; Dewi, H. A.; Mathews, N.; Boix, P. P.; Demir, H. V.; Mhaisalkar, S., Inorganic Halide Perovskites for Efficient Light-Emitting Diodes. *The journal of physical chemistry letters* 2015, 6, 4360-4.

120. Swarnkar, A.; Chulliyil, R.; Ravi, V. K.; Irfanullah, M.; Chowdhury, A.; Nag, A., Colloidal CsPbBr3 Perovskite Nanocrystals: Luminescence beyond Traditional Quantum Dots. *Angewandte Chemie International Edition* 2015, 54, 15424-15428.
121. Cottingham, P.; Brutchey, R. L., On the crystal structure of colloidally prepared CsPbBr3 quantum dots. *Chemical communications* 2016, 52, 5246-9.
122. Amgar, D.; Stern, A.; Rotem, D.; Porath, D.; Etgar, L., Tunable Length and Optical Properties of CsPbX3 (X = Cl, Br, I) Nanowires with a Few Unit Cells. *Nano letters* 2017, 17, 1007-1013.
123. Zhang, D.; Yu, Y.; Bekenstein, Y.; Wong, A. B.; Alivisatos, A. P.; Yang, P., Ultrathin Colloidal Cesium Lead Halide Perovskite Nanowires. *Journal of the American Chemical Society* 2016, 138, 13155-13158.
124. Zhang, D.; Yang, Y.; Bekenstein, Y.; Yu, Y.; Gibson, N. A.; Wong, A. B.; Eaton, S. W.; Kornienko, N.; Kong, Q.; Lai, M.; Alivisatos, A. P.; Leone, S. R.; Yang, P., Synthesis of Composition Tunable and Highly Luminescent Cesium Lead Halide Nanowires through Anion-Exchange Reactions. *Journal of the American Chemical Society* 2016, 138, 7236-9.
125. Teunis, M. B.; Jana, A.; Dutta, P.; Johnson, M. A.; Mandal, M.; Muhoberac, B. B.; Sardar, R., Mesoscale Growth and Assembly of Bright Luminescent Organolead Halide Perovskite Quantum Wires. *Chemistry of Materials* 2016, 28, 5043-5054.
126. Cho, J.; Choi, Y.-H.; O'Loughlin, T. E.; De Jesus, L.; Banerjee, S., Ligand-Mediated Modulation of Layer Thicknesses of Perovskite Methylammonium Lead Bromide Nanoplatelets. *Chemistry of Materials* 2016, 28, 6909-6916.
127. Song, J.; Xu, L.; Li, J.; Xue, J.; Dong, Y.; Li, X.; Zeng, H., Monolayer and Few-Layer All-Inorganic Perovskites as a New Family of Two-Dimensional Semiconductors for Printable Optoelectronic Devices. *Advanced materials* 2016, 28, 4861-9.
128. Hintermayr, V. A.; Richter, A. F.; Ehrat, F.; Doblinger, M.; Vanderlinden, W.; Sichert, J. A.; Tong, Y.; Polavarapu, L.; Feldmann, J.; Urban, A. S., Tuning the Optical Properties of Perovskite Nanoplatelets through Composition and Thickness by Ligand-Assisted Exfoliation. *Advanced materials* 2016, 28, 9478-9485.
129. Liang, Z.; Zhao, S.; Xu, Z.; Qiao, B.; Song, P.; Gao, D.; Xu, X., Shape-controlled Synthesis of All-inorganic CsPbBr3 Perovskite Nanocrystals with Bright Blue Emission. *ACS applied materials & interfaces* 2016.
130. van Embden, J.; Chesman, A. S. R.; Jasieniak, J. J., The Heat-Up Synthesis of Colloidal Nanocrystals. *Chemistry of Materials* 2015, 27, 2246-2285.
131. Di Stasio, F.; Imran, M.; Akkerman, Q. A.; Prato, M.; Manna, L.; Krahne, R., Reversible Concentration-Dependent Photoluminescence Quenching and Change of Emission Color in CsPbBr3 Nanowires and Nanoplatelets. *The journal of physical chemistry letters* 2017, 8, 2725-2729.
132. Kim, Y.; Yassitepe, E.; Voznyy, O.; Comin, R.; Walters, G.; Gong, X.; Kanjanaboos, P.; Nogueira, A. F.; Sargent, E. H., Efficient Luminescence from Perovskite Quantum Dot Solids. *ACS applied materials & interfaces* 2015, 7, 25007-13.
133. Yuan, H.; Debroye, E.; Janssen, K.; Naiki, H.; Steuwe, C.; Lu, G.; Moris, M.; Orgiu, E.; Uji, I. H.; De Schryver, F.; Samori, P.; Hofkens, J.; Roeffaers, M., Degradation of Methylammonium Lead Iodide Perovskite Structures through Light and Electron Beam Driven Ion Migration. *The journal of physical chemistry letters* 2016, 7, 561-6.
134. Hoke, E. T.; Slotcavage, D. J.; Dohner, E. R.; Bowring, A. R.; Karunadasa, H. I.; McGehee, M. D., Reversible photo-induced trap formation in mixed-halide hybrid perovskites for photovoltaics. *Chem Sci* 2015, 6, 613-617.
135. deQuilettes, D. W.; Zhang, W.; Burlakov, V. M.; Graham, D. J.; Leijtens, T.; Osherov, A.; Bulovic, V.; Snaith, H. J.; Ginger, D. S.; Stranks, S. D., Photo-induced halide redistribution in organic-inorganic perovskite films. *Nature communications* 2016, 7, 11683.
136. Wang, Y.; Li, X.; Sreejith, S.; Cao, F.; Wang, Z.; Stuparu, M. C.; Zeng, H.; Sun, H., Photon Driven Transformation of Cesium Lead Halide Perovskites from Few-Monolayer Nanoplatelets to Bulk Phase. *Advanced materials* 2016, 28, 10637-10643.
137. Huang, S.; Li, Z.; Wang, B.; Zhu, N.; Zhang, C.; Kong, L.; Zhang, Q.; Shan, A.; Li, L., Morphology Evolution and Degradation of CsPbBr3 Nanocrystals under Blue Light-Emitting Diode Illumination. *ACS applied materials & interfaces* 2017, 9, 7249-7258.

138. Baghbanzadeh, M.; Carbone, L.; Cozzoli, P. D.; Kappe, C. O., Microwave-assisted synthesis of colloidal inorganic nanocrystals. *Angewandte Chemie* 2011, 50, 11312-59.
139. Shamsi, J.; Rastogi, P.; Caligiuri, V.; Abdelhady, A. L.; Spirito, D.; Manna, L.; Krahne, R., Bright-Emitting Perovskite Films by Large-Scale Synthesis and Photoinduced Solid-State Transformation of CsPbBr3 Nanoplatelets. *ACS nano* 2017, 11, 10206-10213.
140. Shamsi, J.; Dang, Z.; Bianchini, P.; Canale, C.; Stasio, F. D.; Brescia, R.; Prato, M.; Manna, L., Colloidal Synthesis of Quantum Confined Single Crystal CsPbBr3 Nanosheets with Lateral Size Control up to the Micrometer Range. *Journal of the American Chemical Society* 2016, 138, 7240-3.
141. Mir, W. J.; Jagadeeswararao, M.; Das, S.; Nag, A., Colloidal Mn-Doped Cesium Lead Halide Perovskite Nanoplatelets. *ACS Energy Letters* 2017, 2, 537-543.
142. Motti, S. G.; Gandini, M.; Barker, A. J.; Ball, J. M.; Srimath Kandada, A. R.; Petrozza, A., Photoinduced Emissive Trap States in Lead Halide Perovskite Semiconductors. *ACS Energy Letters* 2016, 1, 726-730.
143. Ling, Y.; Yuan, Z.; Tian, Y.; Wang, X.; Wang, J. C.; Xin, Y.; Hanson, K.; Ma, B.; Gao, H., Bright Light-Emitting Diodes Based on Organometal Halide Perovskite Nanoplatelets. *Advanced materials* 2016, 28, 305-11.
144. Pan, J.; Quan, L. N.; Zhao, Y.; Peng, W.; Murali, B.; Sarmah, S. P.; Yuan, M.; Sinatra, L.; Alyami, N. M.; Liu, J.; Yassitepe, E.; Yang, Z.; Voznyy, O.; Comin, R.; Hedhili, M. N.; Mohammed, O. F.; Lu, Z. H.; Kim, D. H.; Sargent, E. H.; Bakr, O. M., Highly Efficient Perovskite-Quantum-Dot Light-Emitting Diodes by Surface Engineering. *Advanced materials* 2016, 28, 8718-8725.
145. Song, J.; Li, J.; Li, X.; Xu, L.; Dong, Y.; Zeng, H., Quantum Dot Light-Emitting Diodes Based on Inorganic Perovskite Cesium Lead Halides (CsPbX3). *Advanced materials* 2015, 27, 7162-7.
146. Kim, Y. H.; Wolf, C.; Kim, Y. T.; Cho, H.; Kwon, W.; Do, S.; Sadhanala, A.; Park, C. G.; Rhee, S. W.; Im, S. H.; Friend, R. H.; Lee, T. W., Highly Efficient Light-Emitting Diodes of Colloidal Metal-Halide Perovskite Nanocrystals beyond Quantum Size. *ACS nano* 2017, 11, 6586-6593.
147. Byun, J.; Cho, H.; Wolf, C.; Jang, M.; Sadhanala, A.; Friend, R. H.; Yang, H.; Lee, T. W., Efficient Visible Quasi-2D Perovskite Light-Emitting Diodes. *Advanced materials* 2016, 28, 7515-20.
148. Kim, Y.-H.; Lee, G.-H.; Kim, Y.-T.; Wolf, C.; Yun, H. J.; Kwon, W.; Park, C. G.; Lee, T. W., High efficiency perovskite light-emitting diodes of ligand-engineered colloidal formamidinium lead bromide nanoparticles. *Nano Energy* 2017, 38, 51-58.
149. Li, G.; Rivarola, F. W.; Davis, N. J.; Bai, S.; Jellicoe, T. C.; de la Pena, F.; Hou, S.; Ducati, C.; Gao, F.; Friend, R. H.; Greenham, N. C.; Tan, Z. K., Highly Efficient Perovskite Nanocrystal Light-Emitting Diodes Enabled by a Universal Crosslinking Method. *Advanced materials* 2016, 28, 3528-34.
150. Yassitepe, E.; Yang, Z.; Voznyy, O.; Kim, Y.; Walters, G.; Castañeda, J. A.; Kanjanaboos, P.; Yuan, M.; Gong, X.; Fan, F.; Pan, J.; Hoogland, S.; Comin, R.; Bakr, O. M.; Padilha, L. A.; Nogueira, A. F.; Sargent, E. H., Amine-Free Synthesis of Cesium Lead Halide Perovskite Quantum Dots for Efficient Light-Emitting Diodes. *Advanced Functional Materials* 2016, 26, 8757-8763.
151. Cardona, M.; Haensel, R.; Lynch, D. W.; Sonntag, B., Optical Properties of the Rubidium and Cesium Halides in the Extreme Ultraviolet. *Phys. Rev. B* 1970, 2, 1117-1131.
152. Maldonado, J. R.; Coyle, S. T.; Shamoun, B.; Yu, M.; Gesley, M.; Pianetta, P., Cs halide photocathode for multi-electron-beam pattern generator. *J. Vac. Sci. Technol. B* 2004, 22, 3025.
153. Nikl, M.; Yoshikawa, A., Recent R&D Trends in Inorganic Single-Crystal Scintillator Materials for Radiation Detection. *Adv. Opt. Mater.* 2015, 3, 463-481.
154. Poole, R. T.; Jenkin, J. G.; Liesegang, J.; Leckey, R. C. G., Electronic band structure of the alkali halides. I. Experimental parameters. *Phys. Rev. B* 1975, 11, 5179-5189.
155. Halliday, M. T.; Hess, W. P.; Shluger, A. L., Structure and properties of electronic and hole centers in CsBr from theoretical calculations. *J. Phys. Condens. Matter* 2015, 27, 245501.
156. Nikl, M.; Nitsch, K.; Mihokova, E.; Polak, K.; Fabeni, P.; Pazzi, G. P.; Gurioli, M.; Phani, R.; Santucci, S.; Scacco, A.; Somma, F., Optical properties of Pb2+-based aggregated phases in CsBr Thin film and single crystal matrices. *Radiat. Eff. Defect. S.* 1999, 150, 341-345.

157. Aceves, R.; Babin, V.; Barboza Flores, M.; Fabeni, P.; Mihokova, E.; Nikl, M.; Nitsch, K.; Pazzi, G. P.; Perez Salas, R.; Zazubovich, N.; Zazubovich, S., Relaxed Excited States Origin and Structure in Lead-Doped Caesium Bromide. *Phys. Status Solidi b* 2001, 223, 745-756.
158. Shamsi, J.; Dang, Z.; Ijaz, P.; Abdelhady, A. L.; Bertoni, G.; Moreels, I.; Manna, L., Colloidal CsX (X = Cl, Br, I) Nanocrystals and Their Transformation to CsPbX3 Nanocrystals by Cation Exchange. *Chemistry of Materials* 2017, 30, 79-83.
159. Knittle, E.; Jeanloz, R., Structural and Bonding Changes in Cesium Iodide at High Pressures. *Science* 1984, 223, 53-56.
160. Onodera, Y., Energy Bands in CsI. *J. Phys. Soc. Jap.* 1968, 25, 469-480.
161. Said, K. I.; Green, G. W., Optical properties of caesium iodide in the vacuum ultraviolet. *J. Phys. C* 1977, 10, 479.
162. Dvorak, M.; Wei, S.-H.; Wu, Z., Origin of the Variation of Exciton Binding Energy in Semiconductors. *Phys. Rev. Lett.* 2013, 110, 016402.
163. Dang, Z.; Shamsi, J.; Palazon, F.; Imran, M.; Akkerman, Q. A.; Park, S.; Bertoni, G.; Prato, M.; Brescia, R.; Manna, L., In Situ Transmission Electron Microscopy Study of Electron Beam-Induced Transformations in Colloidal Cesium Lead Halide Perovskite Nanocrystals. *ACS Nano* 2017, 11, 2124-2132.
164. Kamminga, M. E.; Fang, H.-H.; Filip, M. R.; Giustino, F.; Baas, J.; Blake, G. R.; Loi, M. A.; Palstra, T. T. M., Confinement Effects in Low-Dimensional Lead Iodide Perovskite Hybrids. *Chemistry of Materials* 2016, 28, 4554-4562.
165. Koscher, B. A.; Swabeck, J. K.; Bronstein, N. D.; Alivisatos, A. P., Essentially Trap-Free $CsPbBr_3$ Colloidal Nanocrystals by Postsynthetic Thiocyanate Surface Treatment. *J. Am. Chem. Soc.* 2017, 139, 6566-6569.
166. http://www.nrel.gov/ncpv/images/efficiency_chart.jpg (accessed 13.08.2016).
167. Saparov, B.; Mitzi, D. B., Organic–Inorganic Perovskites: Structural Versatility for Functional Materials Design. *Chem. Rev.* 2016, 116, 4558–4596.
168. Manser, J. S.; Saidaminov, M. I.; Christians, J. A.; Bakr, O. M.; Kamat, P. V., Making and Breaking of Lead Halide Perovskites. *Acc. Chem. Res.* 2016, 49, 330-338.
169. Gao, P.; Grätzel, M.; Nazeeruddin, M. K., Organohalide lead perovskites for photovoltaic applications. *Energy Environ. Sci.* 2014, 7, 2448-2448.
170. Saidaminov, M. I.; Adinolfi, V.; Comin, R.; Abdelhady, A. L.; Peng, W.; Dursun, I.; Yuan, M.; Hoogland, S.; Sargent, E. H.; Bakr, O. M., Planar-integrated single-crystalline perovskite photodetectors. *Nat. Commun.* 2015, 6, 8724-8724.
171. Saidaminov, M. I.; Haque, M. A.; Savoie, M.; Abdelhady, A. L.; Cho, N.; Dursun, I.; Buttner, U.; Alarousu, E.; Wu, T.; Bakr, O. M., Perovskite Photodetectors Operating in Both Narrowband and Broadband Regimes. *Adv. Mater.* 2016, 10.1002/adma.201601235.
172. Tan, Z.-K.; Moghaddam, R. S.; Lai, M. L.; Docampo, P.; Higler, R.; Deschler, F.; Price, M.; Sadhanala, A.; Pazos, L. M.; Credgington, D.; Hanusch, F.; Bein, T.; Snaith, H. J.; Friend, R. H., SI: Bright light-emitting diodes based on organometal halide perovskite. *Nat. Nanotech.* 2014, 9, 1-6.
173. Wang, J.; Wang, N.; Jin, Y.; Si, J.; Tan, Z.-K.; Du, H.; Cheng, L.; Dai, X.; Bai, S.; He, H.; Ye, Z.; Lai, M. L.; Friend, R. H.; Huang, W., Interfacial Control Toward Efficient and Low-Voltage Perovskite Light-Emitting Diodes. *Adv. Mater.* 2015, 27, 2311-2316.
174. Saidaminov, M. I.; Abdelhady, A. L.; Murali, B.; Alarousu, E.; Burlakov, V. M.; Peng, W.; Dursun, I.; Wang, L.; He, Y.; Maculan, G.; Goriely, A.; Wu, T.; Mohammed, O. F.; Bakr, O. M., High-quality bulk hybrid perovskite single crystals within minutes by inverse temperature crystallization. *Nat. Commun.* 2015, 6, 7586-7586.
175. Shi, D.; Adinolfi, V.; Comin, R.; Yuan, M.; Alarousu, E.; Buin, A.; Chen, Y.; Hoogland, S.; Rothenberger, A.; Katsiev, K.; Losovyj, Y.; Zhang, X.; Dowben, P. A.; Mohammed, O. F.; Sargent, E. H.; Bakr, O. M., Solar cells. Low trap-state density and long carrier diffusion in organolead trihalide perovskite single crystals. *Science* 2015, 347, 519-22.
176. Noh, J. H.; Im, S. H.; Heo, J. H.; Mandal, T. N.; Seok, S. I., Chemical management for colorful, efficient, and stable inorganic-organic hybrid nanostructured solar cells. *Nano Lett.* 2013, 13, 1764-1769.

177. Zhang, F.; Zhong, H.; Chen, C.; Wu, X. G.; Hu, X.; Huang, H.; Han, J.; Zou, B.; Dong, Y., Brightly luminescent and color-tunable colloidal $CH_3NH_3PX_3$ (X = Br, I, Cl) quantum dots: Potential alternatives for display technology. *ACS Nano* 2015, 9, 4533-4542.
178. Zhao, T.; Chueh, C.-C.; Chen, Q.; Rajagopal, A.; Jen, A. K. Y., Defect Passivation of Organic–Inorganic Hybrid Perovskites by Diammonium Iodide toward High-Performance Photovoltaic Devices. *ACS Energy Lett.* 2016, 1, 757-763.
179. Etgar, L.; Gao, P.; Qin, P.; Gratzel, M.; Nazeeruddin, M. K., A hybrid lead iodide perovskite and lead sulfide QD heterojunction solar cell to obtain a panchromatic response. *J. Mater. Chem. A* 2014, 2, 11586-11590.
180. Maculan, G.; Sheikh, A. D.; Abdelhady, A. L.; Saidaminov, M. I.; Haque, M. A.; Murali, B.; Alarousu, E.; Mohammed, O. F.; Wu, T.; Bakr, O. M., $CH_3NH_3PbCl_3$ Single Crystals: Inverse Temperature Crystallization and Visible-Blind UV-Photodetector. *J. Phys. Chem. Lett.* 2015, 6, 3781-3786.
181. Kojima, A.; Teshima, K.; Shirai, Y.; Miyasaka, T., Organometal halide perovskites as visible-light sensitizers for photovoltaic cells. *J. Am. Chem. Soc.* 2009, 131, 6050-6051.
182. Akkerman, Q. A.; D'Innocenzo, V.; Accornero, S.; Scarpellini, A.; Petrozza, A.; Prato, M.; Manna, L., Tuning the optical properties of cesium lead halide perovskite nanocrystals by anion exchange reactions. *J. Am. Chem. Soc.* 2015, 137, 10276-10281.
183. Palazon, F.; Akkerman, Q. A.; Prato, M.; Manna, L., X-Ray Lithography on Perovskite Nanocrystals Films: From Patterning with Anion-Exchange Reactions to Enhanced Stability in Air and Water. *ACS Nano* 2016, 10, 1224–1230.
184. Huang, H.; Susha, A. S.; Kershaw, S. V.; Hung, T. F.; Rogach, A. L., Control of Emission Color of High Quantum Yield $CH_3NH_3PBr_3$ Perovskite Quantum Dots by Precipitation Temperature. *Adv. Sci.* 2015, 2, 1500194.
185. Bhaumik, S.; Veldhuis, S.; Ng, Y. F.; Li, M.; Muduli, S. K.; Sum, T. C.; Damodaran, B.; Mhaisalkar, S. G.; Mathews, N., Highly stable, luminescent core-shell type methylammonium-octylammonium lead bromide layered perovskite nanoparticles. *Chem. Commun.* 2016, 52, 7118-7121.
186. Schmidt, L. C.; Pertegás, A.; González-Carrero, S.; Malinkiewicz, O.; Agouram, S.; Mínguez Espallargas, G.; Bolink, H. J.; Galian, R. E.; Pérez-Prieto, J., Nontemplate Synthesis of $CH_3NH_3PbBr_3$ Perovskite Nanoparticles. *J. Am. Chem. Soc.* 2014, 136, 850-853.
187. Van den Bulcke, M.; Rosseel, M. T.; Wijnants, P.; Buylaert, W.; Belpaire, F. M., Metabolism and hepatotoxicity of N,N-dimethylformamide, N-hydroxymethyl-N-methylformamide, and N-methylformamide in the rat. *Arch. Toxicol.* 1994, 68, 291-5.
188. Shamsi, J.; Abdelhady, A. L.; Accornero, S.; Arciniegas, M.; Goldoni, L.; Kandada, A. R.; Petrozza, A.; Manna, L., N-Methylformamide as a Source of Methylammonium Ions in the Synthesis of Lead Halide Perovskite Nanocrystals and Bulk Crystals. *ACS Energy Lett* 2016, 1, 1042-1048.
189. Cottineau, T.; Richard-Plouet, M.; Mevellec, J.-Y.; Brohan, L., Hydrolysis and Complexation of N,N-Dimethylformamide in New Nanostructurated Titanium Oxide Hybrid OrganicÀInorganic Sols and Gel. *J. Phys. Chem. C* 2011, 115, 12269-12274.
190. Eppel, S.; Fridman, N.; Frey, G., Amide-Templated Iodoplumbates: Extending Lead-Iodide Based Hybrid Semiconductors. *Cryst. Growth Des.* 2015, 15, 4363-4371.
191. Dang, Y.; Liu, Y.; Sun, Y.; Yuan, D.; Liu, X.; Lu, W.; Liu, G.; Xia, H.; Tao, X., Bulk crystal growth of hybrid perovskite material $CH_3NH_3PbI_3$. *CrystEngComm* 2015, 17, 665-670.
192. Fu, Y.; Zhu, H.; Schrader, A. W.; Liang, D.; Ding, Q.; Joshi, P.; Hwang, L.; Zhu, X. Y.; Jin, S., Nanowire Lasers of Formamidinium Lead Halide Perovskites and Their Stabilized Alloys with Improved Stability. *Nano letters* 2016, 16, 1000-8.
193. Seo, J. Y.; Matsui, T.; Luo, J.; Correa-Baena, J. P.; Giordano, F.; Saliba, M.; Schenk, K.; Ummadisingu, A.; Domanski, K.; Hadadian, M.; Hagfeldt, A.; Zakeeruddin, S. M.; Steiner, U.; Grätzel, M.; Abate, A., Ionic Liquid Control Crystal Growth to Enhance Planar Perovskite Solar Cells Efficiency. *Adv. Ener. Mater.* 2016, 10.1002/aenm.201600767.
194. Tamura, M.; Tonomura, T.; Shimizu, K.-i.; Satsuma, A., Transamidation of amides with amines under solvent-free conditions using a CeO_2 catalyst. *Greem Chem.* 2012, 14, 717-724.

195. Vybornyi, O.; Yakunin, S.; Kovalenko, M., Polar-solvent-free colloidal synthesis of highly luminescent alkylammonium lead halide perovskite nanocrystals. *Nanoscale* 2015, 8, 2-7.
196. Ravi, V. K.; Markad, G. B.; Nag, A., Band Edge Energies and Excitonic Transition Probabilities of Colloidal CsPbX3 (X = Cl, Br, I) Perovskite Nanocrystals. *ACS Energy Letters* 2016, 1, 665-671.
197. Vybornyi, O.; Yakunin, S.; Kovalenko, M. V., Polar-solvent-free colloidal synthesis of highly luminescent alkylammonium lead halide perovskite nanocrystals. *Nanoscale* 2016, 8, 6278-6283.
198. Nedelcu, G.; Protesescu, L.; Yakunin, S.; Bodnarchuk, M. I.; Grotevent, M. J.; Kovalenko, M. V., Fast Anion-Exchange in Highly Luminescent Nanocrystals of Cesium Lead Halide Perovskites ($CsPbX_3$, X = Cl, Br, I). *Nano Lett.* 2015, 15, 5635-5640.
199. Wang, Q.; Ren, J.; Peng, X. F.; Ji, X. X.; Yang, X. H., Efficient Sky-Blue Perovskite Light-Emitting Devices Based on Ethylammonium Bromide Induced Layered Perovskites. *ACS applied materials & interfaces* 2017, 9, 29901-29906.
200. Peng, W.; Wang, L.; Murali, B.; Ho, K.-T.; Bera, A.; Cho, N.; Kang, C.-F.; Burlakov, V. M.; Pan, J.; Sinatra, L.; Ma, C.; Xu, W.; Shi, D.; Alarousu, E.; Goriely, A.; He, J.-H.; Mohammed, O. F.; Wu, T.; Bakr, O. M., Solution-Grown Monocrystalline Hybrid Perovskite Films for Hole-Transporter-Free Solar Cells. *Adv. Mater.* 2016, 28, 3383-3390.
201. Liu, Y.; Yang, Z.; Cui, D.; Ren, X.; Sun, J.; Liu, X.; Zhang, J.; Wei, Q.; Fan, H.; Yu, F.; Zhang, X.; Zhao, C.; Liu, S., Two-Inch-Sized Perovskite $CH_3NH_3PbX_3$ (X = Cl, Br, I) Crystals: Growth and Characterization. *Adv. Mater.* 2015, 27, 5176-5183.
202. Srimath Kandada, A. R.; Petrozza, A., Research Update: Luminescence in lead halide perovskites. *APL Mater.* 2016, 4, 091506.
203. D'Innocenzo, V.; Srimath Kandada, A. R.; De Bastiani, M.; Gandini, M.; Petrozza, A., Tuning the Light Emission Properties by Band Gap Engineering in Hybrid Lead Halide Perovskite. *J. Am. Chem. Soc.* 2014, 136, 17730-17733.
204. Motti, S. G.; Gandini, M.; Barker, A. J.; Ball, J. M.; Srimath Kandada, A. R.; Petrozza, A., Photoinduced Emissive Trap States in Lead Halide Perovskite Semiconductors. *ACS Energy Lett.* 2016, 726-730.
205. Adhikari, N.; Dubey, A.; Gaml, E. A.; Vaagensmith, B.; Reza, K. M.; Mabrouk, S. A. A.; Gu, S.; Zai, J.; Qian, X.; Qiao, Q., Crystallization of a perovskite film for higher performance solar cells by controlling water concentration in methyl ammonium iodide precursor solution. *Nanoscale* 2016, 8, 2693-2703.
206. Yoon, S. J.; Stamplecoskie, K. G.; Kamat, P. V., How Lead Halide Complex Chemistry Dictates the Composition of Mixed Halide Perovskites. *J. Phys. Chem. Lett.* 2016, 7, 1368-1373.

Scientific Output

Publications

(1) **Shamsi, J.**; Dang, Z.; Ijaz, P.; Abdelhady, A. L.; Bertoni, G.; Moreels, I.; Manna, L. Colloidal CsX (X= Cl, Br, I) Nanocrystals and Their Transformation to $CsPbX_3$ Nanocrystals by Cation Exchange. *Chem. Mater.* **2018**, 30, 79–83.

(2) **Shamsi, J.**; Rastogi, P.; Caligiuri, V.; Abdelhady, A. L.; Spirito, D.; Manna, L.; Krahne, R. Bright-Emitting Perovskite Films by Large-Scale Synthesis and Photoinduced Solid-State Transformation of $CsPbBr_3$ Nanoplatelets. *ACS nano* **2017**, *11*, 10206-10213.

(3) Dang, Z.; **Shamsi, J.**; Akkerman, Q. A.; Imran, M.; Bertoni, G.; Brescia, R.; Manna, L. Low-Temperature Electron Beam-Induced Transformations of Cesium Lead Halide Perovskite Nanocrystals. *ACS omega* **2017**, *2*, 5660-5665.

(4) Dang, Z.; **Shamsi, J.**; Palazon, F.; Imran, M.; Akkerman, Q. A.; Park, S.; Bertoni, G.; Prato, M.; Brescia, R.; Manna, L. In Situ Transmission Electron Microscopy Study of Electron Beam-Induced Transformations in Colloidal Cesium Lead Halide Perovskite Nanocrystals. *ACS nano* **2017**, *11*, 2124-2132.

(5) Imran, M.; Di Stasio, F.; Dang, Z.; Canale, C.; Khan, A. H.; **Shamsi, J.**; Brescia, R.; Prato, M.; Manna, L. Colloidal Synthesis of Strongly Fluorescent $CsPbBr_3$ Nanowires with Width Tunable Down to the Quantum Confinement Regime. *Chem. Mater.* **2016**, *28*, 6450-6454.

(6) **Shamsi, J.**; Abdelhady, A. L.; Accornero, S.; Arciniegas, M.; Goldoni, L.; Kandada, A. R. S.; Petrozza, A.; Manna, L. N-Methylformamide as a Source of Methylammonium Ions in the Synthesis of Lead Halide Perovskite Nanocrystals and Bulk Crystals. *ACS energy letters* **2016**, *1*, 1042-1048.

(7) S**hamsi, J.**; Dang, Z.; Bianchini, P.; Canale, C.; Di Stasio, F.; Brescia, R.; Prato, M.; Manna, L. Colloidal Synthesis of Quantum Confined Single Crystal $CsPbBr_3$ Nanosheets with Lateral Size Control up to the Micrometer Range. *J. Am. Chem. Soc.* **2016**, *138*, 7240-7243.

Oral talk

2017, Oxford, UK. PSCO 2017

A general method for the large-scale synthesis of uniform confined perovskite nanoplatelets and their solid state transformation

Posters

(1) 2016, Marburg, Germany. Nanax7.

"**Nanometer-thick single-crystalline CsPbBr3 perovskite nanosheets with micrometer-scale lateral size"**

(2) 2016, Genova, Italy. 2de International Conference on Perovskite Solar Cells and Optoelectronics (PSCO 2016).

"Quantum-confined single crystal CsPbBr3 perovskite nanosheets with micrometer-scale lateral size"

(3) 2017, Braga, Portugal. Nanax8.

"Chemical strategy towards hybrid lead halide perovskite: From bulk crystal to Nanocrystal"